



TECHNISCHE
UNIVERSITÄT
WIEN



DISSERTATION

Surface-Based Path Following Control on Freeform 3D Objects

ausgeführt zum Zwecke der Erlangung des akademischen Grades eines
Doktors der technischen Wissenschaften (Dr.techn.)

unter der Leitung von

Univ.Prof. Dipl.-Ing. Dr.techn. Andreas KUGI
Institut für Automatisierungs- und Regelungstechnik
E376

eingereicht an der

Technischen Universität Wien
Fakultät für Elektrotechnik und Informationstechnik

von

Christian HARTL-NESIC
e1025010



Die approbierte gedruckte Originalversion dieser Dissertation ist an der TU Wien Bibliothek verfügbar.
The approved original version of this doctoral thesis is available in print at TU Wien Bibliothek.

Studiendekan

Univ.Prof. Dr.-Ing. Wolfgang GAWLIK

Betreuer

Univ.Prof. Dipl.-Ing. Dr.techn. Andreas KUGI

Tag des Rigorosums

10. September 2020

Prüfungsvorsitzender

Univ.Prof. Dr.-Ing. Wolfgang GAWLIK

Erster Gutachter

Prof. Dr.-Ing. Tamim ASFOUR

Zweiter Gutachter

Ao. Univ.Prof. Dipl.-Ing. Dr.techn. Markus VINCZE



Die approbierte gedruckte Originalversion dieser Dissertation ist an der TU Wien Bibliothek verfügbar.
The approved original version of this doctoral thesis is available in print at TU Wien Bibliothek.

für mein Tierchen



Die approbierte gedruckte Originalversion dieser Dissertation ist an der TU Wien Bibliothek verfügbar.
The approved original version of this doctoral thesis is available in print at TU Wien Bibliothek.

Vorwort

Am 11. März 2020 wurde die weltweite Ausbreitung des Virus SARS-CoV-2 durch die Weltgesundheitsorganisation als Pandemie eingestuft. Folglich wurde ab 16. März 2020 der „Lockdown“ in Österreich mit strikten Ausgangsbeschränkungen und Maßnahmen zur sozialen Distanzierung verordnet, um die Ausbreitung des Virus einzudämmen. Fast zur Gänze entstand die vorliegende Niederschrift in dieser außergewöhnlichen Zeit unter diesen außergewöhnlichen Umständen.

An erster Stelle möchte ich mich bei meinem Doktorvater Andreas KUGI bedanken. Vielen herzlichen Dank, Andreas, für deinen fachlichen Rat, dein Vertrauen sowie die Möglichkeiten und Freiheiten, die du mir am Institut geboten hast. Speziell danke ich dir für deine Unterstützung auf der „Zielgeraden“ dieser Arbeit. Ich danke Thomas FEIX und Clemens DYCKMANS von adidas AG, die stets mit spannenden Aufgaben und Fragestellungen in der industriellen Robotik aufgewartet haben. Großer Dank gebührt meinem Betreuer Tobias GLÜCK. Danke, Tobias, ich hatte sehr viel Spaß an unserer gemeinsamen Arbeit, den Besprechungen und speziell auch in der gemeinsamen Zeit auf Dienstreisen.

Vielen Dank an alle aktuellen und ehemaligen Kolleginnen und Kollegen am Institut für den fachlichen Austausch, die produktive Arbeitsatmosphäre und die sportlichen und gemütlichen Aktivitäten außerhalb der Arbeitszeit. Hervorheben möchte ich Stefan FLIXEDER und Bernhard BISCHOF. Gespräche mit euch waren stets eine Inspiration und Bereicherung für mich. Weiters danke ich meinem Bürokollegen Michael SCHWEGEL für die produktiven und ideenreichen, aber auch für die humorvollen und ziellosen Diskussionen.

Ein großer Dank gilt meiner Familie für den Rückhalt und die Möglichkeit, den hinter mir liegenden Weg überhaupt beschreiten zu können. Besonders möchte ich Emina NEŠIĆ danken für die detaillierten Korrekturen an dieser Arbeit. Schließlich danke ich meiner Frau Marinela. Vielen Dank aus tiefstem Herzen für deine großartige, jahrelange Unterstützung, dein Verständnis und deine immerwährende Liebe.



Die approbierte gedruckte Originalversion dieser Dissertation ist an der TU Wien Bibliothek verfügbar.
The approved original version of this doctoral thesis is available in print at TU Wien Bibliothek.

Kurzfassung

Heutige Prozessautomatisierungslösungen beruhen in hohem Maße auf programmierbaren und multifunktionalen Robotern, die die repetitiven und ermüdenden Verarbeitungsschritte in der Massenproduktion für den Menschen zum Teil übernehmen. Viele dieser Prozesse erfordern im Allgemeinen, dass der Roboter ein Werkzeug entlang eines geometrischen Pfades führt, welcher im kartesischen Raum definiert ist. Diese Aufgabe wird in der Regelungstechnik als *Pfadfolgeregelung* bezeichnet und tritt bei Prozessen wie z. B. Fräsen und Schneiden auf.

Die vorliegende Arbeit widmet sich der Entwicklung eines neuen Konzeptes für die oberflächenbezogene Pfadfolgeregelung auf dreidimensionalen Werkstücken. Im Gegensatz zur klassischen Pfadfolgeregelung berücksichtigt das vorgestellte Regelungskonzept systematisch den Oberflächennormalenvektor der zugrundeliegenden dreidimensionalen Freiformoberfläche sowie den Pfadtangentenvektor des oberflächenbezogenen Pfades. Für die Interaktion mit der Oberfläche werden zwei unterschiedliche Koordinatensysteme für den Kontaktpunkt eingeführt, nämlich das *natürliche* und das *parallele* Koordinatensystem. Unter Verwendung einer Koordinatentransformation und einer Zustandsrückführung wird die Dynamik des nichtlinearen Robotersystems bezüglich eines nichtlinearen Pfades in ein System mit linearem Eingangs-/Ausgangsverhalten in den neuen pfadbezogenen Koordinaten transformiert. Diese berücksichtigen die zugrundeliegende dreidimensionale Freiformoberfläche, womit eine Impedanzregelung, Admittanzregelung und Kraftregelung in den neuen Koordinaten formuliert werden kann. Darüber hinaus werden industrielle Prozesse auf dreidimensionalen Freiformoberflächen in Bezug auf kinematische Einschränkungen, d. h. verbotene Werkzeugbewegungen, und kinematische Redundanzen, das sind freie Selbstbewegungen des Werkzeugs, beschrieben.

Das Regelungskonzept wird experimentell anhand eines neuen Ansatzes für das flexible Aufkleben von zugeschnittenen (kurvigen) Klebebändern auf dreidimensionale Freiformoberflächen validiert. Der experimentelle Aufbau für einen Demonstrator geht aus einer ausführlichen Konzeptstudie hervor. Beim Aufklebeprozess wird eine impedanzgeregelte Drapierrolle über das dreidimensionale Objekt geführt, ohne diese um den Oberflächennormalenvektor zu drehen. Dies verhindert die Faltenbildung im aufgeklebten Streifen. Die experimentellen Ergebnisse mit einem KUKA LBR iiwa 14 R820 zeigen die hohe Qualität des vorgestellten Ansatzes.

Die in dieser Arbeit vorgestellte oberflächenbezogene Pfadfolgeregelung ist ein allgemeines und modulares Konzept, mit dem verschiedene industrielle Prozesse auf dreidimensionalen Freiformoberflächen mit unterschiedlichen kinematischen und dynamischen Eigenschaften beschrieben und ausgeführt werden können, wie z. B. Polieren, Schweißen, Laserschneiden, Nähen und Spritzlackieren.



Die approbierte gedruckte Originalversion dieser Dissertation ist an der TU Wien Bibliothek verfügbar.
The approved original version of this doctoral thesis is available in print at TU Wien Bibliothek.

Abstract

Today, process automation solutions strongly rely on programmable and multi-functional robotic manipulators to perform repetitive and for the human operator partly tedious processing tasks for large-scale series productions. Many of these processes require the movement of a robot-mounted tool along a given geometric path defined in the Cartesian space. From a control engineering perspective, this task is called *path following control* and emerges in processes such as milling and cutting.

The work at hand is concerned with the development of a novel surface-based path following control concept for the processing of 3D objects. In contrast to classical path following control, the presented control concept systematically takes into account the surface normal vector of an underlying freeform 3D surface and the path tangent vector of the surface-based path. For the interaction with the target 3D object, two distinct coordinate frames are introduced, i. e. the *natural* and the *parallel* contact frame. Using a coordinate transformation and feedback linearization, the nonlinear robotic system dynamics is transformed into a system with linear input/output behavior in new path-based coordinates. The underlying surface is systematically incorporated into this concept, which allows to formulate impedance control, admittance control, and force control in the new coordinates. Moreover, industrial processes on freeform 3D surfaces are described in terms of kinematic constraints, i. e. forbidden tool motions, and kinematic redundancies, i. e. free self-motions of the tool.

The control concept is validated experimentally by a novel approach for the versatile application of (curved) pre-cut adhesive tapes on freeform 3D surfaces. The experimental design of the demonstrator results from a thorough concept study. In this process, an impedance-controlled draping roll traverses the target 3D object without turning around the surface normal vector to prevent wrinkles. Experimental results with a KUKA LBR iiwa 14 R820 demonstrate the high quality of the proposed approach.

Surface-based path following control is a general and modular framework to describe and perform various industrial processes on freeform 3D surfaces with diverse kinematic and dynamic requirements, e. g., polishing, laser cutting, sewing, and spray painting.



Die approbierte gedruckte Originalversion dieser Dissertation ist an der TU Wien Bibliothek verfügbar.
The approved original version of this doctoral thesis is available in print at TU Wien Bibliothek.

Contents

1	Introduction	1
1.1	Industrial Processes on 3D Objects	1
1.2	Handling of Deformable Materials	2
1.3	Aim of this Work	4
1.4	Outline of this Thesis	5
2	Mathematical Model of a 7-Axis Collaborative Robot	7
2.1	Kinematics	7
2.1.1	Homogeneous Transformations	7
2.1.2	Forward Kinematics	8
2.1.3	Manipulator Jacobian	10
2.1.4	Inverse Kinematics	11
2.2	Dynamics	12
2.3	Singular Perturbation Theory	13
3	Surface-Based Path Following Control	15
3.1	Overview	16
3.2	Paths on Surfaces	17
3.2.1	Surfaces	17
3.2.2	Paths	18
3.2.3	Ribbons	18
3.2.4	Paths and Vector Fields on Surfaces	19
3.2.5	Straight Paths: Geodesics	20
3.2.6	Curved Paths	21
	Curved Planar Paths	21
	Curved Paths on Freeform Surfaces	22
3.3	Surface-Based Frames and Coordinate Transformations	23
3.3.1	Natural Contact Frame	23
	Natural Projection Operator	24
	Tangential Subsystem	24
	Transversal Subsystem	25
	Orientation Subsystem	25
	Coordinate Transformation	26
3.3.2	Parallel Contact Frame	26
	Parallel Projection Operator	27
	Tangential Subsystem	28
	Transversal Subsystem	28
	Orientation Subsystem	29

Contents

	Coordinate Transformation	29
3.4	Feedback Linearization	31
3.5	Task Space Controller	31
3.5.1	Impedance Control	32
	Decoupled Error Dynamics	32
	Compliance Control	32
	Path-Dependent Controller Parameters	33
3.5.2	Admittance Control	34
3.5.3	Force Control	35
3.5.4	Hybrid Control Concepts	35
3.6	Hierarchical Nullspace Controller	36
3.6.1	Single-Axis Tool Redundancy	36
3.6.2	Level 1: Joint Limits and Stabilization of the Redundant Axis	37
3.6.3	Level 2: Elbow Stabilization	38
3.7	Path Progress	39
3.7.1	Autonomous Mode	40
3.7.2	Cooperative Mode	40
3.7.3	Cooperative Mode: Gesture Control	41
3.7.4	Collaborative Mode	42
4	Concept Study on Tape Application	43
4.1	Process Analysis	44
4.1.1	Problem Statement	44
4.1.2	Process Steps	44
	Contouring	45
	Application	46
4.1.3	Robot Employment and Kinematics	47
4.2	Concepts	49
4.2.1	Shape-Adaptive Gripper	49
4.2.2	Shape-Adaptive Table	49
4.2.3	Tape Dispenser Tool	50
	Supply at End-Effector	50
	Stationary Supply	50
4.2.4	Stationary Tape Dispenser	50
	Liner	50
	Conveyor Belt	51
4.2.5	Roll-Up Tool	51
4.2.6	Multi-Robot Cell	51
4.2.7	Additive Methods	52
	Unit Patch Application	52
	3D Printing	53
4.3	Evaluation	53
4.4	Discussion	58
4.4.1	Concept Selection	59
4.4.2	Limitations and Remedies	59
5	Application of Curved Tapes on 3D Objects	61
5.1	Experimental Setup	62

5.1.1	Coordinate Frames	62
5.1.2	Tape Application Tool	62
5.1.3	Characteristics	64
5.2	Process Overview	64
5.3	Tape Application Paths	65
5.4	Tape Application Controller	65
5.4.1	External Tool Kinematics	66
5.4.2	Controller Design	67
	Kinematic Constraints	67
	Coordinate Transformation	67
	Single-Axis Tool Redundancy and Feedback Linearization	68
	Task Space Controller	68
	Nullspace Controller	69
5.4.3	Optimal Initial Robot Pose	69
5.5	Implementation	71
5.5.1	Robot Control	71
5.5.2	Discrete Surfaces	72
5.5.3	Optimal Robot/Tool Position	73
	Robot/Tool Kinematics	74
	Optimization Problem	74
	Demonstrator Target 3D Object	75
5.5.4	Discrete Tape Application Paths	77
5.5.5	Discrete Surface-Based Path Following Control	79
	Discrete-time Parallel Contact Frame	79
	Discrete-time Parallel Projection Operator	80
5.5.6	Contact Force Estimation	80
5.6	Experimental Results	81
5.6.1	Straight Tape	82
5.6.2	Curved Tape	85
5.6.3	Discussion	87
6	Conclusions and Outlook	89
6.1	Conclusions	90
6.2	Outlook	92
A	Parameters	95
A.1	Kinematic Parameters	95
A.2	Controller Parameters	95
	Bibliography	97



Die approbierte gedruckte Originalversion dieser Dissertation ist an der TU Wien Bibliothek verfügbar.
The approved original version of this doctoral thesis is available in print at TU Wien Bibliothek.

Nomenclature

Acronyms and Abbreviations

2D	2-Dimensional
3D	3-Dimensional
AFP	Automated Fiber Placement
APP	Advanced Ply Placement
ATL	Automated Tape Laying
AUV	Autonomous Underwater Vehicle
DoF	Degree of Freedom
F/T	Force/Torque
FDM	Fused Deposition Modeling
FPP	Fiber Patch Placement
FRP	Fiber-Reinforced Plastics
LOWFLIP	Low Cost Flexible Integrated Composite Process
NIC	Network Interface Card
NURBS	Non-Uniform Rational B-Spline
pHRI	physical Human Robot Interaction
SCARA	Selective Compliance Assembly Robot Arm
SRS	Spherical-Rotational-Spherical
TCP	Tool Center Point
TPU	Thermoplastic Polyurethane
TRL	Technology Readiness Level
TSP	Traveling Salesman Problem

General Notation

$a, \gamma, A, \Gamma, \dots$	scalars, sets
$\mathbf{a}, \boldsymbol{\gamma}, \dots$	vectors
$\mathbf{A}, \boldsymbol{\Gamma}, \dots$	matrices
$\mathbf{a}^T, \mathbf{A}^T$	transpose of vectors and matrices
A_{ij}	element in the i th row and j th column of the matrix \mathbf{A} with $i, j \in \mathbb{N}$
$\mathcal{A}, \mathcal{B}, \dots$	coordinate frames
\dot{a}	total derivative with respect to time
\ddot{a}	second-order total derivative with respect to time
$ \cdot $	absolute value of a scalar, cardinality of a set

Nomenclature

$\ \cdot\ $	Euclidean norm
$\ \cdot\ _\infty$	infinity norm
$(\cdot)'$	partial derivative of (\cdot) with respect to p
$(\cdot)''$	second-order partial derivative of (\cdot) with respect to p
$\frac{D}{dp}(\cdot)$	covariant derivative of (\cdot) with respect to p
\mathcal{C}^k	class of k -times continuously differentiable functions

Coordinate Frames

\mathcal{A}	planar tape frame
\mathcal{B}	robot base frame
\mathcal{C}	generic contact frame
\mathcal{C}_n	natural contact frame
\mathcal{C}_p	parallel contact frame
\mathcal{E}	end-effector frame
\mathcal{L}_i	frame of link i
\mathcal{O}	object frame
\mathcal{T}	tool frame
\mathcal{T}_i	frame of triangle i
\mathcal{W}	world (inertial) frame

Latin Symbols

$\mathbf{0}$	zero vector or zero matrix of appropriate dimension
\mathbf{A}	Projection matrix
b_i	barrier function, $i = 1, \dots, 7$
\mathbf{b}	vector of barrier functions
\mathbf{B}	motor inertia matrix
\mathbf{C}	CORIOLIS matrix
d	damping
$\mathbf{d}_{\mathcal{X}}^{\mathcal{Y}}$	origin of frame \mathcal{Y} with respect to frame \mathcal{X} , expressed in \mathcal{X}
\mathbf{D}	damping matrix
\mathbf{e}_i	coordinate frame unit vectors, $i = 1, 2, 3$
\mathbf{f}_e	external force
\mathbf{f}_p	gravitational payload force
\mathbf{f}_s	measured force
\mathbf{g}	vector of potential forces
$\mathbf{h}(\mathbf{q})$	forward kinematics function
$\mathbf{h}^{-1}(\mathbf{q})$	inverse kinematics function
$\mathbf{H}_{Ri,\varphi}$	homogeneous transformation describing a rotation around the local axis $i \in \{x, y, z\}$ by the angle φ
$\mathbf{H}_{Ti,\varphi}$	homogeneous transformation describing a translation along the local axis $i \in \{x, y, z\}$ by the distance d
$\mathbf{H}_{\mathcal{X}}^{\mathcal{Y}}$	homogeneous transformation of frame \mathcal{Y} with respect to frame \mathcal{X} , expressed in \mathcal{X}
\mathbf{I}	identity matrix of appropriate dimension

J	analytical Jacobian
J_g	geometric Jacobian
J_r	rotation part of the analytical Jacobian
J_t	translation part of the analytical Jacobian
k	stiffness
K	stiffness matrix
L	transformation matrix
m	mass
M	mass matrix
M_l	link inertia matrix
M_r	rotor inertia matrix
n	vector of CORIOLIS and gravitational forces
N_i	nullspace projection matrix, $i = 2, 3$
p	path parameter
P_t	set of path turning points
P	generic projection operator
P_n	natural projection operator
P_p	parallel projection operator
Q	set of inverse kinematics solutions
q	joint position
R_{x^y}	rotation matrix of frame \mathcal{Y} with respect to frame \mathcal{X} , expressed in \mathcal{X}
R_{i,φ}	Rotation matrix describing a rotation around the local axis $i \in \{x, y, z\}$ by the angle φ
s	surface parameter $\mathbf{s}^T = [s_1 \ s_2]$
t	time
T	time constant
T_s	sampling time
L	transformation matrix
u	rigid-body system torque input
U	coupling matrix
v	virtual input in path coordinates
Y_t	feasible neighborhood
y	output of the robotic system
y_r	rotation part of the output
y_t	translation part of the output

Greek Symbols

Γ_{jk}^i	CHRISTOFFEL symbols of the surface σ , $i, j, k = 1, 2$
Γ	complete CORIOLIS matrix
θ	motor position
κ_g	geodesic curvature
κ_n	normal curvature

Nomenclature

Λ	complete mass matrix
π	path
π_g	geodesic position in the planar path
π_l	lateral position in the planar path
$\boldsymbol{\pi}$	parametrized path
σ	surface
$\boldsymbol{\sigma}$	parametrized surface
$\boldsymbol{\sigma}_n$	surface normal vector field (GAUSS map)
$\boldsymbol{\sigma}_{s_i}$	surface tangent vector fields, $i = 1, 2$
$\boldsymbol{\sigma}_{s_i s_j}$	second-order derivatives of the parametrized surface, $i, j = 1, 2$
τ	path torsion
$\boldsymbol{\tau}$	joint torques
$\boldsymbol{\tau}_e$	external generalized torques
$\boldsymbol{\tau}_f$	estimated friction torques
$\boldsymbol{\tau}_m$	motor torques
$\boldsymbol{\tau}_n$	nullspace control input torques
φ	angle between path tangent direction and x -axis
$\boldsymbol{\phi}$	minimal representation of an orientation, $\boldsymbol{\phi}^T = [\phi_1 \ \phi_2 \ \phi_3]$
$\boldsymbol{\phi}(\cdot)$	minimal representation of the rotation matrix \cdot
$\boldsymbol{\phi}_{ijk}(\cdot)$	minimal representation of the rotation matrix \cdot using convention ijk , with $i, j, k \in \{x, y, z\}$
ξ_1	tangential path coordinate
ξ_2, ξ_3	transversal path coordinates
ξ_4, ξ_5, ξ_6	orientation path coordinates
$\boldsymbol{\xi}_r$	rotation part of the output in path coordinates
$\boldsymbol{\xi}_t$	translation part of the output in path coordinates
ψ	elbow-plane angle
$\boldsymbol{\omega}_{\mathcal{X}}^{\mathcal{Y}}$	vector of angular velocities of frame \mathcal{Y} with respect to frame \mathcal{X} , expressed in \mathcal{X}

Diacritics

$\hat{\cdot}$	labeling a symbol \cdot in surface-based path coordinates
$\tilde{\cdot}$	labeling a modified symbol \cdot
$\underline{\cdot}$	labeling the lower limit of axis/joint \cdot
$\overline{\cdot}$	labeling the upper limit of axis/joint \cdot

Subscripts

k	referring to a time step $k \in \mathbb{N}$
-----	---

Superscripts

d	desired value
†	right pseudoinverse
*	optimal solution
p	desired value for a subordinate position controller

1

Introduction

In the past, industrial robots were manually programmed for simple pick-and-place tasks and to move a tool along a simple contour of a workpiece. Today, industrial robots are utilized for increasingly complex tasks and are equipped with a number of different sensors [1]. Sophisticated software suits for offline programming are available to plan and simulate complex coordinated movements for a large number of robots in fully automated production lines [2–5]. During execution, predominantly position control is used for the robot motion and, therefore, the robotic system cannot react adequately to disturbances or uncertainties, as for instance the underlying workpiece geometry is not always exactly known to the robot. The control of the interaction forces between the robot tool and the workpiece are is very important for a number of robotic applications.

1.1 Industrial Processes on 3D Objects

Industrial robots today are considered as re-programmable and multi-functional manipulators and 2.4 million units are in operation worldwide, as of 2018 [6]. Besides pick-and-place tasks, industrial robots are mainly utilized to perform industrial processes such as welding [7], glue application [8], application of gaskets and tapes [9], polishing [10], spraying [11], and sewing [12]. Complex processing trajectories are planned and calculated offline based on the CAD data of the workpiece. The robot motion is then fine-tuned and adjusted at the worksite using the robot teach pendant. Additionally, if the interaction forces between the robot tool and the workpiece have to be considered, the robot trajectory is adjusted manually to fulfill the required interaction forces [13, 14]. In most cases, the robot motion is planned in form of a position-based trajectory as a function of time and this planned motion is replayed without feedback from the environment [15].

In contrast, from the viewpoint of industrial robotics and classical automation, many processes require traversing a robot-mounted tool along a given geometric path with-

out *a priori* time parametrization [16]. This task is often called *path following control* or *contouring control* [17, 18] and emerges in many processes, as for instance in milling and cutting. Similarly, glue dispensing is a path following task where the dispensed material is directly related to the arc length of the path. In path following control, the current position along the path is determined using a projection operator. Transversal feedback linearization allows to linearize the (nonlinear) system with respect to the (nonlinear) path [19, 20]. The resulting system exhibits a linear input-output relation in the path coordinates, which allows to formulate well-known control strategies like force control or impedance control in these coordinates.

A suitable coordinate frame is needed to describe the robot motion with respect to the underlying geometry. Previous works use the FRENET-SERRET frame [21, 22] or the parallel transport frame [23–26]. Both frames are not suitable to traverse surfaces of 3D objects, since these frames are derived from the path directly and do not respect the normal vector field of an underlying surface. On the contrary, surface following control shown in [27] provides a distinct surface normal vector, but the local coordinate frame is derived from the surface only and does not take into account the path tangent vector. Many processes, e.g. cutting along contours of a freeform 3D surface and traversing a draping roll along a surface path on a 3D object, clearly require both components – the surface normal vector and the path tangent vector – for a feasible control strategy. Thus, novel control concepts are required to accurately describe and control the robot motion along a surface-based path.

The tool center point (TCP) is a virtual reference point of a robotic tool which is used for positioning a robot in the Cartesian space. The TCP is given as a transformation, i. e. a position offset and the orientation, relative to the tool mounting flange [15]. In industrial processes, the robot motion is determined by the desired motion of the TCP in the workspace of the robot. For example, in a sewing application, the TCP is the position and orientation of the presser foot of the sewing head. Many tools allow for free rotation around a given axis such as the motor axis of a polishing tool and the spray direction of a rotationally symmetric spray painting nozzle [10, 11]. Despite this additional degree of freedom for the robot motion provided by the tool, robot controllers still require to fully specify the desired motion of the TCP in terms of position and orientation. Hence, a systematic control approach to consider the existing kinematic redundancies and constraints is required in order to significantly increase the flexibility for industrial processes.

1.2 Handling of Deformable Materials

The term *deformable materials* refers to bodies which change their shape under the influence of gravity, friction forces or mating forces and torques. Shape changes include buckling, stretching, bending, twisting and volume changes in one or more spatial dimensions [28, 29]. Examples for deformable bodies are found in many industrial sectors, e.g. textile and apparel industry, automotive industry, food sector and paper industry, and encompass materials such as fabrics, carbon and glass fiber textiles, paper, foils, but also meat, cheese slices and cooked pasta [28]. In these sectors, the handling of deformable materials is a major task. For example, technical

textiles, like carbon and glass fiber fabrics and so-called prepregs, have to be handled for the production of fiber-reinforced plastics (FRP) components. Predominantly by manual labor, these components are manufactured by layering and draping multiple sheets of technical textiles onto a mold [30]. Stacking, destacking, transporting and draping processes are also required in the textile and apparel industry [31]. In the production of shirts, a large number of individual components have to be stacked, aligned and sewn together. The completed garments are ironed, folded and draped adequately before being packaged. Similar tasks appear in the shoe production [32], where the textile or leather part of the shoe, i. e. the so-called *upper*, is mostly manufactured using planar deformable parts. Afterwards, the upper is sewn to obtain its 3D shape and then draped on the shoe last, where the sole is applied. Handling of deformable materials also plays a significant role in the automotive industry, where many surfaces of the car interior are made of or are covered by textiles and similar handling tasks are required for the production [33].

Robotic handling of deformable materials in industry has been a challenging task for a long time [34, 35], and has received great attention in research recently [36]. The main challenges for the automated handling of deformable materials are their characteristics, in particular the nonlinear material behavior, the anisotropy, and the high-dimensional object state. The deformable components, especially in the textile and apparel industry, occur in various sizes with diverse outer contours and in a wide range of different materials with diverse material properties like porosity and density. The examples above illustrate various use cases for the handling of deformable materials. Processes in these sectors were optimized for manual labor and rely on the dexterity of the human hand and its sensing capabilities as well as the cognitive capabilities of the human operator [37–39]. Flexible automation on a human level has not yet been achieved for many handling tasks, e. g. grasping, de-stacking and draping [40, 41].

The most common approaches in the literature are advanced ply placement (APP) and fiber patch placement (FPP), where pre-cut deformable components are grasped and transported to the target 3D object and are then deposited and consolidated. Many specialized mechatronic gripper solutions for rather narrow use cases were implemented, see, e. g., [42–45]. In these solutions, areal gripping forces over the extent of the grasped object are applied in order to retain its geometric shape. In contrast, multi-point gripping for strip-like deformable components was implemented with three robots, where two are used for grasping and transporting and a third robot consolidates the strip with a draping roll [46]. For consolidation, additional sensors and compliant actuators mounted to the end-effectors are used to impose a defined compression force onto the surface, whereas the robots are position controlled. In [47], a force-controlled application of strip-like materials is demonstrated on a three-arm gantry robot based on a collaborative path following control concept. Similar to [46], two gripping arms grasp and transport a textile strip and the third arm is used for consolidation. The presented solution only solves the 2D case and the feasibility of a 3D implementation is yet to be researched on. Draping motions on freeform 3D surfaces are the focus of [40]. In this work, a pre-shearing step is performed, in which the areal textile component is preformed using a press mechanism. Afterwards, the deformable material is placed manually on the freeform 3D surface and the manually planned draping motions are executed by the robot. Two differently shaped draping

rolls and a “wedge” end-effector are used to perform the draping process onto a complex doubly-curved mold. The commercial solution SAMBA PRO [48] is able to place small textile fiber patches using two position-controlled robots. While a 6-axis industrial robot positions and orients the target 3D object, a selective compliance assembly robot arm (SCARA) with a soft gripper performs the patch placement. In this solution, however, the patch size as well as the wrapping angle are very limited.

Bjornsson et al. and Ward et al. [36, 49] state that pick-and-place systems as introduced above deliver only low output volumes and lack efficient and reliable end-effectors. Using pre-cut components as it is done in APP is difficult to integrate and requires planning far ahead [50]. Systems capable of dispensing deformable materials continuously have proven to be more successful in industry. These solutions do not involve a grasping and transporting step and the deformable material is precisely controlled by the end-effector. To this end, in automated tape laying (ATL) and automated fiber placement (AFP), highly specialized application and consolidation tools are used to mechanically place and thermally consolidate continuous tapes of technical textiles on freeform 3D surfaces [9]. These approaches are predominately used in the fiber-reinforced plastics (FRP) industry. Due to the tool size and weight, high-payload robots are required for the tool movement and the solutions are suitable for large and mostly convex surfaces only. Hence, brackets, ribs and spars are too small to be efficiently manufactured using an ATL or AFP approach. Also doubly-curved surfaces, tight corners and steep ramps are challenging to manufacture using these approaches [40, 51] and a minimal path length is required due to the design of the application tool [9]. A small-scale realization of ATL using a masking tape on 3D objects is shown in [52], which also includes 3D object scanning and robot motion planning. While [53] extends this demonstrator to support simple means of force control, it is only capable of dispensing continuous tapes on simple geodesic paths.

From the literature overview above, it is clear that versatile solutions for the application of pre-cut deformable components onto complex freeform 3D surfaces are still not available. Moreover, [54] even observes that handling of deformable materials is still “a manual process except for specialized solutions”. Björnsson et al. [36] state that there is a need for alternative approaches to ATL and AFP for small and complex shapes, which provide more flexibility with respect to the shape of the target 3D object and the deformable component. Furthermore, a systematic approach is required to control the interaction forces between the robot tool and the freeform 3D surface. Additionally, taking into account the kinematic redundancy of the robot tool has the potential to significantly improve the overall flexibility.

1.3 Aim of this Work

The aim of this work is to develop a novel control concept, called *surface-based path following control*, which extends classical path following control by incorporating an underlying freeform 3D surface into the control strategy. This control concept is able to describe the robot motion in surface-based path coordinates relative to a known surface and allows to systematically traverse a freeform 3D surface with a robot tool. Hence, the robot systematically considers the surface associated with the

path, the surface normal direction and the path tangent direction. These directions are used to accurately impose defined interaction forces and torques between the robot tool and the freeform 3D surface. Moreover, kinematic tool redundancies, like the rotation around the motor axis of a polishing tool, are also taken into account and provide additional flexibility for the robot motion. The algorithms and solutions emerging from this work are formulated in a generalized and modular way in order to be applicable to a large number of industrial processes on freeform 3D surfaces.

A further goal of this work is to demonstrate the developed methods on an *industrial process*. To this end, the novel control concept is implemented for the fast and flexible application of (curved) pre-cut adhesive tapes on freeform 3D surfaces. Initially, a concept study is conducted to evaluate the most suitable approach targeted on high accuracy and throughput, large wrapping angles, defined interaction forces during application and on small- to medium-sized 3D objects. A prototype for this industrial process is designed and the control concept proposed in this work is applied to generate the motion of the draping roll traversing the freeform 3D surface.

1.4 Outline of this Thesis

The remainder of this work is organized as follows:

Chapter 2 “[Mathematical Model of a 7-Axis Collaborative Robot](#)” first introduces the notation of homogeneous transformations and utilizes this concept to derive the forward and inverse kinematics and dynamics of the KUKA LBR iiwa 14 R820, which is employed throughout this work. This derivation results in a detailed dynamic robot model which also captures the elastic joint dynamics, but is not suitable for the controller design. To this end, singular perturbation theory is applied to separate the elastic joint dynamics from the robot link dynamics and obtain the quasi-static model in the standard form of a rigid-body model.

The main contribution of this work is Chapter 3 “[Surface-Based Path Following Control](#)”, in which the control concept to traverse a robot tool along a path defined on a surface is derived. First, the terms “path” and “surface” are introduced mathematically in a differential geometric setting and are then utilized to describe straight and curved paths on freeform 3D surfaces. Second, two distinct surface-based coordinate frames are defined, i. e. the natural contact frame and the parallel contact frame, which serve as a basis for the subsequent coordinate transformation and feedback linearization. This transformation is applied to the nonlinear rigid-body system with respect to a nonlinear surface-based path and yields a system with linear input-output behavior. Third, task space controllers and hierarchical nullspace controllers are formulated in the new surface-based path coordinates. In order to control the nullspace, a novel method to consider the single-axis tool redundancy is proposed in a general form. Finally, four different concepts for the robot motion along the surface-based path are presented, i. e. an autonomous mode, two cooperative modes, and a collaborative mode.

Chapter 4 “[Concept Study on Tape Application](#)” is a preparatory chapter, in which a concept for the fast and flexible application of deformable materials on small-

1 Introduction

and medium-sized 3D objects is developed. As a first step, the complete industrial process is analyzed and structured into the main processing steps, i. e. contouring and application, followed by general considerations on the robotic implementation. Ten distinct concepts for the application process are presented and contrasted to existing solutions in the literature and in industry. A qualitative evaluation of the proposed concepts is performed, which yields two most promising solutions.

In the following Chapter 5 “[Application of Curved Tapes on 3D Objects](#)”, the results of Chapter 3 are applied to the industrial process of Chapter 4 and implemented on the proposed experimental setup, which is based on the results of the previous chapter. As the two concepts with the highest score are related conceptually, a prototypical design for a tape application tool is proposed which incorporates the key aspects of both approaches. In this chapter, the experimental setup and the tape application process are described in detail. The tape application controller is adapted from the results of Chapter 3 to account for the peculiarities of the tape application process. Moreover, algorithms are presented to find the optimal robot/tool position and to determine the optimal initial robot pose for each deformable component to be applied onto the freeform 3D surface. Subsequently, the derived controller is implemented in discrete time on the computing hardware using discrete-space paths and surfaces. The surface-based path following control concept for the tape application process is validated experimentally on the KUKA LBR iiwa 14 R820 and the measurement results are discussed.

Finally, Chapter 6 “[Conclusions and Outlook](#)” summarizes this work and provides conclusions and an outlook on future research activities.

2

Mathematical Model of a 7-Axis Collaborative Robot

This chapter is concerned with the mathematical modeling of the collaborative robot KUKA LBR iiwa 14 R820, which is utilized throughout this work. This robot is a light-weight industrial manipulator which is designed for human-robot interaction [55] and comprises seven rotational degrees of freedom (DoF). Each joint is equipped with a torque sensor and a harmonic drive with a high gear ratio, which introduces significant elasticity into the drive train of each joint.

In the first section of this chapter, homogeneous transformations are introduced and this formulation is used to derive the forward kinematics, the manipulator Jacobian, and the inverse kinematics of the KUKA LBR iiwa 14 R820. Subsequently, the complete dynamical model, which also considers the elastic joint dynamics, is derived. As this model is too complex for the controller design, certain coupling terms are neglected to obtain the reduced model. Finally, singular perturbation theory is applied, which leads to a model in the form of a standard rigid-body system.

2.1 Kinematics

In this section, homogeneous transformations are introduced and the basic kinematic relations for the forward and inverse kinematics, as well as the manipulator Jacobian are derived for the KUKA LBR iiwa 14 R820.

2.1.1 Homogeneous Transformations

A homogeneous transformation $\mathbf{H}_{\mathcal{X}}^{\mathcal{Y}}$ describes the geometric relation of the coordinate frame \mathcal{Y} with respect to \mathcal{X} (expressed in \mathcal{X}) and contains the position of the

origin $\mathbf{d}_x^y \in \mathbb{R}^3$ and the orthogonal rotation matrix $\mathbf{R}_x^y \in \text{SO}(3)$

$$\mathbf{H}_x^y = \begin{bmatrix} \mathbf{R}_x^y & \mathbf{d}_x^y \\ \mathbf{0} & 1 \end{bmatrix}. \quad (2.1)$$

Using the properties of rotation matrices

$$\left(\mathbf{R}_x^y\right)^{-1} = \left(\mathbf{R}_x^y\right)^T = \mathbf{R}_y^x, \quad (2.2)$$

the inverse of (2.1) is found as

$$\left(\mathbf{H}_x^y\right)^{-1} = \begin{bmatrix} \left(\mathbf{R}_x^y\right)^{-1} & -\left(\mathbf{R}_x^y\right)^{-1}\mathbf{d}_x^y \\ \mathbf{0} & 1 \end{bmatrix} = \begin{bmatrix} \mathbf{R}_y^x & -\mathbf{R}_y^x\mathbf{d}_x^y \\ \mathbf{0} & 1 \end{bmatrix} = \mathbf{H}_y^x. \quad (2.3)$$

Thus, the inverse transformation \mathbf{H}_x^y describes the coordinate frame \mathcal{X} with respect to \mathcal{Y} , expressed in \mathcal{Y} . Here and in the following, the symbol $\mathbf{0}$ denotes a zero vector or matrix of proper size. A coordinate frame \mathcal{C} with respect to a frame \mathcal{A} is given using successive transformations with an intermediate coordinate frame \mathcal{B} as

$$\mathbf{H}_A^C = \mathbf{H}_A^B \mathbf{H}_B^C. \quad (2.4)$$

In this work, a simple translation along the local axis $i \in \{x, y, z\}$ is denoted by $\mathbf{H}_{T_i, d}$, whereas a simple rotation around the local axis i by the angle φ is described by $\mathbf{H}_{R_i, \varphi}$. Finally, the rotation matrix of $\mathbf{H}_{R_i, \varphi}$ is denoted by $\mathbf{R}_{i, \varphi}$.

2.1.2 Forward Kinematics

Robots with serial kinematics are described using successive homogeneous transformations $\mathbf{H}_{\mathcal{L}_{i-1}}^{\mathcal{L}_i}$. The coordinate frames \mathcal{L}_i are chosen such that the axis z_i coincides with the corresponding axis of joint i . The kinematic relation between two successive coordinate frames \mathcal{L}_{i-1} and \mathcal{L}_i is given by

$$\mathbf{H}_{\mathcal{L}_{i-1}}^{\mathcal{L}_i} = \mathbf{H}_{T_y, d_{i,y}} \mathbf{H}_{T_z, d_{i,z}} \mathbf{H}_{R_x, \alpha_i} \mathbf{H}_{R_z, q_i}, \quad (2.5)$$

with three parameters $d_{i,y}$, $d_{i,z}$ and α_i for each joint i and the joint position q_i . The coordinate frames and dimensions of the KUKA LBR iiwa 14 R820 are depicted schematically in Fig. 2.1 with the joint positions $\mathbf{q}^T = [q_1 \ q_2 \ \dots \ q_7]$. Note that the coordinate frame \mathcal{L}_0 corresponds to the robot base frame \mathcal{B} . Using (2.5) and the joint positions \mathbf{q} , the homogeneous transformation $\mathbf{H}_{\mathcal{W}}^{\mathcal{T}}(\mathbf{q})$ of the TCP frame (or tool frame), denoted by \mathcal{T} , with respect to the (inertial) world frame \mathcal{W} is calculated as

$$\mathbf{H}_{\mathcal{W}}^{\mathcal{T}}(\mathbf{q}) = \mathbf{H}_{\mathcal{W}}^{\mathcal{B}} \underbrace{\mathbf{H}_{\mathcal{B}}^{\mathcal{L}_1}(q_1) \mathbf{H}_{\mathcal{L}_1}^{\mathcal{L}_2}(q_2) \cdots \mathbf{H}_{\mathcal{L}_6}^{\mathcal{L}_7}(q_7) \mathbf{H}_{\mathcal{L}_7}^{\mathcal{E}}}_{\mathbf{H}_{\mathcal{B}}^{\mathcal{E}}(\mathbf{q})} \mathbf{H}_{\mathcal{E}}^{\mathcal{T}} = \begin{bmatrix} \mathbf{R}_{\mathcal{W}}^{\mathcal{T}}(\mathbf{q}) & \mathbf{d}_{\mathcal{W}}^{\mathcal{T}}(\mathbf{q}) \\ \mathbf{0} & 1 \end{bmatrix}, \quad (2.6)$$

where the forward kinematics of the robot itself is denoted by $\mathbf{H}_{\mathcal{B}}^{\mathcal{E}}(\mathbf{q})$. In (2.6), $\mathbf{H}_{\mathcal{L}_7}^{\mathcal{E}} = \mathbf{H}_{T_z, d_{8,z}}$ and $\mathbf{H}_{\mathcal{E}}^{\mathcal{T}}$ describes the (constant) homogeneous transformation from the robot end-effector (flange) frame \mathcal{E} to the TCP frame \mathcal{T} . The parameters for

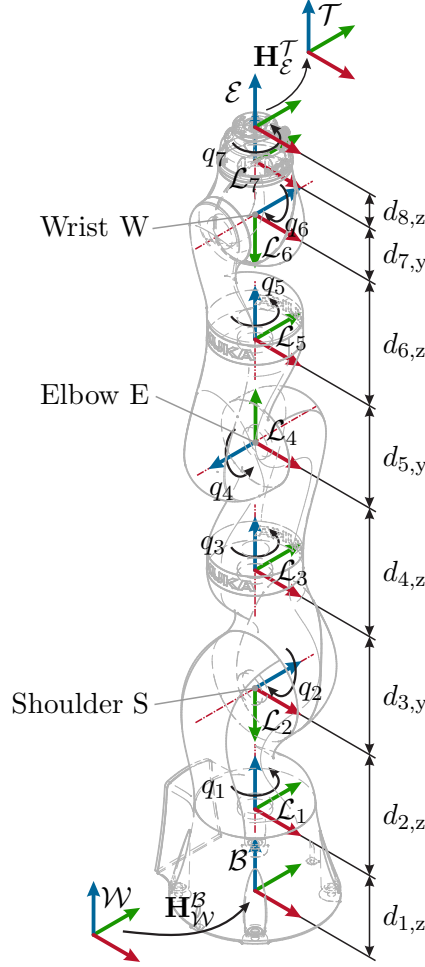


Figure 2.1: Coordinate frames, dimensions and distinct points of the KUKA LBR iiwa 14 R820.

all transformations $\mathbf{H}_{\mathcal{L}_{i-1}}^{\mathcal{L}_i}$, $i = 1, 2, \dots, 8$, are listed in Table A.1 of the Appendix. Based on (2.6), the forward kinematics of the robot is defined as, see Fig. 2.1,

$$\mathbf{y} = \begin{bmatrix} \mathbf{y}_t \\ \mathbf{y}_r \end{bmatrix} = \begin{bmatrix} \mathbf{d}_{\mathcal{W}}^{\mathcal{T}}(\mathbf{q}) \\ \phi(\mathbf{R}_{\mathcal{W}}^{\mathcal{T}}(\mathbf{q})) \end{bmatrix} = \begin{bmatrix} \mathbf{h}_t(\mathbf{q}) \\ \mathbf{h}_r(\mathbf{q}) \end{bmatrix} = \mathbf{h}(\mathbf{q}) \in \mathbb{R}^6, \quad (2.7)$$

with the Cartesian position $\mathbf{y}_t \in \mathbb{R}^3$ and the orientation $\mathbf{y}_r \in \mathbb{R}^3$ given as minimal representation $\phi(\mathbf{R}_{\mathcal{W}}^{\mathcal{T}}(\mathbf{q}))$ which is computed from the rotation matrix $\mathbf{R}_{\mathcal{W}}^{\mathcal{T}}(\mathbf{q})$. Minimal representations in the form

$$\phi = \begin{bmatrix} \phi_1 \\ \phi_2 \\ \phi_3 \end{bmatrix} = \phi_{ijk}(\mathbf{R}_{\mathcal{W}}^{\mathcal{T}}), \quad i, j, k \in \{x, y, z\} \quad (2.8)$$

use a sequence of three rotations, reading as

$$\mathbf{R}_{\mathcal{W}}^{\mathcal{T}}(\phi) = \mathbf{R}_{i,\phi_1} \mathbf{R}_{j,\phi_2} \mathbf{R}_{k,\phi_3}, \quad (2.9)$$

to represent the orientation. The two feasible conventions are the EULER angles, which use $i = k$ in (2.8), and the TAIT-BRYAN angles with $i \neq j \neq k$. Note that representations with $i = j$ or $j = k$ are degenerate and cannot be used to represent $\text{SO}(3)$.

2.1.3 Manipulator Jacobian

The geometric Jacobian $\mathbf{J}_g(\mathbf{q})$ establishes the relationship between the joint velocities $\dot{\mathbf{q}}$ and the translational and angular velocities in the task space in the form

$$\begin{bmatrix} \dot{\mathbf{y}}_t \\ \boldsymbol{\omega}_{\mathcal{W}}^{\mathcal{T}} \end{bmatrix} = \begin{bmatrix} \frac{\partial}{\partial \mathbf{q}} \mathbf{d}_{\mathcal{W}}^{\mathcal{T}} \\ \frac{\partial}{\partial \mathbf{q}} \boldsymbol{\omega}_{\mathcal{W}}^{\mathcal{T}} \end{bmatrix} \dot{\mathbf{q}} = \mathbf{J}_g(\mathbf{q}) \dot{\mathbf{q}}, \quad (2.10)$$

where $\dot{\mathbf{y}}_t$ is the translational velocity and $\boldsymbol{\omega}_{\mathcal{W}}^{\mathcal{T}}$ is the angular velocity of the tool frame \mathcal{T} with respect to the world frame \mathcal{W} . The latter is calculated via the skew-symmetric matrix operator $\mathbf{S}(\boldsymbol{\omega})$, which is defined for an angular velocity $\boldsymbol{\omega}^{\mathcal{T}} = [\omega_x \ \omega_y \ \omega_z]$ and the corresponding rotation matrix \mathbf{R} as

$$\mathbf{S}(\boldsymbol{\omega}) = \dot{\mathbf{R}}\mathbf{R}^{\mathcal{T}} = \begin{bmatrix} 0 & -\omega_z & \omega_y \\ \omega_z & 0 & -\omega_x \\ -\omega_y & \omega_x & 0 \end{bmatrix}. \quad (2.11)$$

Alternatively, the geometric Jacobian $\mathbf{J}_g(\mathbf{q})$ can also be derived using a geometric approach in which the contributions of each joint velocity to the translational and angular velocity in the task space are calculated [56].

In contrast, the analytical Jacobian $\mathbf{J}(\mathbf{q})$, denoted without index, is computed via differentiation of the forward kinematics (2.7) as

$$\dot{\mathbf{y}} = \begin{bmatrix} \dot{\mathbf{y}}_t \\ \dot{\mathbf{y}}_r \end{bmatrix} = \left(\frac{\partial \mathbf{h}}{\partial \mathbf{q}} \right) (\mathbf{q}) \dot{\mathbf{q}} = \begin{bmatrix} \mathbf{J}_t(\mathbf{q}) \\ \mathbf{J}_r(\mathbf{q}) \end{bmatrix} \dot{\mathbf{q}} = \mathbf{J}(\mathbf{q}) \dot{\mathbf{q}}. \quad (2.12)$$

It expresses the task space velocities $\dot{\mathbf{y}}$ in terms of the joint velocities $\dot{\mathbf{q}}$. Note that the time derivative of the orientation task space coordinates $\dot{\mathbf{y}}_r$ differs from the angular velocities $\boldsymbol{\omega}_{\mathcal{W}}^{\mathcal{T}}$. The relationship between $\dot{\mathbf{y}}_r$ and $\boldsymbol{\omega}_{\mathcal{W}}^{\mathcal{T}}$ is established with the transformation matrix $\mathbf{T}(\boldsymbol{\phi})$, given by [56]

$$\mathbf{T}(\boldsymbol{\phi}) = \frac{\partial}{\partial \boldsymbol{\phi}} \boldsymbol{\omega}_{\mathcal{W}}^{\mathcal{T}}, \quad (2.13)$$

in the form

$$\boldsymbol{\omega}_{\mathcal{W}}^{\mathcal{T}} = \mathbf{T}(\boldsymbol{\phi}) \dot{\boldsymbol{\phi}} = \mathbf{T}(\boldsymbol{\phi}) \dot{\mathbf{y}}_r, \quad (2.14)$$

and between the geometric Jacobian $\mathbf{J}_g(\mathbf{q})$ and the analytical Jacobian $\mathbf{J}(\mathbf{q})$ as

$$\mathbf{J}_g(\mathbf{q}) = \begin{bmatrix} \mathbf{I} & \mathbf{0} \\ \mathbf{0} & \mathbf{T}(\boldsymbol{\phi}) \end{bmatrix} \mathbf{J}(\mathbf{q}), \quad (2.15)$$

with the identity matrix \mathbf{I} of proper size. Note that the representation of the orientation in form of EULER angles $\boldsymbol{\phi}(\mathbf{R}_{\mathcal{W}}^{\mathcal{T}}(\mathbf{q}))$ gives rise to so-called *representation singularities* where the transformation matrix $\mathbf{T}(\boldsymbol{\phi})$ becomes singular, i. e. $\det(\mathbf{T}(\boldsymbol{\phi})) = 0$. A non-minimal representation $\mathbf{y}_r \in \mathbb{R}^d$ with $d > 3$, e. g. quaternions, can be used to avoid such singularities.

2.1.4 Inverse Kinematics

The considered robot KUKA LBR iiwa 14 R820 has seven DoF and, thus, is a redundant manipulator in the 3D Cartesian space, which is of dimension six. In contrast to 6-DoF robots, the solution of the inverse kinematics problem for the 7-DoF robot comprises multiple one-dimensional sets due to the kinematic redundancy. Hence, the robot can perform self-motions in the joint space without moving the tool frame \mathcal{T} .

The seven joints of the robot, depicted in Fig. 2.1, exhibit a special arrangement, where the first three axes and the last three axes intersect in the points S and W, respectively, representing two virtual spherical joints. Thus, a spherical shoulder S (joints 1, 2 and 3), an elbow (joint 4) and a spherical wrist W (joints 5, 6 and 7) are formed.

Including the revolute elbow joint, the kinematic chain of the robot is called SRS (spherical-revolute-spherical). In the literature, the term “anthropomorphic manipulator” is also encountered frequently, as the kinematic structure of the considered robot is similar to the human arm.

The inverse kinematics of (2.7) is formally denoted as

$$Q = \mathbf{h}^{-1}(\mathbf{y}) , \quad (2.16)$$

with the set of joint-space solutions Q for the given Cartesian position \mathbf{y} . While the inverse kinematics of a general 7-DoF kinematic chain can only be computed numerically, the special case of an SRS structure allows to calculate analytical solutions [57, 58]. The inverse kinematics of the SRS robot is solved in two steps [57]. First, the inverse kinematics is solved analytically for a virtual 6-axis manipulator, which emerges by setting $q_3 = 0$. This yields eight discrete solutions, denoted by \mathbf{q}_i , $i = 1, 2, \dots, 8$. In each of the eight resulting solutions, the shoulder S, the elbow E and the wrist W (see Fig. 2.1) span the so-called *reference plane*. Second, this reference plane is tilted by the angle ψ , called *elbow-plane angle*, from which the joint-space functions $\tilde{\mathbf{q}}_i(\psi)$ with $\psi \in \Psi = [-\pi, \pi)$ for $i = 1, 2, \dots, 8$ are found. Note that $\mathbf{q}_i = \tilde{\mathbf{q}}_i(0)$ for $i = 1, 2, \dots, 8$ holds. The set Q consists of eight one-parametric solution sets [57]

$$Q = \bigcup_{i=1}^8 Q_i \quad (2.17a)$$

$$Q_i = \{ \tilde{\mathbf{q}}_i(\psi) \mid \psi \in \Psi \} , \quad (2.17b)$$

with $i = 1, 2, \dots, 8$. Each set Q_i is the image of the elbow-plane angle $\psi \in \Psi$ under the joint-space function $\tilde{\mathbf{q}}_i(\psi)$. Similarly in [58], the inverse kinematics problem is solved using a geometric approach and utilizing quaternions for the orientation, while keeping $\nu_2 = \tan(\frac{\alpha_2}{2})$ as a free parameter.

For practical implementation of the inverse kinematics algorithm for the SRS robot structure, the computational costs in terms of the number of calculation operations and the running time are significant performance indicators. These aspects are considered in [59], where the computational performance of two implementations based on the approach of Pfuner [58] are compared – one based on homogeneous

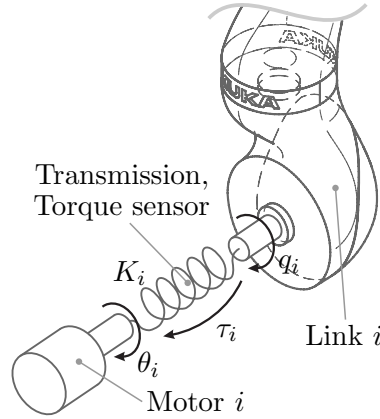


Figure 2.2: Schematic drawing of the drive train model of a single joint i .

transformations and one based on dual quaternions. This work shows that the computational performance is equivalent for both approaches for the forward kinematics, while the dual-quaternions implementation for the inverse kinematics is about 70 % slower compared to the implementation using homogeneous transformations.

2.2 Dynamics

The KUKA LBR iiwa 14 R820 is a light-weight robot, which is equipped with torque sensors and harmonic drives in each joint [55]. Due to the low mechanical stiffness of these components, this type of drive train exhibits significant joint elasticity, which has to be considered in the robot model. Additionally, high gear ratios of up to 160 result in high angular velocities of the motor rotors and, thus, their inertias cannot be neglected. Hence, the inertias of the motor rotors have to be included in the robot model. A schematic drawing of the drive train model of a single joint i is depicted in Fig. 2.2. Here and in the following, the motor position is denoted by θ_i , the joint torque is τ_i and K_i describes the (linear) joint stiffness, $i = 1, 2, \dots, 7$.

To this end, the *complete model*, which incorporates the joint elasticity and the motor rotor inertias of the seven joints, reads as [60]

$$\Lambda(\mathbf{q}) \begin{bmatrix} \ddot{\mathbf{q}} \\ \ddot{\boldsymbol{\theta}} \end{bmatrix} + \Gamma(\mathbf{q}, \dot{\mathbf{q}}) \begin{bmatrix} \dot{\mathbf{q}} \\ \dot{\boldsymbol{\theta}} \end{bmatrix} + \begin{bmatrix} \mathbf{g}(\mathbf{q}) - \mathbf{K}(\boldsymbol{\theta} - \mathbf{q}) \\ \mathbf{K}(\boldsymbol{\theta} - \mathbf{q}) \end{bmatrix} = \begin{bmatrix} \boldsymbol{\tau}_e \\ \boldsymbol{\tau}_m \end{bmatrix}, \quad (2.18)$$

with the *complete inertia matrix*

$$\Lambda(\mathbf{q}) = \begin{bmatrix} \mathbf{M}_l(\mathbf{q}) + \mathbf{M}_r(\mathbf{q}) & \mathbf{U}(\mathbf{q}) \\ \mathbf{U}^T(\mathbf{q}) & \mathbf{B} \end{bmatrix}, \quad (2.19)$$

where $\mathbf{M}_l(\mathbf{q})$ and $\mathbf{M}_r(\mathbf{q})$ are the inertia matrices of the links and the rotors, respectively, $\mathbf{B} = \text{diag}(B_1, B_2, \dots, B_7)$ denotes the diagonal matrix of the motor rotor inertias B_i , $i = 1, 2, \dots, 7$, and $\mathbf{U}(\mathbf{q})$ takes into account the couplings between the links and the motor rotors. Note that $\mathbf{U}(\mathbf{q})$ can be shown to be a strictly upper triangular matrix [60]. In (2.18), the motor positions $\boldsymbol{\theta}^T = [\theta_1 \ \theta_2 \ \dots \ \theta_7]$, the diagonal joint stiffness matrix $\mathbf{K} = \text{diag}(K_1, K_2, \dots, K_7)$, the motor torques $\boldsymbol{\tau}_m$, the generalized external torques $\boldsymbol{\tau}_e$, and the gravitational forces $\mathbf{g}(\mathbf{q})$ are introduced.

The *complete CORIOLIS matrix* $\Gamma(\mathbf{q}, \dot{\mathbf{q}})$ is not unique in general and its elements $\Gamma_{ij}(\mathbf{q}, \dot{\mathbf{q}})$ are chosen as

$$\Gamma_{ij}(\mathbf{q}, \dot{\mathbf{q}}) = \sum_{k=1}^{14} c_{ijk}(\mathbf{q}) \dot{z}_k \quad (2.20a)$$

$$c_{ijk}(\mathbf{q}) = \frac{1}{2} \left(\frac{\partial \Lambda_{ij}(\mathbf{q})}{\partial z_k} + \frac{\partial \Lambda_{ik}(\mathbf{q})}{\partial z_j} - \frac{\partial \Lambda_{kj}(\mathbf{q})}{\partial z_i} \right), \quad (2.20b)$$

with $\mathbf{z}^T = [\mathbf{q}^T \ \boldsymbol{\theta}^T] = [z_1 \ z_2 \ \dots \ z_{14}] \in \mathbb{R}^{14}$ and the CHRISTOFFEL symbols $c_{ijk}(\mathbf{q})$, $i, j, k = 1, 2, \dots, 14$. The first row of the complete robot model (2.18) describes the link dynamics with the joint position \mathbf{q} , while the second row accounts for the dynamics in the drive train with the motor position $\boldsymbol{\theta}$. These subsystems are coupled via the complete CORIOLIS matrix $\Gamma(\mathbf{q}, \dot{\mathbf{q}})$, the coupling matrix $\mathbf{U}(\mathbf{q})$ and the joint stiffness in the drive train

$$\boldsymbol{\tau} = \mathbf{K}(\boldsymbol{\theta} - \mathbf{q}) = [\tau_1 \ \tau_2 \ \dots \ \tau_7]^T. \quad (2.21)$$

The coupling matrix $\mathbf{U}(\mathbf{q})$ only represents loose coupling between the links and the motors. These couplings make the calculation of an inverse dynamics control extremely difficult. Moreover, the system is not input-state linearizable by *static* state feedback [61].

The complete model (2.18) is thus simplified under the assumption that the kinetic energy of each rotor is exclusively determined by its own rotation [62], neglecting the rotations due to the link motions. This assumption is justified for high gear ratios and leads to $\mathbf{U}(\mathbf{q}) = \mathbf{0}$. As a result, the complete inertia matrix $\boldsymbol{\Lambda}(\mathbf{q})$ in (2.19) is reduced to a block-diagonal matrix [60]. Hence, with (2.20), this simplification yields the *reduced model* in the form

$$\mathbf{M}(\mathbf{q})\ddot{\mathbf{q}} + \mathbf{n}(\mathbf{q}, \dot{\mathbf{q}}) = \mathbf{K}(\boldsymbol{\theta} - \mathbf{q}) + \boldsymbol{\tau}_e \quad (2.22a)$$

$$\mathbf{B}\ddot{\boldsymbol{\theta}} + \mathbf{K}(\boldsymbol{\theta} - \mathbf{q}) = \boldsymbol{\tau}_m, \quad (2.22b)$$

where the mass matrix $\mathbf{M}(\mathbf{q}) = \mathbf{M}_l(\mathbf{q}) + \mathbf{M}_r(\mathbf{q})$ and the vector of CORIOLIS and gravitational forces $\mathbf{n}(\mathbf{q}, \dot{\mathbf{q}}) = \mathbf{C}(\mathbf{q}, \dot{\mathbf{q}})\dot{\mathbf{q}} + \mathbf{g}(\mathbf{q})$ are introduced.

2.3 Singular Perturbation Theory

While the reduced model (2.22) is input-state linearizable, the control strategies based on this model are complex, sensitive to parameter variations and require time derivatives of the mass matrix $\mathbf{M}(\mathbf{q})$ and of the vector of CORIOLIS and gravitational forces $\mathbf{n}(\mathbf{q}, \dot{\mathbf{q}})$ [61]. To obtain a suitable model for the controller design, the singular perturbation theory is applied to the reduced model (2.22), see, e. g., [60, 62]. In the framework of the singular perturbation theory, the joint dynamics (2.22b) are assumed to be sufficiently fast compared to the link dynamics (2.22a) and the model (2.22) can be separated into a fast and a slow subsystem accordingly. Applying the control law, see [60],

$$\boldsymbol{\tau}_m = \mathbf{u} - \mathbf{K}_\tau(\boldsymbol{\tau} - \mathbf{u}) - \epsilon \mathbf{D}_\tau \dot{\boldsymbol{\tau}} \quad (2.23)$$

2 Mathematical Model of a 7-Axis Collaborative Robot

yields

$$\underbrace{(\mathbf{M}(\bar{\mathbf{q}}) + (\mathbf{I} + \mathbf{K}_\tau)^{-1} \mathbf{B})}_{\bar{\mathbf{M}}(\bar{\mathbf{q}})} \ddot{\bar{\mathbf{q}}} + \mathbf{n}(\bar{\mathbf{q}}, \dot{\bar{\mathbf{q}}}) = \mathbf{u} + \bar{\boldsymbol{\tau}}_e \quad (2.24)$$

as quasi-static model, with the new system input \mathbf{u} , the singular perturbation parameter $0 < \varepsilon \ll 1$ and the positive definite controller gain matrices \mathbf{K}_τ and \mathbf{D}_τ . In (2.24), the bar above the symbols indicates quasi-static variables, i. e. $\bar{\mathbf{q}}$ and $\bar{\boldsymbol{\tau}}_e$. Thus, the quasi-static model (2.24) represents a rigid-body model with the modified mass matrix $\bar{\mathbf{M}}(\bar{\mathbf{q}})$. Using this result, classical control strategies can be applied to robots with elastic joints. Note that the measurement of the joint torque $\boldsymbol{\tau}$ is required for the control law (2.23).

3

Surface-Based Path Following Control

In path following control, the robot motion is described by a geometric path in the task space of the robot and a path parameter which describes the progress of the motion along the path. Surface-based paths, in contrast to free paths in space, impose a distinct surface normal direction at each point along the path, which cannot be taken into account in classical path following control methods.

Processing surfaces of 3D objects is a frequent task occurring in industrial robotics, e. g. polishing, laser cutting, draping, spraying and grinding [10, 63]. All of these processes require the robot tool to maintain alignment with the distinct surface normal direction at each point on the target 3D object. Additionally, some processes, like cutting and sewing, require the tool orientation to be aligned with the path tangent. Other processes, like polishing and laser cutting, use tools with a rotational symmetry around the surface normal vector and, thus, the rotation around the surface normal vector becomes redundant. These examples illustrate that each process and tool imposes its own *kinematic constraints* and *kinematic redundancies* when interacting with a freeform 3D surface, which have to be maintained with high precision.

In the course of this chapter, surface-based path following control is developed, which allows to move a robot tool along a path defined on a surface, while considering the distinct surface normal vector and the path tangent vector. Additionally, the kinematic constraints and kinematic redundancies are systematically taken into account by the control approach. The robot motion is described using a surface-based coordinate frame for the interaction with the freeform 3D surface. Thus, the robot position and orientation as well as the interaction forces and torques are formulated in this coordinate frame and have a clear meaning with respect to the surface and the surface-based path. Using this approach, the robotic system systematically takes into account the surface to be processed and is able to deal with uncertainties in the

3 Surface-Based Path Following Control

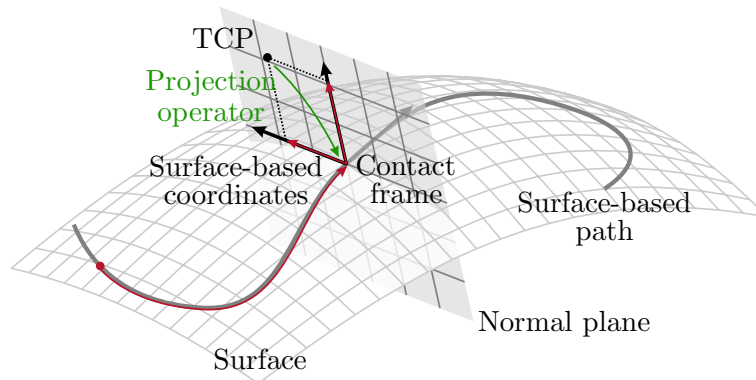


Figure 3.1: Basic components of the surface-based path following control concept.

freeform 3D surface during the process.

This chapter starts with a conceptual overview of the surface-based path following control. Subsequently, the fundamentals of paths on surfaces as well as surface-based frames are introduced in a differential geometric setting. Based on these frames, a coordinate transformation is derived, which is used in a feedback linearization to linearize the nonlinear robotic system with respect to the surface-based path. Afterwards, task space controllers and hierarchical nullspace controllers are described, which observe the kinematic constraints in the task space and allow for an adequate motion in the free axes of the nullspace. Finally, four different modes of operation with different time evolutions of the path parameter are discussed.

3.1 Overview

The basic components of the surface-based path following control concept are illustrated in Fig. 3.1. The surface-based path (thick dark gray line) has a distinct surface normal vector at each point along the path, which is derived from the underlying surface (light gray). The position of the TCP (black dot) is projected onto the surface-based path using a projection operator (green arrow), which determines the closest point on the path such that the TCP position lies on the normal plane (light gray plane). At the projected point, a contact frame (black arrows) is constructed from geometric components of the surface and the path, e.g. the surface normal vector and the path tangent vector. Based on this contact frame, a coordinate transformation and a feedback linearization are calculated, which linearize the robotic system in the new surface-based coordinates (red arrows). This allows to formulate standard controllers in these coordinates, as e.g. position, impedance or force controllers.

The contact frame provides distinct kinematic relations to the surface and, thus, rotations around specific axes of the contact frame can be either locked or left open for free motion. For example, a surface polishing tool is a motorized rotating disk, which is mounted on the robot flange. During the robot motion, the rotation around the motor axis of the polishing tool does not need to be specified and, thus, represents an additional redundancy to the robot motion, see Fig. 3.2a. Due to this kinematic redundancy, merely the motor axis has to be aligned with the surface normal direction, which means that the dimension of the task space is reduced

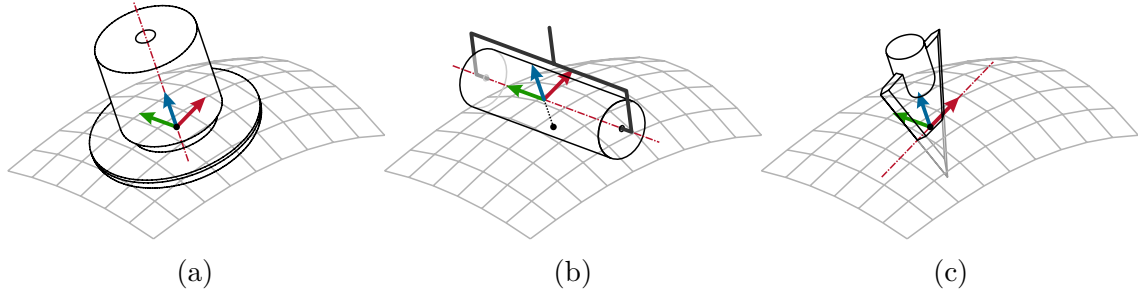


Figure 3.2: Examples for tools exhibiting a single-axis tool redundancy. (a) Polishing tool, (b) Draping tool, (c) Ultrasonic cutting tool.

by one. Similarly in Fig. 3.2b, a draping roll has a rotational symmetry around the draping roll axis and, thus, the contact point between the draping roll and the freeform 3D surface (black dot) may move freely on the circumference of the draping roll. Analogous to the first example, the rotation around the draping roll axis gives rise to an additional redundancy for the robot motion. A third example is shown in Fig. 3.2c for an ultrasonic cutting tool. The intersection between the blade and the freeform 3D surface is approximated by a line segment, around which free rotations are admissible to a limited extent. Kinematic relations of this type are called *single-axis tool redundancy* in this work and are discussed in detail in Section 3.6.1 “Single-Axis Tool Redundancy”.

3.2 Paths on Surfaces

Surface-based paths on freeform 3D surfaces are described as parametrized paths complemented with a surface normal vector field. In this section, the basics of surfaces, paths and ribbons are shortly summarized in terms of differential geometry. The definitions and relations are then used to calculate straight paths on freeform 3D surfaces, i. e. geodesics, and to map curved planar paths onto target 3D objects.

The basics presented in the following are mainly based on [21, 64] and the reader is referred to these texts for further details. Moreover, the arguments of some functions are omitted for clarity of presentation. The positions and orientations of all geometric objects are given with respect to the world frame \mathcal{W} .

3.2.1 Surfaces

A surface σ is given as a regular \mathcal{C}^3 parametrization $\sigma(\mathbf{s}) : U \subseteq \mathbb{R}^2 \mapsto \mathbb{R}^3$ with the surface parameter vector $\mathbf{s}^T = [s_1 \ s_2]$ from a subspace $U \subseteq \mathbb{R}^2$. The parametrization $\sigma(\mathbf{s})$ of a surface σ is called regular if $(\sigma_{s_1} \times \sigma_{s_2})(\mathbf{s}) \neq \mathbf{0} \ \forall \mathbf{s} \in U$, where $\sigma_{s_i} = \partial\sigma/\partial s_i$, $i = 1, 2$, are the surface tangent vectors. Equivalently, a regular parametrization has nonzero and linearly independent surface tangent vectors $\sigma_{s_i}(\mathbf{s})$, $i = 1, 2 \ \forall \mathbf{s} \in U$. Thus, for each regular surface parametrization $\sigma(\mathbf{s})$ there exists a unique unit normal vector field

$$\sigma_n(\mathbf{s}) = \frac{\sigma_{s_1}(\mathbf{s}) \times \sigma_{s_2}(\mathbf{s})}{\|\sigma_{s_1}(\mathbf{s}) \times \sigma_{s_2}(\mathbf{s})\|}, \quad (3.1)$$

which defines the so-called GAUSS map.

3.2.2 Paths

Analogous to the surface, a parametrized regular path is given by $\boldsymbol{\pi}(p) : I \subseteq \mathbb{R} \mapsto \mathbb{R}^3$, with the path parameter p defined on the interval $I \subseteq \mathbb{R}$. A regular parametrization fulfills the condition $\boldsymbol{\pi}'(p) \neq \mathbf{0} \forall p \in I$, where the derivative with respect to the path parameter p is denoted by $(\cdot)' = \frac{\partial}{\partial p}(\cdot)$. The arc length $l(p)$ of a path $\boldsymbol{\pi}(p)$ at p measured from a reference point p_0 is defined as

$$l(p) = \int_{p_0}^p \|\boldsymbol{\pi}'(\tilde{p})\| d\tilde{p} . \quad (3.2)$$

A special case for a path parametrization is the so-called *arc-length parametrization*, i. e. a parametrization with constant speed $\|\boldsymbol{\pi}'(p)\| = 1 \forall p \in I$. Any path $\boldsymbol{\pi}(p)$ can be parametrized its by arc length by using a regular reparametrization in the form $\tilde{\boldsymbol{\pi}}(l) = \boldsymbol{\pi}(p(l))$, where $p(l)$ is the inverse function of (3.2). This can be easily seen from

$$\|\tilde{\boldsymbol{\pi}}'(l)\| = \|\boldsymbol{\pi}'(p)\|p'(l) = \frac{\|\boldsymbol{\pi}'(p)\|}{l'(p)} = 1 , \quad (3.3)$$

where the relation $l'(p) = \|\boldsymbol{\pi}'(p)\|$ holds due to (3.2) and $p'(l) = \frac{1}{l'(p)}$ originates from the inverse function theorem [64].

Assumption 1. *Without loss of generality, all paths are assumed to be arc-length parametrized, i. e. $\|\boldsymbol{\pi}'(p)\| = 1 \forall p \in I$.*

3.2.3 Ribbons

A smooth unit vector field $\mathbf{n}(p)$ is called a unit normal field along $\boldsymbol{\pi}(p)$ if $\mathbf{n}(p) \perp \boldsymbol{\pi}'(p) \forall p \in I$. The conjunction of a parametrized path $\boldsymbol{\pi}(p)$ and a unit normal field $\mathbf{n}(p)$ is called a *ribbon* (or strip) $(\boldsymbol{\pi}(p), \mathbf{n}(p))$ [65]. Additionally, a so-called *adapted frame* $\mathbf{F}(p) = [\mathbf{t}(p) \ \mathbf{n}(p) \ \mathbf{b}(p)] \in \text{SO}(3)$ is defined for each ribbon $(\boldsymbol{\pi}(p), \mathbf{n}(p))$ with

$$\mathbf{t}(p) = \boldsymbol{\pi}'(p) \quad (3.4a)$$

$$\mathbf{b}(p) = \mathbf{t}(p) \times \mathbf{n}(p) . \quad (3.4b)$$

The evolution of an adapted frame $\mathbf{F}(p)$ along a ribbon $(\boldsymbol{\pi}(p), \mathbf{n}(p))$ with an arc-length parametrized path is governed by the *structure equations* with the unique functions for the normal curvature $\kappa_n(p)$, geodesic curvature $\kappa_g(p)$ and torsion $\tau(p)$ in the form [65]

$$\mathbf{F}'(p) = \mathbf{F}(p) \begin{bmatrix} 0 & -\kappa_n(p) & \kappa_g(p) \\ \kappa_n(p) & 0 & -\tau(p) \\ -\kappa_g(p) & \tau(p) & 0 \end{bmatrix} \quad (3.5)$$

or equivalently

$$\mathbf{t}' = \kappa_n(p)\mathbf{n} - \kappa_g(p)\mathbf{b} \quad (3.6a)$$

$$\mathbf{n}' = -\kappa_n(p)\mathbf{t} + \tau(p)\mathbf{b} \quad (3.6b)$$

$$\mathbf{b}' = \kappa_g(p)\mathbf{t} - \tau(p)\mathbf{n} . \quad (3.6c)$$

Note that $\kappa_n(p)$, $\kappa_g(p)$ and $\tau(p)$ are geometric quantities of the ribbon and are invariant under reparametrization or under a Euclidean motion, i. e. translation and

rotation in space. Conversely, the fundamental theorem for ribbons states, see, e. g., [65], that given these three functions, an arc-length parametrized path $\boldsymbol{\pi}(p)$ with a corresponding unit normal field $\mathbf{n}(p)$ can be calculated such that $\kappa_n(p)$, $\kappa_g(p)$ and $\tau(p)$ are the normal and geodesic curvature and the torsion of the ribbon $(\boldsymbol{\pi}(p), \mathbf{n}(p))$, respectively. The resulting ribbon is unique up to a Euclidean motion.

Finally, based on (3.6), three types of ribbons are defined. A ribbon $(\boldsymbol{\pi}(p), \mathbf{n}(p))$ is denoted as

- *asymptotic* ribbon if $\kappa_n(p) \equiv 0$,
- *geodesic* ribbon if $\kappa_g(p) \equiv 0$ and
- *curvature* ribbon if $\tau(p) \equiv 0$.

3.2.4 Paths and Vector Fields on Surfaces

Surface-based paths are fully described by so-called *natural ribbons* $(\boldsymbol{\pi}(p), \boldsymbol{\sigma}_n(\mathbf{s}(p)))$, which comprise the regularly parametrized path $\boldsymbol{\pi}(p) = \boldsymbol{\sigma}(\mathbf{s}(p))$ given on the surface and the corresponding GAUSS map $\boldsymbol{\sigma}_n(\mathbf{s}(p))$ of the parametrized surface $\boldsymbol{\sigma}(\mathbf{s})$. The path parametrization is regular if $\mathbf{s}'(p) \neq \mathbf{0} \forall p \in I$.

The covariant derivative $\frac{D}{dp}(\cdot)$ of a vector field $\mathbf{v}(p)$ along a surface-based path $\boldsymbol{\pi}(p)$ describes the rate of change of this vector field $\mathbf{v}(p)$ projected onto the tangential plane of the surface and is defined as [21]

$$\frac{D}{dp}\mathbf{v} := \mathbf{v}' - (\mathbf{v}' \cdot \boldsymbol{\sigma}_n)\boldsymbol{\sigma}_n. \quad (3.7)$$

A vector field $\mathbf{v}(p)$ defined along the surface-based path $\boldsymbol{\pi}(p)$ is *parallel*, if

$$\frac{D}{dp}\mathbf{v} = \mathbf{0} \quad \forall p \in I. \quad (3.8)$$

In the following, the covariant derivative for the special case of a surface tangent vector field $\mathbf{v}(p)$ is derived and is expressed in terms of the surface. The surface tangent vector field $\mathbf{v}(p)$ can be written as a linear combination of the local surface tangent vectors $\boldsymbol{\sigma}_{s_i}(\mathbf{s}(p))$, $i = 1, 2$, in the form

$$\mathbf{v}(p) = v_1(p)\boldsymbol{\sigma}_{s_1}(\mathbf{s}(p)) + v_2(p)\boldsymbol{\sigma}_{s_2}(\mathbf{s}(p)). \quad (3.9)$$

Inserting (3.9) into (3.7) yields

$$\begin{aligned} \frac{D}{dp}\mathbf{v} &= v_1'\boldsymbol{\sigma}_{s_1} + v_1\boldsymbol{\sigma}'_{s_1} + v_2'\boldsymbol{\sigma}_{s_2} + v_2\boldsymbol{\sigma}'_{s_2} \\ &\quad - \left((v_1'\underbrace{\boldsymbol{\sigma}_{s_1}}_{\perp\boldsymbol{\sigma}_n} + v_1\boldsymbol{\sigma}'_{s_1} + v_2'\underbrace{\boldsymbol{\sigma}_{s_2}}_{\perp\boldsymbol{\sigma}_n} + v_2\boldsymbol{\sigma}'_{s_2}) \cdot \boldsymbol{\sigma}_n \right) \boldsymbol{\sigma}_n \\ &= v_1'\boldsymbol{\sigma}_{s_1} + v_1\frac{D}{dp}\boldsymbol{\sigma}_{s_1} + v_2'\boldsymbol{\sigma}_{s_2} + v_2\frac{D}{dp}\boldsymbol{\sigma}_{s_2}. \end{aligned} \quad (3.10)$$

Next, the covariant derivatives $\frac{D}{dp}\boldsymbol{\sigma}_{s_1}$ and $\frac{D}{dp}\boldsymbol{\sigma}_{s_2}$ are formulated in terms of the surface using $\Gamma_{jk}^i(\mathbf{s}(p))$, $i, j, k = 1, 2$, with $\Gamma_{12}^1 = \Gamma_{21}^1$ and $\Gamma_{12}^2 = \Gamma_{21}^2$, as the CHRISTOFFEL symbols of the surface σ in the parametrization $\boldsymbol{\sigma}(\mathbf{s})$. With the second-order

3 Surface-Based Path Following Control

partial derivatives $\sigma_{s_i s_j} = \partial^2 \sigma / \partial s_i \partial s_j$, $i, j = 1, 2$, the covariant derivatives of the surface tangent vectors σ_{s_1} and σ_{s_2} read as [64]

$$\begin{aligned} \frac{D}{dp} \sigma_{s_1} &= \sigma'_{s_1} - (\sigma'_{s_1} \cdot \sigma_n) \sigma_n \\ &= \sigma_{s_1 s_1} s'_1 + \sigma_{s_1 s_2} s'_2 - ((\sigma_{s_1 s_1} s'_1 + \sigma_{s_1 s_2} s'_2) \cdot \sigma_n) \sigma_n \\ &= (\Gamma_{11}^1 \sigma_{s_1} + \Gamma_{11}^2 \sigma_{s_2}) s'_1 + (\Gamma_{12}^1 \sigma_{s_1} + \Gamma_{12}^2 \sigma_{s_2}) s'_2 \end{aligned} \quad (3.11)$$

and

$$\begin{aligned} \frac{D}{dp} \sigma_{s_2} &= \sigma'_{s_2} - (\sigma'_{s_2} \cdot \sigma_n) \sigma_n \\ &= \sigma_{s_2 s_1} s'_1 + \sigma_{s_2 s_2} s'_2 - ((\sigma_{s_2 s_1} s'_1 + \sigma_{s_2 s_2} s'_2) \cdot \sigma_n) \sigma_n \\ &= (\Gamma_{21}^1 \sigma_{s_1} + \Gamma_{21}^2 \sigma_{s_2}) s'_1 + (\Gamma_{22}^1 \sigma_{s_1} + \Gamma_{22}^2 \sigma_{s_2}) s'_2, \end{aligned} \quad (3.12)$$

where the GAUSS-CODAZZI equations were utilized in the last line of (3.11) and (3.12). The intermediate results (3.10), (3.11) and (3.12) are combined to obtain the covariant derivative (3.7) expressed in terms of the surface, reading as

$$\begin{aligned} \frac{D}{dp} \mathbf{v} &= (v'_1 + v_1 (s'_1 \Gamma_{11}^1 + s'_2 \Gamma_{12}^1) + v_2 (s'_1 \Gamma_{21}^1 + s'_2 \Gamma_{22}^1)) \sigma_{s_1} \\ &\quad + (v'_2 + v_1 (s'_1 \Gamma_{11}^2 + s'_2 \Gamma_{12}^2) + v_2 (s'_1 \Gamma_{21}^2 + s'_2 \Gamma_{22}^2)) \sigma_{s_2}. \end{aligned} \quad (3.13)$$

3.2.5 Straight Paths: Geodesics

Geodesics are arc-length parametrized straight paths π on a surface σ with $\kappa_g(p) \equiv 0$, i.e. these paths do not exhibit turns around the local surface normal vector σ_n . Equivalently, the path tangent $\pi'(p)$ of a geodesic is a parallel vector field as defined in (3.8). Straight surface-based paths on freeform 3D surfaces are described by geodesic ribbons $(\pi(p), \sigma_n(\mathbf{s}(p)))$, which are constructed from a geodesic path $\pi(p)$ and the corresponding GAUSS map $\sigma_n(\mathbf{s}(p))$. As the following theorem states, a geodesic is uniquely determined when given a starting point \mathbf{s}_0 on the surface and a tangent direction \mathbf{t}_0 .

Theorem 1 (Geodesics on freeform 3D surfaces). [64] *Given a starting point $\mathbf{s}_0^T = [s_{1,0} \ s_{2,0}]$ on the surface σ with the regular parametrization $\sigma(\mathbf{s})$ and a tangent direction $\mathbf{t}_0 = s'_{1,0} \sigma_{s_1} + s'_{2,0} \sigma_{s_2}$, with $\mathbf{t}_0 \perp \sigma_n(\mathbf{s}_0)$ at \mathbf{s}_0 , there is a unique geodesic $\pi(p)$, with $\pi(p_0) = \sigma(\mathbf{s}_0)$ and $\pi'(p_0) = \mathbf{t}_0$.*

Proof. Applying the covariant derivative in surface coordinates (3.13) to the path tangent vector field $\pi'(p)$, i.e. $\mathbf{v} = \pi' = s'_1 \sigma_{s_1} + s'_2 \sigma_{s_2}$, leads to

$$\begin{aligned} \frac{D}{dp} \pi' &= (s''_1 + s_1'^2 \Gamma_{11}^1 + 2\Gamma_{12}^1 s'_1 s'_2 + s_2'^2 \Gamma_{22}^1) \sigma_{s_1} \\ &\quad + (s''_2 + s_1'^2 \Gamma_{11}^2 + 2\Gamma_{12}^2 s'_1 s'_2 + s_2'^2 \Gamma_{22}^2) \sigma_{s_2}, \end{aligned} \quad (3.14)$$

where $\Gamma_{jk}^i = \Gamma_{kj}^i$ was used. To satisfy (3.8), both parentheses in (3.14) have to vanish individually, since the surface tangent vectors σ_{s_1} and σ_{s_2} are linearly independent for a regular surface parametrization $\sigma(\mathbf{s})$. Hence, this yields the initial

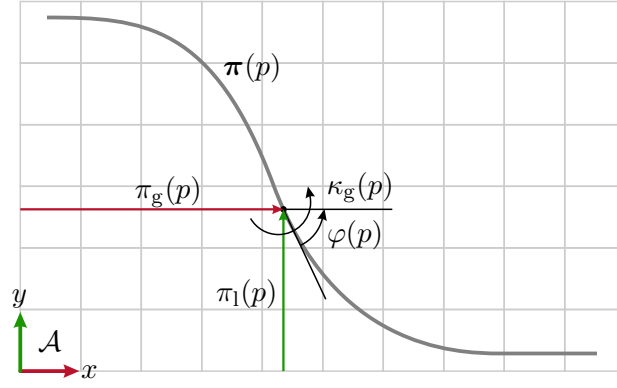


Figure 3.3: Geometric relations in the coordinate system of the planar path \mathcal{A} .

value problem

$$s_1'' = -s_1'^2 \Gamma_{11}^1 - 2\Gamma_{12}^1 s_1' s_2' - s_2'^2 \Gamma_{22}^1 \quad (3.15a)$$

$$s_2'' = -s_1'^2 \Gamma_{11}^2 - 2\Gamma_{12}^2 s_1' s_2' - s_2'^2 \Gamma_{22}^2, \quad (3.15b)$$

with the initial conditions

$$s_1(p_0) = s_{1,0} \quad s_1'(p_0) = s'_{1,0} \quad (3.16a)$$

$$s_2(p_0) = s_{2,0} \quad s_2'(p_0) = s'_{2,0}. \quad (3.16b)$$

The geodesic is obtained as solution of (3.15) with (3.16) and its uniqueness follows from the PICARD-LINDELÖF theorem, see [66] for more details. \square

3.2.6 Curved Paths

A curved path $\pi(p)$ on a freeform 3D surface can be computed using different approaches, e. g. interpolating points on the surface with sufficient smoothness [67], projecting planar curves onto the surface [68] or generating the curve from surface/plane intersections [69].

In this section, a novel approach to generate surface-based paths is presented, which maps a given planar path onto the freeform 3D surface such that the geometric shape of the path remains unchanged. To this end, the geometric quantities of a planar path are extracted and the surface-based path is constructed on the freeform 3D surface from these quantities. Thus, the planar and the surface-based path represent a matching pair of target lines [70].

Curved Planar Paths

The geometric relations for an arc-length parametrized planar path $\pi(p)$ in the planar coordinate system \mathcal{A} are depicted in Fig. 3.3. The shape of the planar path in \mathcal{A} is fully defined by the geodesic curvature $\kappa_g(p)$, which is calculated as [21]

$$\kappa_g(p) = \begin{bmatrix} 0 & 0 & 1 \end{bmatrix} (\boldsymbol{\pi}' \times \boldsymbol{\pi}''). \quad (3.17)$$

The location of each point $\pi(p)$ of the planar path is parametrized by the geodesic position $\pi_g(p)$ along the x -axis and by the lateral position $\pi_1(p)$ along the y -axis.

3 Surface-Based Path Following Control

The angle between the path tangent direction and the x -axis (see Fig. 3.3) is given by

$$\varphi(p) = \arccos\left(\begin{bmatrix} 1 & 0 & 0 \end{bmatrix} \boldsymbol{\pi}'\right) = \int_{p_0}^p \kappa_g(\tilde{p}) d\tilde{p} , \quad (3.18)$$

and is utilized to calculate the lateral and geodesic positions as

$$\pi_l(p) = \int_{p_0}^p \sin(\varphi(\tilde{p})) d\tilde{p} \quad (3.19)$$

$$\pi_g(p) = \int_{p_0}^p \cos(\varphi(\tilde{p})) d\tilde{p} . \quad (3.20)$$

Curved Paths on Freeform Surfaces

The geodesic position $\pi_g(p)$ along the path, the lateral position $\pi_l(p)$ relative to the path and the geodesic curvature $\kappa_g(p)$ are intrinsic geometric quantities of the path, which do not change under a reparametrization or under a Euclidean motion. These quantities also remain unchanged when the underlying path is mapped onto a freeform 3D surface using the geodesic curvature $\kappa_g(p)$. Thus, the surface-based path is constructed on the freeform 3D surface by imposing the geodesic curvature $\kappa_g(p)$ on the covariant derivative according to [64]

$$\left(\frac{D}{dp} \boldsymbol{\pi}'\right)(p) = \kappa_g(p) \left(\boldsymbol{\sigma}_n(\mathbf{s}(p)) \times \boldsymbol{\pi}'(p)\right) . \quad (3.21)$$

The right hand side of (3.21) is expressed in terms of surface variables as

$$\begin{aligned} \kappa_g(p) \left(\boldsymbol{\sigma}_n(\mathbf{s}(p)) \times \boldsymbol{\pi}'(p)\right) &= \kappa_g(p) \left(\frac{\boldsymbol{\sigma}_{s_1} \times \boldsymbol{\sigma}_{s_2}}{\|\boldsymbol{\sigma}_{s_1} \times \boldsymbol{\sigma}_{s_2}\|} \times (s_1' \boldsymbol{\sigma}_{s_1} + s_2' \boldsymbol{\sigma}_{s_2})\right) \\ &= \kappa_{s_1}(p) \boldsymbol{\sigma}_{s_1} + \kappa_{s_2}(p) \boldsymbol{\sigma}_{s_2} , \end{aligned} \quad (3.22)$$

with

$$\kappa_{s_1}(p) = \frac{-\kappa_g(p)}{\|\boldsymbol{\sigma}_{s_1} \times \boldsymbol{\sigma}_{s_2}\|} (s_1' \boldsymbol{\sigma}_{s_1} \cdot \boldsymbol{\sigma}_{s_2} + s_2' \boldsymbol{\sigma}_{s_2} \cdot \boldsymbol{\sigma}_{s_2}) \quad (3.23a)$$

$$\kappa_{s_2}(p) = \frac{\kappa_g(p)}{\|\boldsymbol{\sigma}_{s_1} \times \boldsymbol{\sigma}_{s_2}\|} (s_1' \boldsymbol{\sigma}_{s_1} \cdot \boldsymbol{\sigma}_{s_1} + s_2' \boldsymbol{\sigma}_{s_2} \cdot \boldsymbol{\sigma}_{s_1}) . \quad (3.23b)$$

Following the arguments of Theorem 1, a new system of ordinary differential equations for curved surface-based paths is obtained from (3.21) with (3.22) as

$$s_1'' = -s_1'^2 \Gamma_{11}^1 - 2\Gamma_{12}^1 s_1' s_2' - s_2'^2 \Gamma_{22}^1 + \kappa_{s_1}(p) \quad (3.24a)$$

$$s_2'' = -s_1'^2 \Gamma_{11}^2 - 2\Gamma_{12}^2 s_1' s_2' - s_2'^2 \Gamma_{22}^2 + \kappa_{s_2}(p) , \quad (3.24b)$$

and the initial values are given by (3.16). Thus, the surface-based path $\boldsymbol{\pi}(p)$ is steered locally using the path curvature $\kappa_g(p)$ via $\kappa_{s_1}(p)$ and $\kappa_{s_2}(p)$, and the solution of (3.24) is the unique surface-based path corresponding to a given starting point \mathbf{s}_0 and tangent direction \mathbf{t}_0 , which has the same geodesic curvature $\kappa_g(p)$ as the planar path. The resulting path $\boldsymbol{\pi}(p)$ complemented by the GAUSS map $\boldsymbol{\sigma}_n(\mathbf{s}(p))$ yields the natural ribbon $(\boldsymbol{\pi}(p), \boldsymbol{\sigma}_n(\mathbf{s}(p)))$, which fully describes the curved surface-based path.

3.3 Surface-Based Frames and Coordinate Transformations

The interaction between the robot tool and the target 3D object is governed by a contact frame. In this section, two different frames are developed, which are suited for a number of different applications. On the one hand, the *natural* contact frame \mathcal{C}_n is constructed from the path tangent vector and the surface normal vector and, thus, the frame orientation follows the path tangent. Sewing and ultrasonic cutting are example applications, which require the tool to be oriented along the processing path. On the other hand, the *parallel* contact frame \mathcal{C}_p comprises a parallel surface tangent vector and the surface normal vector. This construction prevents turns of the contact frame around the surface normal vector. For some applications, e. g. a draping process, this property is necessary to prevent wrinkles in the processed material. Additionally, a projection operator $P_n(\mathbf{y}_t)$ and $P_p(\mathbf{y}_t)$ is associated with the contact frames \mathcal{C}_n and \mathcal{C}_p , respectively.

For an application at hand, the suitable contact frame is chosen. The contact frame with its corresponding projection operator comprise the basis for a coordinate transformation. Using this coordinate transformation, the system output \mathbf{y} is uniquely transformed to the new path coordinates

$$\hat{\mathbf{y}} = \begin{bmatrix} \boldsymbol{\xi}_t \\ \boldsymbol{\xi}_r \end{bmatrix} = \begin{bmatrix} \xi_1 \\ \vdots \\ \xi_6 \end{bmatrix}, \quad (3.25)$$

with the position $\boldsymbol{\xi}_t \in \mathbb{R}^3$ and the orientation $\boldsymbol{\xi}_r \in \mathbb{R}^3$.

The following two subsections are devoted to the derivation of the natural contact frame \mathcal{C}_n and the parallel contact frame \mathcal{C}_p . At the beginning of each subsection, the respective frame and its corresponding projection operator are defined. Afterwards, the coordinates for the tangential, transversal and orientation subsystem are given, which are then combined to a coordinate transformation.

3.3.1 Natural Contact Frame

The natural contact frame $\mathcal{C}_n(p)$ is constructed from a given surface-based ribbon $(\boldsymbol{\pi}(p), \boldsymbol{\sigma}_n(\mathbf{s}(p)))$ and the path tangent vector $\boldsymbol{\pi}'(p)$ in the form

$$\begin{aligned} \mathbf{H}_{\mathcal{W}}^{\mathcal{C}_n}(p) &= \begin{bmatrix} \mathbf{e}_1(p) & \mathbf{e}_2(p) & \mathbf{e}_3(p) & \boldsymbol{\pi}(p) \\ 0 & 0 & 0 & 1 \end{bmatrix} \\ &= \begin{bmatrix} \boldsymbol{\pi}'(p) & \boldsymbol{\sigma}_n(\mathbf{s}(p)) \times \boldsymbol{\pi}'(p) & \boldsymbol{\sigma}_n(\mathbf{s}(p)) & \boldsymbol{\pi}(p) \\ 0 & 0 & 0 & 1 \end{bmatrix}. \end{aligned} \quad (3.26)$$

All three vectors $\mathbf{e}_i(p)$, $i = 1, 2, 3$, are unit vectors due to Assumption 1 and they compose a rotation matrix in $\text{SO}(3)$. Note the similarity of this rotation matrix to the adapted frame $\mathbf{F}(p)$ of Section 3.2.3 “Ribbons” for $\mathbf{n}(p) = \boldsymbol{\sigma}_n(\mathbf{s}(p))$. The geometric relations of the natural contact frame $\mathcal{C}_n(p)$ are illustrated in Fig. 3.4 for three points $p_0 < p^* < p_1$ along the path. The orientation of the natural contact

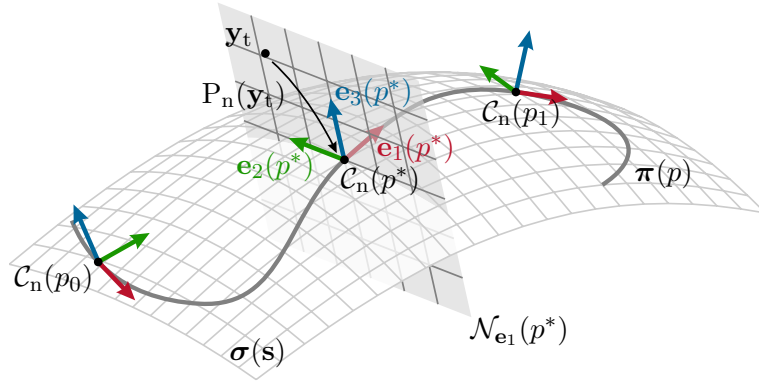


Figure 3.4: Geometric relations of the natural contact frame $\mathcal{C}_n(p)$.

frame $\mathcal{C}_n(p)$ maintains the surface normal vector and simultaneously follows the path tangent $\pi'(p)$.

Natural Projection Operator

As introduced in Section 3.1 “Overview”, a projection operator is used to determine the current position on the path, denoted by p^* . The natural projection operator $P_n(\mathbf{y}_t)$ for the natural contact frame $\mathcal{C}_n(p)$ is chosen as a minimum-distance criterion in the form [24]

$$p^* = P_n(\mathbf{y}_t) = \arg \min_{p \in I} \|\mathbf{y}_t - \pi(p)\|^2, \quad (3.27)$$

which determines the point $\pi(p^*)$ on the path π closest to \mathbf{y}_t with an orthogonal projection. The natural projection operator $P_n(\mathbf{y}_t)$ in (3.27) is formulated as an optimization problem and the corresponding first-order optimality condition reads as

$$(\mathbf{y}_t - \pi(p^*))^T \underbrace{\pi'(p^*)}_{=\mathbf{e}_1(p^*)} = 0, \quad (3.28)$$

i. e. the distance vector $\mathbf{y}_t - \pi(p^*)$ is orthogonal to the path tangent $\mathbf{e}_1(p^*) = \pi'(p^*)$ for the optimal solution p^* of (3.27). Thus, the distance vector $\mathbf{y}_t - \pi(p^*)$ lies in the normal plane $\mathcal{N}_{\mathbf{e}_1}(p^*) = \{\mathbf{x} \in \mathbb{R}^3 \mid \mathbf{x} - \pi(p^*) \perp \mathbf{e}_1(p^*)\}$, which underlines the geometric relations depicted in Fig. 3.4. Moreover, [24] shows that the optimization problem (3.27) exhibits a strict minimum in the feasible neighborhood given by the set

$$Y_t = \{\mathbf{y}_t \in \mathbb{R}^3 \mid \alpha(\mathbf{y}_t) < 1\}, \quad (3.29)$$

with

$$\alpha(\mathbf{y}_t) = (\mathbf{y}_t - \pi(p^*))^T \pi''(p^*). \quad (3.30)$$

The time derivative of the projected path parameter p^* in (3.27) is used as an intermediate result for the following subsections and is calculated from the time derivative of (3.28) using Assumption 1, $\beta(\mathbf{y}_t) = (1 - \alpha(\mathbf{y}_t))^{-1}$ and (2.12) as

$$\dot{p}^* = \beta(\mathbf{y}_t) \mathbf{e}_1^T(p^*) \mathbf{J}_t(\mathbf{q}) \dot{\mathbf{q}}. \quad (3.31)$$

Tangential Subsystem

A coordinate transformation for the new coordinates (3.25) is derived in the following, which is based on the natural contact frame $\mathcal{C}_n(p^*)$ and the natural projection operator $P_n(\mathbf{y}_t)$, see Fig. 3.5.

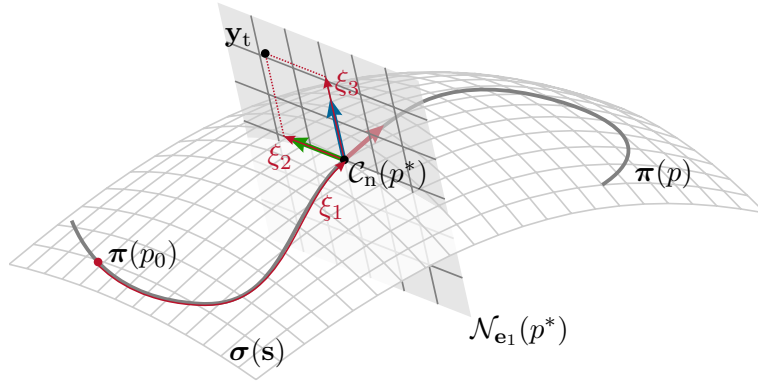


Figure 3.5: Coordinate transformation using the natural contact frame $\mathcal{C}_n(p)$.

The first coordinate ξ_1 is chosen as the arc length along the path, which simplifies to

$$\xi_1 = \int_{p_0}^{p^*} \|\pi'(p)\| dp = \int_{p_0}^{p^*} dp = p^* - p_0 \quad (3.32)$$

due to the assumed arc-length parametrization, see Assumption 1. Using (3.31), the time derivative of (3.32) is calculated as

$$\dot{\xi}_1 = \dot{p}^* = \beta(\mathbf{y}_t) \mathbf{e}_1^T(p^*) \mathbf{J}_t(\mathbf{q}) \dot{\mathbf{q}} . \quad (3.33)$$

Transversal Subsystem

The transversal coordinates ξ_2 and ξ_3 are chosen as projections of the distance vector $\mathbf{y}_t - \pi(p^*)$ onto the respective coordinate axis $\mathbf{e}_2(p^*)$ and $\mathbf{e}_3(p^*)$, reading as

$$\xi_i = \mathbf{e}_i^T(p^*) (\mathbf{y}_t - \pi(p^*)) , \quad i = 2, 3 . \quad (3.34)$$

Note that due to the special construction of the natural projection operator $P_n(\mathbf{y}_t)$, the distance vector $\mathbf{y}_t - \pi(p^*)$ lies in the normal plane $\mathcal{N}_{\mathbf{e}_1}(p^*)$ and ξ_3 measures the distance of the output \mathbf{y}_t to the surface along the surface normal vector $\sigma_n(\mathbf{s}(p))$. The velocities $\dot{\xi}_2$ and $\dot{\xi}_3$ are computed from (3.34) by time differentiation

$$\begin{aligned} \dot{\xi}_i &= (\mathbf{e}'_i(p^*))^T (\mathbf{y}_t - \pi(p^*)) \dot{p}^* + \mathbf{e}_i^T(p^*) \dot{\mathbf{y}}_t - \mathbf{e}_i^T(p^*) \underbrace{\pi'(p^*)}_{=\mathbf{e}_1(p^*)} \dot{p}^* \\ &= (\gamma_i(\mathbf{y}_t) \mathbf{e}_1^T(p^*) + \mathbf{e}_i^T(p^*)) \mathbf{J}_t \dot{\mathbf{q}} , \quad \underbrace{\quad}_{=0, \mathbf{e}_1 \perp \mathbf{e}_i} \end{aligned} \quad (3.35)$$

with

$$\gamma_i(p^*) = (\mathbf{e}'_i(p^*))^T (\mathbf{y}_t - \pi(p^*)) \beta(\mathbf{y}_t) \quad (3.36)$$

for $i = 2, 3$. Note that the expressions in (3.35) simplify due to the orthogonality of the basis vectors $(\mathbf{e}_1, \mathbf{e}_2, \mathbf{e}_3)$ of the natural contact frame $\mathcal{C}_n(p)$.

Orientation Subsystem

The three coordinates of the orientation subsystem ξ_r are chosen as the deviation of the orientation \mathbf{y}_r of the TCP frame \mathcal{T} from the orientation of the projected natural contact frame $\mathcal{C}_n(p^*)$, denoted as $\mathbf{c}_n(p^*)$ in minimal representation. Hence, the orientation subsystem ξ_r reads as

$$\xi_r = \mathbf{y}_r - \mathbf{c}_n(p^*) = \mathbf{h}_r(\mathbf{q}) - \mathbf{c}_n(p^*) , \quad (3.37)$$

3 Surface-Based Path Following Control

and the corresponding time derivative yields

$$\begin{aligned}\dot{\boldsymbol{\xi}}_r &= \dot{\mathbf{y}}_r - \mathbf{c}'_n(p^*)\dot{p}^* \\ &= \left(\mathbf{J}_r(\mathbf{q}) - \mathbf{c}'_n(p^*)\beta(\mathbf{y}_t)\mathbf{e}_1^T(p^*)\mathbf{J}_t(\mathbf{q}) \right) \dot{\mathbf{q}}.\end{aligned}\quad (3.38)$$

Coordinate Transformation

The results for the individual subsystems are assembled to a coordinate transformation to obtain the new coordinates $\hat{\mathbf{y}}$ and the time derivatives $\dot{\hat{\mathbf{y}}}$ in the form

$$\begin{bmatrix} \hat{\mathbf{y}} \\ \dot{\hat{\mathbf{y}}} \end{bmatrix} = \Phi(\mathbf{q}, \dot{\mathbf{q}})\quad (3.39)$$

as

$$\hat{\mathbf{y}} = \begin{bmatrix} \xi_1 \\ \xi_2 \\ \xi_3 \\ \boldsymbol{\xi}_r \end{bmatrix} = \begin{bmatrix} (3.32) \\ (3.34)|_{i=2} \\ (3.34)|_{i=3} \\ (3.37) \end{bmatrix}\quad (3.40a)$$

$$\dot{\hat{\mathbf{y}}} = \begin{bmatrix} \dot{\xi}_1 \\ \dot{\xi}_2 \\ \dot{\xi}_3 \\ \dot{\boldsymbol{\xi}}_r \end{bmatrix} = \begin{bmatrix} (3.33) \\ (3.35)|_{i=2} \\ (3.35)|_{i=3} \\ (3.38) \end{bmatrix} = \underbrace{\begin{bmatrix} \beta(\mathbf{y}_t)\mathbf{e}_1^T(p^*) & \mathbf{0} \\ \gamma_2(\mathbf{y}_t)\mathbf{e}_1^T(p^*) + \mathbf{e}_2^T(p^*) & \mathbf{0} \\ \gamma_3(\mathbf{y}_t)\mathbf{e}_1^T(p^*) + \mathbf{e}_3^T(p^*) & \mathbf{0} \\ -\mathbf{c}'_n(p^*)\beta(\mathbf{y}_t)\mathbf{e}_1^T(p^*) & \mathbf{I} \end{bmatrix}}_{\mathbf{L}(\mathbf{q})} \underbrace{\begin{bmatrix} \mathbf{J}_t(\mathbf{q}) \\ \mathbf{J}_r(\mathbf{q}) \end{bmatrix}}_{\mathbf{J}(\mathbf{q})} \dot{\mathbf{q}}.\quad (3.40b)$$

Note that the geometry of the surface-based path is incorporated in form of an additional transformation matrix $\mathbf{L}(\mathbf{q})$ in $\hat{\mathbf{J}}(\mathbf{q})$, cf. (2.12). The regularity of the transformation matrix $\mathbf{L}(\mathbf{q})$ in (3.40) is preserved for $\beta(\mathbf{y}_t) < \infty$, i.e. inside the feasible neighborhood Y_t of (3.29). In the same way as in [24], the coordinate transformation (3.40), with the nonsingular transformation matrix $\mathbf{L}(\mathbf{q})$, can be proven to be a \mathcal{C}^1 -diffeomorphism for a fully actuated 6-DoF robot.

3.3.2 Parallel Contact Frame

Parallel vector fields do not exhibit turns around the surface normal vector $\boldsymbol{\sigma}_n$, as stated in Section 3.2.4 “Paths and Vector Fields on Surfaces”. The parallel contact frame $\mathcal{C}_p(p)$ is constructed from a parallel vector field and the surface normal field $\boldsymbol{\sigma}_n$ and, thus, inherits this property. In the following, the parallel contact frame $\mathcal{C}_p(p)$ is derived, which is suitable for draping processes, where the draping roll must not turn around the surface normal vector to prevent wrinkles in the processed material.

For simplicity of the mathematical notation, the intermediate variable names and function names of the previous section ($\alpha(\mathbf{y}_t)$, $\beta(\mathbf{y}_t)$, \dot{p}^* , ...) are redefined in the following for the parallel contact frame. Subsequently, confusion will be avoided by referring to the corresponding equation.

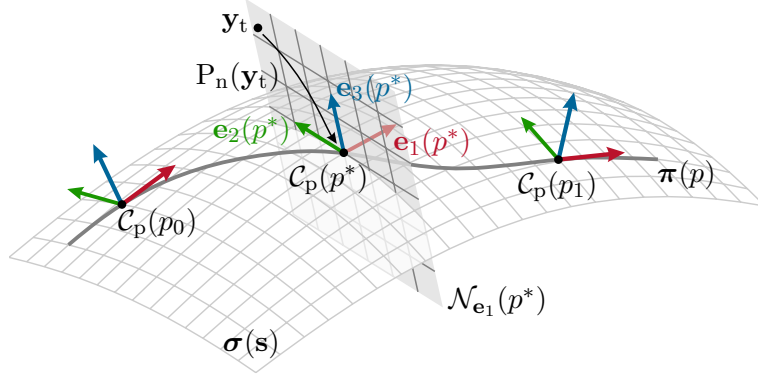


Figure 3.6: Geometric relations of the parallel contact frame $\mathcal{C}_p(p)$.

The first-order differential equations for the parallel unit vector field $\pi_p(p)$ are derived using (3.13) and (3.8) with $\mathbf{v} = \pi_p(p) = t_1(p)\boldsymbol{\sigma}_{s_1}(\mathbf{s}(p)) + t_2(p)\boldsymbol{\sigma}_{s_2}(\mathbf{s}(p))$. Following along the lines of Theorem 1 leads to

$$t'_1 = -t_1(s'_1\Gamma_{11}^1 + s'_2\Gamma_{12}^1) - t_2(s'_1\Gamma_{21}^1 + s'_2\Gamma_{22}^1) \quad (3.41a)$$

$$t'_2 = -t_1(s'_1\Gamma_{11}^2 + s'_2\Gamma_{12}^2) - t_2(s'_1\Gamma_{21}^2 + s'_2\Gamma_{22}^2), \quad (3.41b)$$

from which the parallel unit vector field $\pi_p(p)$ is calculated. The initial conditions $t_1(p_0)$ and $t_2(p_0)$ are chosen such that the vector field π_p is aligned with the path tangent $\pi'(p_0)$ at p_0 , i. e.

$$\pi_p(p_0) = \pi'(p_0). \quad (3.42)$$

Thus, with

$$\begin{aligned} \mathbf{H}_{\mathcal{W}}^{\mathcal{C}_p}(p) &= \begin{bmatrix} \mathbf{e}_1(p) & \mathbf{e}_2(p) & \mathbf{e}_3(p) & \boldsymbol{\pi}(p) \\ 0 & 0 & 0 & 1 \end{bmatrix} \\ &= \begin{bmatrix} \boldsymbol{\pi}_p(p) & \boldsymbol{\sigma}_n(\mathbf{s}(p)) \times \boldsymbol{\pi}_p(p) & \boldsymbol{\sigma}_n(\mathbf{s}(p)) & \boldsymbol{\pi}(p) \\ 0 & 0 & 0 & 1 \end{bmatrix}, \end{aligned} \quad (3.43)$$

the parallel contact frame $\mathcal{C}_p(p)$ is constructed. Similar to the previous section, the homogeneous transformation $\mathbf{H}_{\mathcal{W}}^{\mathcal{C}_p}(p)$ contains the three unit vectors $\mathbf{e}_i(p)$, $i = 1, 2, 3$, which constitute a rotation matrix in $\text{SO}(3)$. The parallel contact frame $\mathcal{C}_p(p)$ for a parametrized path $\boldsymbol{\pi}(p)$ is shown for three path positions $p_0 < p^* < p_1$ in Fig. 3.6, which illustrates the evolution of the parallel contact frame along the path while avoiding turns around the surface normal vector $\boldsymbol{\sigma}_n(\mathbf{s}(p))$.

Parallel Projection Operator

The parallel projection operator $P_p(\mathbf{y}_t)$ takes into account the orientation of the parallel contact frame $\mathcal{C}_p(p)$, which is determined by the surface normal vector $\mathbf{e}_3(p) = \boldsymbol{\sigma}_n(\mathbf{s}(p))$ and the parallel vector field $\mathbf{e}_1(p) = \boldsymbol{\pi}_p(p)$, cf. Fig. 3.6. Hence, the operator projects the output position \mathbf{y}_t onto the specific point $\boldsymbol{\pi}(p^*)$ on the path which satisfies the condition

$$(\mathbf{y}_t - \boldsymbol{\pi}(p^*))^T \underbrace{\boldsymbol{\pi}_p(p^*)}_{=\mathbf{e}_1(p^*)} = 0, \quad (3.44)$$

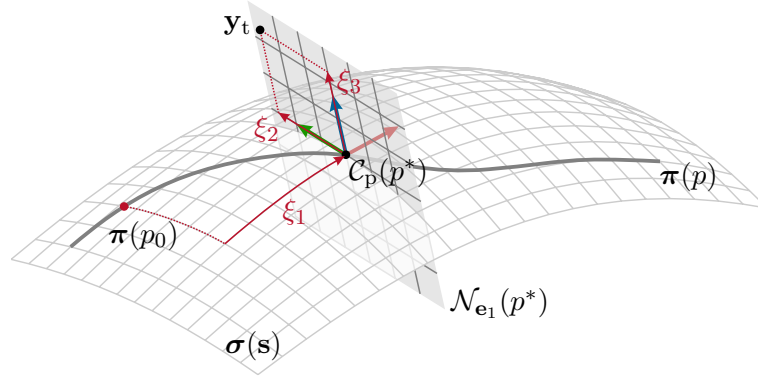


Figure 3.7: Coordinate transformation using the parallel contact frame $\mathcal{C}_p(p)$.

i. e. where the normal plane $\mathcal{N}_{\mathbf{e}_1}(p^*) = \{\mathbf{x} \in \mathbb{R}^3 \mid \mathbf{x} - \boldsymbol{\pi}(p^*) \perp \mathbf{e}_1(p^*)\}$ intersects the path, see Fig. 3.6. If multiple solutions to (3.44) exist, the position p^* with the smallest distance $\|\mathbf{y}_t - \boldsymbol{\pi}(p^*)\|$ is selected. Taking the time derivative of the constraint (3.44) and solving for \dot{p}^* yields

$$\dot{p}^* = \frac{\beta(\mathbf{y}_t)}{\mathbf{e}_1^T(p^*)\boldsymbol{\pi}'(p^*)} \mathbf{e}_1^T(p^*) \mathbf{J}_t(\mathbf{q}) \dot{\mathbf{q}}, \quad (3.45)$$

with

$$\beta(\mathbf{y}_t) = (1 - \alpha(\mathbf{y}_t))^{-1} \quad (3.46)$$

$$\alpha(\mathbf{y}_t) = \frac{(\mathbf{y}_t - \boldsymbol{\pi}(p^*))^T \mathbf{e}_1'(p^*)}{\mathbf{e}_1^T(p^*)\boldsymbol{\pi}'(p^*)}. \quad (3.47)$$

Tangential Subsystem

Using the parallel contact frame $\mathcal{C}_p(p)$ and the parallel projection operator $P_p(\mathbf{y}_t)$, a coordinate transformation is derived in the following to transform the system output \mathbf{y} to the new coordinates $\hat{\mathbf{y}}$ in the form of (3.25). The new coordinates are illustrated in Fig. 3.7 for the parallel contact frame $\mathcal{C}_p(p)$.

The tangential coordinate ξ_1 is chosen as the geodesic position $\pi_g(p^*)$ along the path. In terms of surface geometry this is

$$\xi_1 = \int_{p_0}^{p^*} (\boldsymbol{\pi}'(p))^T \mathbf{e}_1(p) dp, \quad (3.48)$$

with the time derivative, see (3.45),

$$\dot{\xi}_1 = (\boldsymbol{\pi}'(p^*))^T \mathbf{e}_1(p^*) \dot{p}^* = \beta(\mathbf{y}_t) \mathbf{e}_1^T(p^*) \mathbf{J}_t(\mathbf{q}) \dot{\mathbf{q}}. \quad (3.49)$$

Transversal Subsystem

The transversal coordinates ξ_2 and ξ_3 are calculated as the projection of the distance vector $\mathbf{y}_t - \boldsymbol{\pi}(p^*)$ onto the respective coordinate axis $\mathbf{e}_2(p^*)$ and $\mathbf{e}_3(p^*)$ using

$$\xi_i = \mathbf{e}_i^T(p^*) (\mathbf{y}_t - \boldsymbol{\pi}(p^*)), \quad i = 2, 3. \quad (3.50)$$

Note that the transversal coordinates take into account the surface normal direction and, thus, ξ_3 measures the distance of the output \mathbf{y}_t to the surface along the

surface normal vector $\boldsymbol{\sigma}_n(\mathbf{s}(p))$. The corresponding velocities are computed as time derivatives of (3.50) and read as

$$\dot{\boldsymbol{\xi}}_i = \left(\gamma_i(\mathbf{y}_t) \mathbf{e}_1^T(p^*) + \mathbf{e}_i^T(p^*) \right) \mathbf{J}_t(\mathbf{q}) \dot{\mathbf{q}} , \quad (3.51)$$

with

$$\gamma_i(\mathbf{y}_t) = \frac{\beta(\mathbf{y}_t)}{\mathbf{e}_1^T(p^*) \boldsymbol{\pi}'(p^*)} \left((\mathbf{e}_i'(p^*))^T (\mathbf{y}_t - \boldsymbol{\pi}(p^*)) - \mathbf{e}_i^T(p^*) \boldsymbol{\pi}'(p^*) \right) . \quad (3.52)$$

Orientation Subsystem

The orientation subsystem is defined in an analogous way as in the previous section, i. e. as rotational deviation of the tool frame \mathcal{T} from the projected parallel contact frame $\mathcal{C}_p(p^*)$. Using the orientation of $\mathcal{C}_p(p^*)$ in minimal representation, denoted by $\mathbf{c}_p(p^*)$, the orientation subsystem is chosen as

$$\boldsymbol{\xi}_r = \mathbf{y}_r - \mathbf{c}_p(p^*) = \mathbf{h}_r(\mathbf{q}) - \mathbf{c}_p(p^*) , \quad (3.53)$$

and its time derivative yields

$$\begin{aligned} \dot{\boldsymbol{\xi}}_r &= \dot{\mathbf{y}}_r - \mathbf{c}'_p(p^*) \dot{p}^* \\ &= \left(\mathbf{J}_r(\mathbf{q}) - \frac{\mathbf{c}'_p(p^*) \beta(\mathbf{y}_t) \mathbf{e}_1^T(p^*)}{\mathbf{e}_1^T(p^*) \boldsymbol{\pi}'(p^*)} \mathbf{J}_t(\mathbf{q}) \right) \dot{\mathbf{q}} . \end{aligned} \quad (3.54)$$

Coordinate Transformation

The intermediate results (3.48) to (3.54) for the positions and velocities of the new coordinates $\hat{\mathbf{y}}$ and $\dot{\hat{\mathbf{y}}}$, respectively, constitute a coordinate transformation of the structure (3.39) in the form

$$\hat{\mathbf{y}} = \begin{bmatrix} \boldsymbol{\xi}_1 \\ \boldsymbol{\xi}_2 \\ \boldsymbol{\xi}_3 \\ \boldsymbol{\xi}_r \end{bmatrix} = \begin{bmatrix} (3.48) \\ (3.50)|_{i=2} \\ (3.50)|_{i=3} \\ (3.53) \end{bmatrix} \quad (3.55a)$$

$$\dot{\hat{\mathbf{y}}} = \begin{bmatrix} \dot{\boldsymbol{\xi}}_1 \\ \dot{\boldsymbol{\xi}}_2 \\ \dot{\boldsymbol{\xi}}_3 \\ \dot{\boldsymbol{\xi}}_r \end{bmatrix} = \begin{bmatrix} (3.49) \\ (3.51)|_{i=2} \\ (3.51)|_{i=3} \\ (3.54) \end{bmatrix} = \underbrace{\begin{bmatrix} \beta(\mathbf{y}_t) \mathbf{e}_1^T(p^*) & \mathbf{0} \\ \gamma_2(\mathbf{y}_t) \mathbf{e}_1^T(p^*) + \mathbf{e}_2^T(p^*) & \mathbf{0} \\ \gamma_3(\mathbf{y}_t) \mathbf{e}_1^T(p^*) + \mathbf{e}_3^T(p^*) & \mathbf{0} \\ -\frac{\mathbf{c}'_p(p^*) \beta(\mathbf{y}_t) \mathbf{e}_1^T(p^*)}{\mathbf{e}_1^T(p^*) \boldsymbol{\pi}'(p^*)} & \mathbf{I} \end{bmatrix}}_{\mathbf{L}(\mathbf{q})} \underbrace{\begin{bmatrix} \mathbf{J}_t(\mathbf{q}) \\ \mathbf{J}_r(\mathbf{q}) \end{bmatrix}}_{\mathbf{J}(\mathbf{q})} \dot{\mathbf{q}} . \quad (3.55b)$$

Note that the structure of this coordinate transformation is equal to the previous section, cf. (3.39) and (3.40). The geometry of the surface-based path is governed by the transformation matrix $\mathbf{L}(\mathbf{q})$ for the parallel contact frame $\mathcal{C}_p(p^*)$ and, thus, the regularity of $\mathbf{L}(\mathbf{q})$ is a crucial property for this coordinate transformation. The transformation matrix $\mathbf{L}(\mathbf{q})$ is nonsingular inside the feasible neighborhood

$$Y_t = \{ \mathbf{y}_t \in \mathbb{R}^3 \mid -\infty < \alpha(\mathbf{y}_t) < 1 \} , \quad (3.56)$$

3 Surface-Based Path Following Control

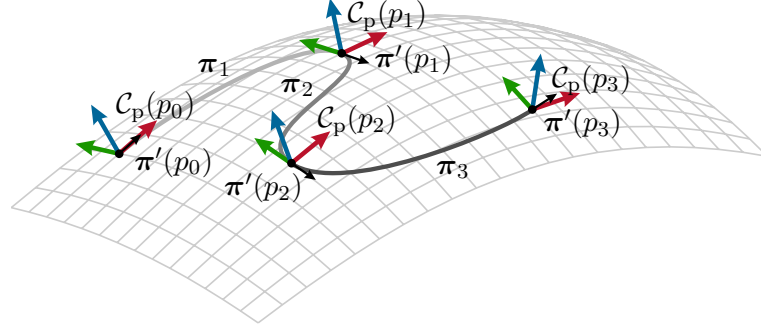


Figure 3.8: Schematic illustration of turning points. For $p \in \{p_1, p_2\}$, the path tangent vector $\pi'(p)$ lies in the normal plane $\mathcal{N}_{\mathbf{e}_1}(p)$ of the parallel contact frame $\mathcal{C}_p(p)$.

with $\alpha(\mathbf{y}_t)$ from (3.47), in which $0 < \beta(\mathbf{y}_t) < \infty$ for (3.52) and (3.55). Moreover, the set

$$P_t = \{p \in I \mid \pi'(p) \perp \pi_p(p)\} \quad (3.57)$$

designates the so-called *turning points* of a path $\pi(p)$ at which the path has in-plane turns, i. e. where the path tangent $\pi'(p)$ lies in the normal plane $\mathcal{N}_{\mathbf{e}_1}(p)$ of the parallel contact frame $\mathcal{C}_p(p)$, cf. Fig. 3.8. In order to further investigate the turning points P_t , inserting (3.46) and (3.47) into (3.45) yields

$$\dot{p}^* = \frac{1}{\mathbf{e}_1^T(p^*)\pi'(p^*) - (\mathbf{y}_t - \pi(p^*))^T \mathbf{e}'_1(p^*)} \mathbf{e}_1^T(p^*) \mathbf{J}_t(\mathbf{q}) \dot{\mathbf{q}}. \quad (3.58)$$

In (3.58), the term $(\mathbf{y}_t - \pi(p^*))^T \mathbf{e}'_1(p^*)$ becomes zero at planar surface areas of the underlying freeform 3D surface $\sigma(\mathbf{s}(p))$, i. e. $\mathbf{e}'_1(p^*) = \mathbf{0}$, or if the output \mathbf{y}_t is on the path $\pi(p^*)$, i. e. $\mathbf{y}_t - \pi(p^*) = \mathbf{0}$. Additionally, at turning points $\mathbf{e}_1^T(p^*)\pi'(p^*) = 0$ and therefore the path velocity $\dot{p}^* \rightarrow \infty$ due to (3.58). Since \dot{p}^* is used in (3.49) and (3.51), the corresponding rows of the transformation matrix $\mathbf{L}(\mathbf{q})$ grow to infinity at turning points and the coordinate transformation (3.55) becomes undefined. Note that in the proximity of turning points, the transformation matrix $\mathbf{L}(\mathbf{q})$ remains nonsingular, but becomes ill-conditioned. Therefore, such paths have to be split into multiple parts to exclude the turning points P_t . For example, the path $\pi(p)$ illustrated in Fig. 3.8 exhibits two turning points at $p \in \{p_1, p_2\}$ according to (3.57). In order to exclude the turning points, this path is split into

$$\begin{aligned} \pi_1(p) &= \{\pi(p) \mid p \in [p_0, p_1]\} \\ \pi_2(p) &= \{\pi(p) \mid p \in (p_1, p_2)\} \\ \pi_3(p) &= \{\pi(p) \mid p \in (p_2, p_3]\}. \end{aligned}$$

In a practical implementation, the turning points P_t can be approached very closely, such that switching to the next part of the path is possible.

Inside the feasible neighborhood Y_t , the coordinate transformation for the surface-based path (3.55) can be shown to be a \mathcal{C}^1 -diffeomorphism for a fully actuated 6-DoF robot.

3.4 Feedback Linearization

In this section, a static state feedback is introduced in order to linearize the quasi-static model (2.24) from Section 2.3 “Singular Perturbation Theory”. To simplify the notation, this model is stated again in the form

$$\mathbf{M}(\mathbf{q})\ddot{\mathbf{q}} + \mathbf{n}(\mathbf{q}, \dot{\mathbf{q}}) = \mathbf{u} + \boldsymbol{\tau}_e, \quad (3.59)$$

with the system torque input $\mathbf{u}^T = [u_1 \dots u_7]$. The following concepts and equations are independent of the underlying contact frame. Hence, either the natural contact frame \mathcal{C}_n from Section 3.3.1 “Natural Contact Frame” or the parallel contact frame \mathcal{C}_p from Section 3.3.2 “Parallel Contact Frame” can be chosen for the specific application at hand. Thus, the appropriate Jacobian $\hat{\mathbf{J}}(\mathbf{q})$ is used either from (3.40) or (3.55), as the application requires, and the contact frame is denoted generically by \mathcal{C} .

The system input \mathbf{u} in (3.59) is composed of

$$\mathbf{u} = \boldsymbol{\tau}_c + \boldsymbol{\tau}_n, \quad (3.60)$$

where $\boldsymbol{\tau}_c$ denotes the controller input and $\boldsymbol{\tau}_n$ is the nullspace input. The latter is detailed in Section 3.6 “Hierarchical Nullspace Controller”. The controller input $\boldsymbol{\tau}_c$ is given by the static state feedback

$$\boldsymbol{\tau}_c = \mathbf{M}(\mathbf{q})\hat{\mathbf{J}}^\dagger(\mathbf{q})\left(\mathbf{v} - \dot{\hat{\mathbf{J}}}(\mathbf{q}, \dot{\mathbf{q}})\dot{\mathbf{q}}\right) + \mathbf{n}(\mathbf{q}, \dot{\mathbf{q}}) - \boldsymbol{\tau}_e \quad (3.61)$$

with the new system input $\mathbf{v}^T = [\mathbf{v}_t^T \ \mathbf{v}_r^T] = [v_1 \dots v_6]$, which transforms the system (3.59) into a system with linear input-output behavior in the new coordinates

$$\ddot{\hat{\mathbf{y}}} = \mathbf{v}. \quad (3.62)$$

Thus, the feedback transformation (3.61) transforms the nonlinear system dynamics (3.59) with respect to a nonlinear surface-based ribbon $(\boldsymbol{\pi}(p), \boldsymbol{\sigma}_n(\mathbf{s}(p)))$ on a freeform 3D surface $\boldsymbol{\sigma}(\mathbf{s}(p))$ into a linear system in form of six integrator chains of length two in the new coordinates $\hat{\mathbf{y}}$. Note that the right pseudoinverse of the Jacobian $\hat{\mathbf{J}}^\dagger(\mathbf{q}) = \hat{\mathbf{J}}^T(\mathbf{q})(\hat{\mathbf{J}}(\mathbf{q})\hat{\mathbf{J}}^T(\mathbf{q}))^{-1}$ was used in (3.61) due to the kinematic redundancy of the robot.

3.5 Task Space Controller

The linear system (3.62) in the new coordinates $\hat{\mathbf{y}}$, which results from the feedback transformation (3.61), serves as a basis for the design of standard linear controllers, in particular an impedance controller, an admittance controller and a force controller, which are introduced in this section. Note that as a result of the projection operator and the transformation into the path coordinates, these controllers act with respect to the contact frame. At each instance of time, the distance of the system output \mathbf{y}_t normal to the surface, tangential and transversal to the path are taken into account by the surface-based path following control concept. Thus, the control errors for position and orientation are formulated with respect to the contact frame \mathcal{C} and also the virtual control inputs \mathbf{v} act in this frame.

3.5.1 Impedance Control

Impedance control imposes a mechanical reference model, i. e. the relation between position and force, on the underlying linear system, which is realized using the control law

$$\mathbf{v} = \ddot{\hat{\mathbf{y}}^d} + (\mathbf{M}^d)^{-1} (\hat{\mathbf{f}}_e - \mathbf{D}^d(\dot{\hat{\mathbf{y}}} - \dot{\hat{\mathbf{y}}^d}) - \mathbf{K}^d(\hat{\mathbf{y}} - \hat{\mathbf{y}}^d)) , \quad (3.63)$$

with the projected external generalized forces

$$\hat{\mathbf{f}}_e = (\hat{\mathbf{J}}^\dagger(\mathbf{q}))^T \boldsymbol{\tau}_e . \quad (3.64)$$

Equation (3.63) uses the desired trajectory $(\hat{\mathbf{y}}^d, \dot{\hat{\mathbf{y}}^d}, \ddot{\hat{\mathbf{y}}^d})$ comprising the desired position, velocity and acceleration given in the coordinates of the contact frame $\hat{\mathbf{y}}$. The desired mass matrix is denoted by \mathbf{M}^d , \mathbf{D}^d is the desired damping matrix and \mathbf{K}^d the desired stiffness matrix. Using (3.63) for the linear system (3.62) yields

$$\mathbf{M}^d \ddot{\hat{\mathbf{e}}} + \mathbf{D}^d \dot{\hat{\mathbf{e}}} + \mathbf{K}^d \hat{\mathbf{e}} = \hat{\mathbf{f}}_e \quad (3.65)$$

as closed-loop error system with the control error $\hat{\mathbf{e}} = \hat{\mathbf{y}} - \hat{\mathbf{y}}^d$ in the new coordinates. For $\hat{\mathbf{f}}_e = \mathbf{0}$, the equilibrium point $\hat{\mathbf{e}} = \mathbf{0}$, $\dot{\hat{\mathbf{e}}} = \mathbf{0}$ is exponentially stable for positive definite matrices \mathbf{M}^d , \mathbf{D}^d and \mathbf{K}^d [71].

Decoupled Error Dynamics

The error dynamics (3.65) decompose into six decoupled ordinary differential equations of order two by using diagonal controller gain matrices \mathbf{M}^d , \mathbf{D}^d and \mathbf{K}^d in the form

$$\mathbf{M}^d = \text{diag}(m_1^d, \dots, m_6^d) \quad (3.66a)$$

$$\mathbf{D}^d = \text{diag}(d_1^d, \dots, d_6^d) \quad (3.66b)$$

$$\mathbf{K}^d = \text{diag}(k_1^d, \dots, k_6^d) . \quad (3.66c)$$

The error dynamics (3.65) with (3.66) are exponentially stable if $m_i^d > 0$, $d_i^d > 0$ and $k_i^d > 0$ for $i = 1, \dots, 6$.

Compliance Control

For the implementation of the impedance control law (3.63), the measurement of the external generalized forces in $\boldsymbol{\tau}_e$ (3.64) is required. If this measurement is not available, $\boldsymbol{\tau}_e$ cannot be fed back in (3.61) and the feedback linearization is not valid if external forces act on the system. In this case, the control law (3.63) is reduced to a compliance control law in the form

$$\mathbf{v} = \ddot{\hat{\mathbf{y}}^d} + (\mathbf{M}^d)^{-1} (-\mathbf{D}^d(\dot{\hat{\mathbf{y}}} - \dot{\hat{\mathbf{y}}^d}) - \mathbf{K}^d(\hat{\mathbf{y}} - \hat{\mathbf{y}}^d)) , \quad (3.67)$$

where the feedback of $\hat{\mathbf{f}}_e$ is omitted. Essentially, the control law (3.67) represents a PD control law formulated in the path coordinates. Imposing the desired mass matrix \mathbf{M}^d is not possible in this case.

Path-Dependent Controller Parameters

In path following control, the current position on the path $p^*(t)$ is calculated at every instance of time by a projection operator, as introduced in Section 3.3 “Surface-Based Frames and Coordinate Transformations”. Thus, the path position $p^*(t)$ is known and the parameters of the mechanical reference model can be adapted by the path position in the form of $\mathbf{M}^d(p(t))$, $\mathbf{D}^d(p(t))$ and $\mathbf{K}^d(p(t))$ [72]. Using this property, the behavior of the robot along the path, normal to the surface and transversal to the path can be adjusted locally. For example, in a draping or polishing process, the stiffness k_3 for coordinate axis ξ_3 along the surface normal can be adjusted along the path to provide the appropriate surface normal forces at each point on the path. Due to the time dependence in the reference model parameters, the error dynamics of the system (3.65) become time variant and are stable under the following conditions [72].

Lemma 1. *Let*

$$\mathbf{M}^d(p(t))\ddot{\hat{\mathbf{e}}} + \mathbf{D}^d(p(t))\dot{\hat{\mathbf{e}}} + \mathbf{K}^d(p(t))\hat{\mathbf{e}} = \mathbf{0} \quad (3.68)$$

be the error dynamics of the closed-loop system with the path-dependent diagonal gain matrices $\mathbf{M}^d(p) = \text{diag}(m_1^d(p), \dots, m_6^d(p))$, $\mathbf{D}^d(p) = \text{diag}(d_1^d(p), \dots, d_6^d(p))$ and $\mathbf{K}^d(p) = \text{diag}(k_1^d(p), \dots, k_6^d(p))$. Under the assumption of positive and finite impedance parameters

$$M_1 < m_i^d(p) < M_2 \quad (3.69a)$$

$$M_3 < d_i^d(p) < M_4 \quad (3.69b)$$

$$M_5 < k_i^d(p) < M_6, \quad (3.69c)$$

and if the conditions

$$|\dot{p}(t)| < M_7 \quad (3.70a)$$

$$\left| \frac{\partial}{\partial p} \left(\frac{k_i^d(p)}{m_i^d(p)} \right) \right| < M_8 < 2 \frac{M_3 M_5}{M_2^2 M_7} \quad (3.70b)$$

hold for all path parameters $p(t)$, $i = 1, \dots, 6$, and $0 < M_j < \infty$ ($j = 1, \dots, 8$), then the closed-loop system with the error dynamics (3.68) is uniformly exponentially stable.

Proof. Due to the diagonal matrices $\mathbf{M}^d(p(t))$, $\mathbf{D}^d(p(t))$ and $\mathbf{K}^d(p(t))$ in (3.68), the error dynamics decomposes into six decoupled, linear time-variant differential equations of the form

$$\ddot{\hat{e}}_i + \underbrace{\frac{d_i^d(p(t))}{m_i^d(p(t))}}_{f(t)} \dot{\hat{e}}_i + \underbrace{\frac{k_i^d(p(t))}{m_i^d(p(t))}}_{g(t)} \hat{e}_i = 0, \quad i = 1, \dots, 6. \quad (3.71)$$

As shown in [73], these decoupled systems are uniformly asymptotically stable under

3 Surface-Based Path Following Control

the conditions

$$|f(t)| < C_1 \quad (3.72a)$$

$$|g(t)| < C_2 \quad (3.72b)$$

$$|\dot{g}(t)| < C_3 \quad (3.72c)$$

$$0 < C_4 < g(t) \quad (3.72d)$$

$$0 < C_5 < \dot{g}(t) + 2g(t)f(t) . \quad (3.72e)$$

With the assumptions (3.69a) to (3.69c), the conditions (3.72a), (3.72b) and (3.72d) are satisfied immediately. The upper bound for condition (3.72c) is found from (3.70a) and (3.70b) in the form

$$|\dot{g}(t)| = \left| \frac{\partial}{\partial p} \left(\frac{k_i^d(p)}{m_i^d(p)} \right) \right| |\dot{p}(t)| < M_7 M_8 = C_3 . \quad (3.73)$$

With the smallest possible rate of change of $\dot{g}(t)$, that is $-M_7 M_8$, the right-hand side of (3.72e) is bounded from below with

$$\dot{g}(t) + 2g(t)f(t) > \underbrace{-M_7 M_8 + 2 \frac{M_3 M_5}{M_2^2}}_{C_5} > 0 , \quad (3.74)$$

from which the right inequality of (3.70b) results. This proves the uniform asymptotic stability. Finally, uniform exponential stability of (3.68) follows from the uniform asymptotic stability with [71, Theorem 6.13]. \square

3.5.2 Admittance Control

In admittance control, the mass-spring-damper reference model, parametrized by the matrices \mathbf{M}^d , \mathbf{D}^d and \mathbf{K}^d , generates a reference trajectory $(\hat{\mathbf{y}}^p, \dot{\hat{\mathbf{y}}}^p, \ddot{\hat{\mathbf{y}}}^p)$ comprising the reference position, velocity and acceleration, reading as

$$\ddot{\hat{\mathbf{y}}}^p = \ddot{\hat{\mathbf{y}}}^d + (\mathbf{M}^d)^{-1} (\hat{\mathbf{f}}_e - \mathbf{D}^d(\dot{\hat{\mathbf{y}}}^p - \dot{\hat{\mathbf{y}}}^d) - \mathbf{K}^d(\hat{\mathbf{y}}^p - \hat{\mathbf{y}}^d)) \quad (3.75a)$$

$$\dot{\hat{\mathbf{y}}}^p = \int_0^t \ddot{\hat{\mathbf{y}}}^p d\tau \quad (3.75b)$$

$$\hat{\mathbf{y}}^p = \int_0^t \dot{\hat{\mathbf{y}}}^p d\tau . \quad (3.75c)$$

The reference model in (3.75a) incorporates the feedback of the external forces $\hat{\mathbf{f}}_e$ [74]. The error system for this reference model with the reference position error $\hat{\mathbf{e}}^p = \hat{\mathbf{y}}^p - \hat{\mathbf{y}}^d$ is given by

$$\mathbf{M}^d \ddot{\hat{\mathbf{e}}}^p + \mathbf{D}^d \dot{\hat{\mathbf{e}}}^p + \mathbf{K}^d \hat{\mathbf{e}}^p = \hat{\mathbf{f}}_e , \quad (3.76)$$

and matches the error dynamics of the impedance control (3.65). The reference trajectory generated by (3.75) is fed to a subordinate position controller with the positive definite gain matrices \mathbf{K}_0 and \mathbf{K}_1 in the form

$$\mathbf{v} = \ddot{\hat{\mathbf{y}}}^p - \mathbf{K}_1(\dot{\hat{\mathbf{y}}} - \dot{\hat{\mathbf{y}}}^p) - \mathbf{K}_0(\hat{\mathbf{y}} - \hat{\mathbf{y}}^p) . \quad (3.77)$$

3.5.3 Force Control

The control law

$$\mathbf{v} = \ddot{\mathbf{y}}^d + (\mathbf{M}^d)^{-1} \left(\hat{\mathbf{f}}_e - \hat{\mathbf{f}}_e^d - \mathbf{D}_f^d (\dot{\hat{\mathbf{f}}}_e - \dot{\hat{\mathbf{f}}}_e^d) \right) \quad (3.78)$$

implements the force controller with the desired mass matrix \mathbf{M}^d and the damping matrix \mathbf{D}_f^d . By introducing the force error $\hat{\mathbf{e}}_f = \hat{\mathbf{f}}_e - \hat{\mathbf{f}}_e^d$, the error dynamics for the linear system (3.62) with (3.78) become

$$\mathbf{M}^d \ddot{\hat{\mathbf{e}}}_f = \hat{\mathbf{e}}_f + \mathbf{D}_f^d \dot{\hat{\mathbf{e}}}_f. \quad (3.79)$$

At this point it should be emphasized that the desired forces $\hat{\mathbf{f}}_e^d$, the interaction forces $\hat{\mathbf{f}}_e$ and the force error $\hat{\mathbf{e}}_f$ are given with respect to the contact frame \mathcal{C} due to the chosen coordinate transformation and the feedback linearization, see Section 3.4 “Feedback Linearization”. Thus, at every point along the path, the surface normal vector and the tangential and transversal directions are known and the interaction forces are formulated with respect to these directions. This property is beneficial for many industrial processes on freeform 3D surfaces, e. g. polishing and draping, where the interaction forces with respect to the freeform 3D surface are critical.

3.5.4 Hybrid Control Concepts

The feedback transformation from Section 3.4 “Feedback Linearization” yields a linear system (3.62), which comprises six independent integrator chains of length two. Based on the decoupling in the new coordinates and the new system input \mathbf{v} , hybrid control concepts can be designed as a composition of the standard control laws introduced in the previous subsections.

As an example, a polishing process for freeform 3D surfaces and the development of a hybrid control concept is described in the following. For a known target 3D object, the surface-based paths are planned using an offline programming method [2]. In order to allow the robot to adjust for uncertainties and deviations from the target 3D object, an online controller is required, which is aware of the underlying surface. Thus, surface-based path following control with a hybrid control concept for the six independent virtual inputs v_i , $i = 1, \dots, 6$, of (3.62) is implemented in the form

$$\mathbf{v} = \begin{bmatrix} v_1 \\ v_2 \\ v_3 \\ v_4 \\ v_5 \\ v_6 \end{bmatrix} = \begin{bmatrix} \ddot{\hat{y}}_1^d - k_1(\hat{y}_1 - \hat{y}_1^d) - d_1(\dot{\hat{y}}_1 - \dot{\hat{y}}_1^d) \\ \ddot{\hat{y}}_2^d - k_2(\hat{y}_2 - \hat{y}_2^d) - d_2(\dot{\hat{y}}_2 - \dot{\hat{y}}_2^d) \\ \ddot{\hat{y}}_3^d + \frac{1}{m_3^d} \left(\hat{f}_{e,3} - \hat{f}_{e,3}^d - d_3^d (\dot{\hat{f}}_{e,3} - \dot{\hat{f}}_{e,3}^d) \right) \\ \ddot{\hat{y}}_4^d + \frac{1}{m_4^d} \left(\hat{f}_{e,4} - d_4^d (\dot{\hat{y}}_4 - \dot{\hat{y}}_4^d) - k_4^d (\hat{y}_4 - \hat{y}_4^d) \right) \\ \ddot{\hat{y}}_5^d + \frac{1}{m_5^d} \left(\hat{f}_{e,5} - d_5^d (\dot{\hat{y}}_5 - \dot{\hat{y}}_5^d) - k_5^d (\hat{y}_5 - \hat{y}_5^d) \right) \\ \ddot{\hat{y}}_6^d + \frac{1}{m_6^d} \left(\hat{f}_{e,6} - d_6^d (\dot{\hat{y}}_6 - \dot{\hat{y}}_6^d) - k_6^d (\hat{y}_6 - \hat{y}_6^d) \right) \end{bmatrix}, \quad (3.80)$$

with suitable controller parameters as defined in the respective subsections. In (3.80), the force controller (3.78) is used in ξ_3 -direction to provide a desired force profile along the surface normal. Position controllers in the form of (3.77) along ξ_1 and ξ_2 stabilize the tool on the given path. Moreover, the impedance control law given by (3.63) is utilized for the orientation coordinates and allows the robot to compensate for deviations in the local orientation of the freeform 3D surface.

3.6 Hierarchical Nullspace Controller

The KUKA LBR iiwa 14 R820 utilized in this work is a 7-DoF robot and, thus, exhibits a one-dimensional nullspace when operating in a 3D task space. Moreover, certain tools mounted on the robot flange provide an additional kinematic redundancy for the robot motion, as already stated in Section 3.1.

In the following, the concept of single-axis tool redundancies is introduced in mathematical terms. This way, one DoF is moved from the task space to the nullspace, which increases the dimension of the latter to two. This two-dimensional nullspace is stabilized using a hierarchical nullspace controller [75] in two hierarchical levels, composed of, see (3.60),

$$\boldsymbol{\tau}_n = \boldsymbol{\tau}_{n,1} + \boldsymbol{\tau}_{n,2} . \quad (3.81)$$

The first level $\boldsymbol{\tau}_{n,1}$ influences the robot motion such that the joint limits are avoided and the redundant tool axis is stabilized, while the second hierarchical level $\boldsymbol{\tau}_{n,2}$ controls the motion of the robot elbow and stabilizes a virtual equilibrium position.

3.6.1 Single-Axis Tool Redundancy

As introduced in Section 3.1 “Overview”, a single-axis tool redundancy is a kinematic redundancy induced by the use of specific robotic tools. For example, the polishing tool illustrated in Fig. 3.2a can rotate freely around the z -axis (blue arrow), the draping roll shown in Fig. 3.2b has a redundant y -axis (green arrow), and the ultrasonic cutting tool in Fig. 3.2c exhibits a (limited) redundancy for the rotation around the x -axis (red arrow). Thus, for these tools, the task space dimension can be reduced by one and the rotation around the redundant tool axis is then stabilized in the nullspace.

The major benefit of this approach is the systematic consideration of the additional degree of freedom in the robot motion. One constraint for the tool orientation is omitted in the task space and the robot can automatically adjust the redundant axis in the nullspace. This significantly increases the overall flexibility of the robotic system. Additionally, this approach is independent of the contact frame $\mathcal{C}(p)$. Thus, either the natural contact frame $\mathcal{C}_n(p)$ or the parallel contact frame $\mathcal{C}_p(p)$ can be used for this concept. Note that this concept can also be applied to classical task space control of robotic systems [56].

In order to exploit the single-axis tool redundancy for the redundant axis $r \in \{x, y, z\}$, the appropriate minimal representation for the orientation in (2.8) has to be chosen. To this end, the TAIT-BRYAN convention (see Section 2.1.2 “Forward Kinematics”) is employed with

$$k = r \quad (3.82a)$$

$$i, j \in \{x, y, z\} \setminus r \text{ with } i \neq j . \quad (3.82b)$$

This way, the direction of the redundant tool axis r is fully determined by the angles ϕ_1 and ϕ_2 and the angle ϕ_3 denotes the rotation around the redundant tool axis. As an example, the geometric relations for $\boldsymbol{\phi}_{zyx}(\mathbf{R}_W^T)$ are illustrated in Fig. 3.9. Additionally, the transformation matrix $\mathbf{T}(\phi)$ introduced in (2.13) becomes independent

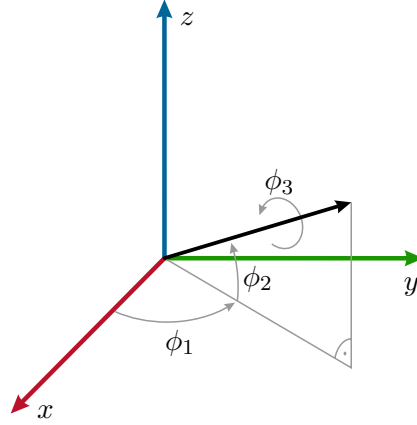


Figure 3.9: Geometric relations for the minimal representation of the orientation according to the TAIT-BRYAN convention $\phi_{zyx}(\mathbf{R}_{\mathcal{W}}^T)$.

of ϕ_3 , as can be verified by direct computation. Thus, the rotation ϕ_3 around the redundant tool axis r does not influence the angles ϕ_1 and ϕ_2 .

Using the above convention $\phi_{ijk}(\mathbf{R}_{\mathcal{W}}^T)$ for the minimal representation of the orientation, the (reduced) 5-dimensional task space $\tilde{\mathbf{y}}$ considering the single-axis tool redundancy is derived in the form

$$\tilde{\mathbf{y}} = \begin{bmatrix} \xi_1 \\ \vdots \\ \xi_5 \end{bmatrix} = \mathbf{A}\hat{\mathbf{y}} \quad (3.83)$$

$$\dot{\tilde{\mathbf{y}}} = \mathbf{A}\dot{\hat{\mathbf{y}}} = \underbrace{\mathbf{A}\hat{\mathbf{J}}(\mathbf{q})}_{\tilde{\mathbf{J}}(\mathbf{q})} \dot{\mathbf{q}}, \quad (3.84)$$

with the projection matrix

$$\mathbf{A} = \begin{bmatrix} \mathbf{I} & \mathbf{0} \\ \mathbf{0} & \begin{bmatrix} 1 & 0 & 0 \\ 0 & 1 & 0 \end{bmatrix} \end{bmatrix} \in \mathbb{R}^{5 \times 6} \quad (3.85)$$

i. e. by omitting the third orientation coordinate ξ_6 of the path-based coordinates. Note that in (3.84), the reduced Jacobian matrix $\tilde{\mathbf{J}}(\mathbf{q})$ is introduced. Analogous to Section 3.4 “Feedback Linearization”, the static state feedback, cf. (3.61),

$$\boldsymbol{\tau}_c = \mathbf{M}(\mathbf{q})\tilde{\mathbf{J}}^\dagger(\mathbf{q})(\tilde{\mathbf{v}} - \dot{\tilde{\mathbf{J}}}(\mathbf{q}, \dot{\mathbf{q}})\dot{\mathbf{q}}) + \mathbf{n}(\mathbf{q}, \dot{\mathbf{q}}) - \boldsymbol{\tau}_e, \quad (3.86)$$

with the new system input $\tilde{\mathbf{v}}^T = [\tilde{v}_1 \ \cdots \ \tilde{v}_5]$, is applied to the rigid-body system (3.59) with (3.60), which yields

$$\ddot{\tilde{\mathbf{y}}} = \tilde{\mathbf{v}}, \quad (3.87)$$

i. e. a system with linear input-output behavior in the reduced coordinates $\tilde{\mathbf{y}}$.

3.6.2 Level 1: Joint Limits and Stabilization of the Redundant Axis

The first hierarchical level of the nullspace controller operates in the nullspace of the reduced Jacobian $\tilde{\mathbf{J}}(\mathbf{q})$ of the reduced task space with the dynamically consistent

3 Surface-Based Path Following Control

nullspace projection matrix, see [75],

$$\mathbf{N}_2(\mathbf{q}) = \mathbf{M}(\mathbf{q}) \left(\mathbf{I} - \tilde{\mathbf{J}}^\dagger(\mathbf{q}) \tilde{\mathbf{J}}(\mathbf{q}) \right). \quad (3.88)$$

The lower and upper joint limits of the robot $\mathbf{q} = [q_1 \dots q_7]$ and $\bar{\mathbf{q}} = [\bar{q}_1 \dots \bar{q}_7]$, respectively, are observed using barrier functions in the joint space, reading as [76]

$$\mathbf{b}^\top(\mathbf{q}) = [b_1(q_1) \quad b_2(q_2) \quad \dots \quad b_7(q_7)] \quad (3.89)$$

$$b_i(q_i) = \frac{\bar{b}_i}{(q_i - \bar{q}_i)^2} - \frac{b_i}{(\underline{q}_i - q_i)^2}, \quad i = 1, \dots, 7, \quad (3.90)$$

where the constants b_i and \bar{b}_i , $i = 1, \dots, 7$ parametrize the slope of these functions. The barrier functions are applied to the system using

$$\boldsymbol{\tau}_{n,1} = -\mathbf{N}_2(\mathbf{q}) \mathbf{b}(\mathbf{q}). \quad (3.91)$$

The rotation around the redundant tool axis r from Section 3.6.1 “Single-Axis Tool Redundancy” can also underlie certain application-specific constraints and requirements. In the example described before related to polishing, the rotation around the z -axis is free and unconstrained, but needs to be damped to achieve a stable robot motion. On the contrary, for the draping process mentioned above, the mechanical construction of the tool brings along certain angle limits and a desired equilibrium position with respect to the rotation around the redundant axis. Thus, for the general case, the lower and upper axis limits $\underline{\xi}_6$ and $\bar{\xi}_6$, respectively, and the corresponding slope parameters b_{ξ_6} and \bar{b}_{ξ_6} are introduced for the redundant axis and the barrier function

$$b_{\xi_6}(\xi_6) = -\frac{b_{\xi_6}}{(\xi_6 - \underline{\xi}_6)^2} + \frac{\bar{b}_{\xi_6}}{(\xi_6 - \bar{\xi}_6)^2} \quad (3.92)$$

is applied to the system in the form

$$\boldsymbol{\tau}_{n,1} = \mathbf{N}_2(\mathbf{q}) \left(-\mathbf{b}(\mathbf{q}) + \hat{\mathbf{J}}^\dagger(\mathbf{q}) \begin{bmatrix} \mathbf{0} \\ -b_{\xi_6}(\xi_6) - d_6 \dot{\xi}_6 - k_6(\xi_6 - \xi_{6,0}) \end{bmatrix} \right), \quad (3.93)$$

with the damping coefficient $d_6 > 0$, the stiffness coefficient $k_6 > 0$ and the equilibrium position $\xi_{6,0}$ for the redundant tool axis r . Note that $\hat{\mathbf{J}}^\dagger(\mathbf{q})$ generates a joint space motion in the redundant tool axis r from and implements the stabilization of ξ_6 .

3.6.3 Level 2: Elbow Stabilization

For a fixed TCP frame \mathcal{T} , the redundant 7-DoF manipulator can perform a nullspace motion by rotating the elbow plane around the shoulder-wrist axis, see Fig. 2.1 and Section 2.1.4 “Inverse Kinematics”. This robot elbow motion is stabilized by the second hierarchical level, which operates in the nullspace of the first level. Using augmented projections with dynamic consistency [75], i. e. using

$$\mathbf{N}_3(\mathbf{q}) = \mathbf{M}(\mathbf{q}) \left(\mathbf{I} - \hat{\mathbf{J}}^\dagger(\mathbf{q}) \hat{\mathbf{J}}(\mathbf{q}) \right) \quad (3.94)$$

$$\boldsymbol{\tau}_{n,2} = \mathbf{N}_3(\mathbf{q}) (-\mathbf{D}_n \dot{\mathbf{q}} - \mathbf{K}_n \mathbf{q}), \quad (3.95)$$

the nullspace projection matrix $\mathbf{N}_3(\mathbf{q})$ projects the torques of the nullspace PD joint controller with the positive definite gain matrices \mathbf{K}_n and \mathbf{D}_n onto the torque input $\boldsymbol{\tau}_{n,2}$. Note that in (3.94), the Jacobian matrix $\hat{\mathbf{J}}(\mathbf{q})$ augments the reduced Jacobian matrix $\tilde{\mathbf{J}}(\mathbf{q})$, see (3.84).

3.7 Path Progress

In path following control, the robot motion is described by a path $\boldsymbol{\pi}(p)$, which defines the motion geometry in space, and the path parameter p , which specifies the temporal progress along the path. Hence, the path progress $p(t)$ is an additional degree of freedom, which can be specified according to the requirements of the given application. In the literature, many works on path following control [19, 22, 24] do not cover the path progress and use a simple timing law. In [18], an integrator chain of sufficient length is used as timing law to simplify the structure of the system equations. Moreover, a non-negative path progress is assumed in this work. The path parameter used in [77] for a nonlinear control law synchronizes the motion of multiple autonomous underwater vehicles (AUV). A collaborative scenario is presented in [78] with an application in the automotive industry in mind. The goal of this application is to mount a car door into the hinges of the car body – demonstrated using a wooden plate with hooks moved by the robot and the corresponding inertially fixed hinges. In this setting, the human motion specifies the path progress, while the robot bears the heavy load.

Collaborative robots are becoming increasingly popular in industry, and collaboration between humans and robots constitutes an important component of modern production systems. In this sense, surface-based path following control also qualifies for physical human robot interaction (pHRI), since the robot motion is restricted to a geometric path defined on the surface. For example in a polishing process, the robot can carry the weight of the polishing tool and constrain its motion to a path on the surface, while the human imposes the tangential (forward) motion. This way, the human can visually and haptically inspect the surface during the process and intuitively control the robot motion.

The following subsections focus on the temporal evolution of the path progress, with an emphasis on operation principles for pHRI applications. Four different modes of operation are presented, which summarize the results of [72]: autonomous mode, cooperative mode, cooperative mode with gesture control, collaborative mode. The different modes are based on the impedance controller (3.63), as introduced in Section 3.5.1 “Impedance Control”. Each of the operation modes generates a \mathcal{C}^2 reference trajectory $(\hat{\mathbf{y}}^d, \dot{\hat{\mathbf{y}}}^d, \ddot{\hat{\mathbf{y}}}^d)$ in the form

$$\hat{\mathbf{y}}^d = \begin{bmatrix} \xi_1^d \\ \xi_1^d \\ \mathbf{0} \end{bmatrix}, \quad (3.96)$$

i. e. the desired trajectory specifies the path progress with the trajectory $(\xi_1^d, \dot{\xi}_1^d, \ddot{\xi}_1^d)$, and – without loss of generality – prevents translational or rotational deviations from the path otherwise. Moreover, the proposed modes of operation can also be applied to classical path following control as derived in [24, 47, 72]. A video demonstrating these modes of operation is published at www.acin.tuwien.ac.at/fc09 [72].

3 Surface-Based Path Following Control

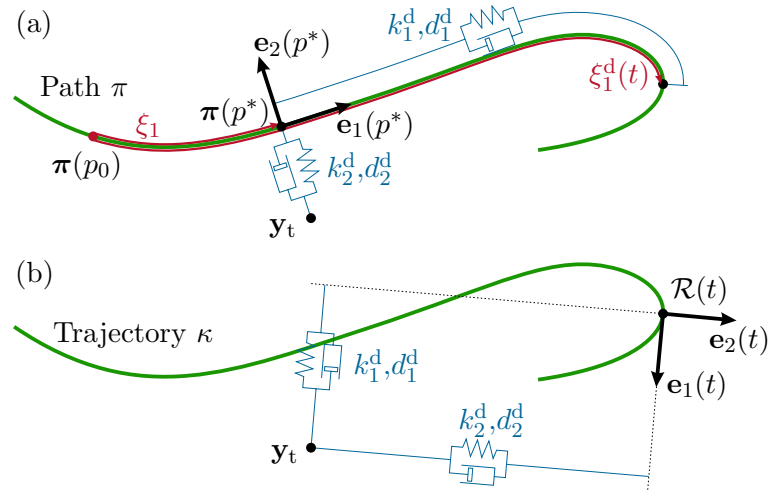


Figure 3.10: Two-dimensional schematic drawing of the coordinate systems for (a) path following control with the path progress $\xi_1^d(t)$ and (b) trajectory tracking control.

3.7.1 Autonomous Mode

If the robot motion is executed in the autonomous mode, the path progress is imposed directly as a function of time ($\xi_1^d(t)$, $\dot{\xi}_1^d(t)$, $\ddot{\xi}_1^d(t)$). Thus, the robot performs the prescribed motion along the tangential direction of the path in terms of position, velocity and acceleration.

While this robot motion is similar to classical trajectory tracking control [56], there are distinct differences in the details, as Fig. 3.10 illustrates for the two-dimensional case. In path following control (Fig. 3.10a), the projected point on the path $\pi(p^*)$ is found using a projection operator $P(\mathbf{y}_t)$ as defined in Section 3.3 “Surface-Based Frames and Coordinate Transformations”. Thus, the error dynamics are defined with respect to the projected contact frame and the transversal error dynamics act normal to the path, while the tangential error dynamics act along the path. In contrast, in trajectory tracking control (Fig. 3.10b) the control errors are defined in terms of the desired tracking coordinate frame $\mathcal{R}(t)$ at all times t and the error dynamics act along the axes of this frame. This difference becomes more significant for large control errors or large curvatures in the path $\pi(p)$ [79, 80].

3.7.2 Cooperative Mode

In cooperative mode, the robot moves at first autonomously and is independent from the human. If the human recognizes an error condition in the robot task, the robot motion can be halted using physical contact and the error condition can be remedied through manual intervention by the human.

To implement this behavior, the reference trajectory (3.96) is determined by a reference velocity v using a second-order lag element with the time constant T in the form

$$\frac{d}{dt} \begin{bmatrix} \dot{\xi}_1^d \\ \ddot{\xi}_1^d \end{bmatrix} = \begin{bmatrix} 0 & 1 \\ -\frac{1}{T^2} & -\frac{2}{T} \end{bmatrix} \begin{bmatrix} \xi_1^d \\ \dot{\xi}_1^d \end{bmatrix} + \begin{bmatrix} 0 \\ \frac{1}{T^2} \end{bmatrix} v, \quad (3.97)$$

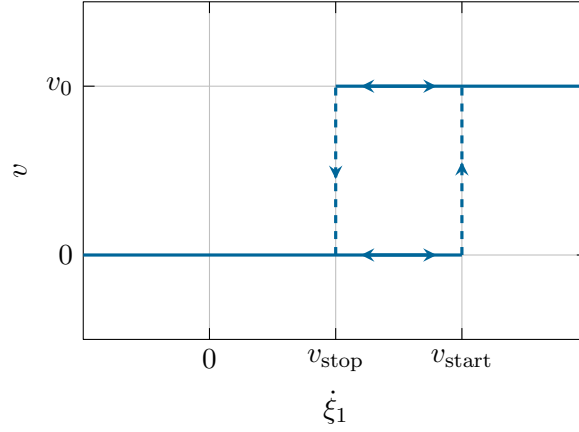


Figure 3.11: Schematic drawing of the *Relay* operator (3.99) for the reference velocity $v(t)$ for in cooperative mode with gesture control.

and the time integration of $\dot{\xi}_1^d$. The reference velocity v is chosen as

$$v = v_0 \left(1 - \frac{\xi_1^d - \xi_1}{\Delta \xi_1} \right), \quad (3.98)$$

where v_0 is the nominal velocity and the expression (3.98) reduces or increases the reference velocity as soon as the current path progress ξ_1 deviates from the reference path progress ξ_1^d . Note that the reference velocity (3.98) reaches zero at the maximum deviation $\Delta \xi_1$. The stiffness of the tangential subsystem k_1^d of the impedance controller (3.63) is chosen such that the human can easily provoke the necessary deviation using small forces at the TCP of the robot. An external motion control ensures that the path progress is stopped at the end of the path.

3.7.3 Cooperative Mode: Gesture Control

Simple gesture control can be added to the cooperative mode using the tangential velocity $\dot{\xi}_1$ and the lag element (3.97). To this end, the reference velocity $v(t)$ is implemented as hysteresis function in form of a so-called *Relay* operator [81] given by

$$v(t) = \begin{cases} 0 & \text{if } \dot{\xi}_1(t) \leq v_{\text{stop}} \\ v_0 & \text{if } \dot{\xi}_1(t) \geq v_{\text{start}} \\ 0 & \text{if } \dot{\xi}_1(\tau) \in (v_{\text{stop}}, v_{\text{start}}) \forall \tau \in [t_0, t] \\ v\left(\arg \max_{\tau \in [t_0, t]} \dot{\xi}_1(\tau) \notin (v_{\text{stop}}, v_{\text{start}})\right) & \text{otherwise,} \end{cases} \quad (3.99)$$

with $0 < v_{\text{stop}} < v_{\text{start}} < v_0$, see Fig. 3.11. The tangential error dynamics are parametrized to ensure a compliant behavior with k_1^d and d_1^d , while the transversal coordinates use high stiffness to stabilize the TCP on the path. Thus, the end-effector is compliant along the path and an autonomous motion can be initiated by pushing the robot end-effector or tool in tangential direction with $\dot{\xi}_1 > v_{\text{start}}$. The robot motion is stopped again once the instantaneous tangential velocity falls below the stopping threshold velocity v_{stop} , i. e. $\dot{\xi}_1 < v_{\text{stop}}$, by halting the robot manually at its end-effector.

3 Surface-Based Path Following Control

3.7.4 Collaborative Mode

The collaborative mode follows directly from the concept of path following control by setting the tangential stiffness to zero, i. e. $k_1^d = 0$. Hence, the tangential coordinate ξ_1 in (3.65) is no longer influenced by ξ_1^d and the robot end-effector or tool can be moved along the path freely by the human. Still, the TCP is stabilized onto the path by the transversal subsystem ξ_2, ξ_3 and the orientation ξ_r follows the orientation of the contact frame $\mathcal{C}(p^*)$ using the orientation subsystem.

4

Concept Study on Tape Application

An important task in the handling of deformable materials is the application of pre-cut deformable tapes to given 3D objects, as introduced in Section 1.2 “[Handling of Deformable Materials](#)”. In the textile and apparel industry, for example, functional and decorative elements are placed onto garments, shoes and other consumer goods [31]. Decorative labels and functional adhesive tapes, e.g. gaskets and protective foils, are applied to car parts and components in the automotive industry. In the FRP sector, layering and draping of multiple sheets of pre-cut technical textiles onto a mold is required for the production of FRP components [30].

While many scientific works [36, 82] and also commercially available solutions are focused on the application of continuous tapes [9], these solutions do not generalize to pre-cut tapes. Björnsson et al. [36] state that there is a need for alternative approaches to ATL and AFP for small and complex shapes, which provide more flexibility with respect to the shape of the target 3D object and the deformable component.

The aim of the concept study conducted in this chapter is to systematically develop such a concept for the application of pre-cut tapes in an industrial setting, as introduced above. A special focus is laid on the application of strip-like textiles on small- and medium-sized target 3D objects which fit into the work space of a robot cell, covering many of the above use cases in the textile and garment industry as well as the FRP composites part production.

In a first step, the complete tape application process chain is presented and analyzed. Successively, ten different concepts are proposed and discussed with references to the literature and commercial solutions. Afterwards, these concepts are evaluated with respect to accuracy, flexibility, speed, complexity and risk of design as well as the ability to impose tension and consolidation forces on the applied tape. In the final section of this chapter, the most suitable concept is then selected and its limitations and possible remedies are discussed.

4 Concept Study on Tape Application

A patent application for the results of this concept study was filed [83]. As an example use-case for the surface-based path following control concept, the selected concept for the tape application is then implemented in Chapter 5 “Application of Curved Tapes on 3D Objects” to demonstrate the feasibility of the proposed control approach.

4.1 Process Analysis

In this section, the handling, placing and draping process of deformable materials onto 3D objects is analyzed. First, the problem to be solved is stated concisely, followed by a detailed description of the process steps and general statements on the robot employment and kinematics.

4.1.1 Problem Statement

Task The task to be solved is the combined contouring and application of deformable materials to freeform 3D surfaces.

Requirements The process requires high flexibility with respect to the shape of the deformable material and the target 3D object. Further process requirements are high accuracy for the deformable material to be placed on the freeform 3D surface and the possibility to wrap a textile up to 180° around the target 3D object. Simultaneously, the consolidation forces (normal to the surface) and the tension forces have to be controlled.

Scope The scope of this problem is the processing of strip-like pre-cut tapes on small- to medium-sized target 3D objects.

Workflow The required robot motions are calculated in an offline-programming approach [2] and executed using closed-loop control strategies.

4.1.2 Process Steps

An overview of the individual process steps and different possibilities to arrange these steps are depicted in Fig. 4.1. The complete process, shown in Fig. 4.1a, incorporates a pre-heating and a consolidation step. Some deformable materials, e. g., thermoplastic polyurethane (TPU) [84] and prepregs [9], require a pre-heating step to activate the adhesive properties of the material prior to transferring the deformable component to the freeform 3D surface. A consolidation step is also required for some materials to unify the applied material with the workpiece [9, 84]. The main focus of this concept study are the contouring and application process steps, see Fig. 4.1b, while the pre-heating and consolidation steps are not considered in this work. Additionally, the contouring and application steps can also be arranged in reverse order, see Fig. 4.1c. In this case, the raw material is applied first to the target 3D object and is then contoured in place. If the application step is implemented using an additive process, like 3D printing [85] or building the contour of the deformable material from smaller entities [48, 86, 87], the contouring step can be omitted.

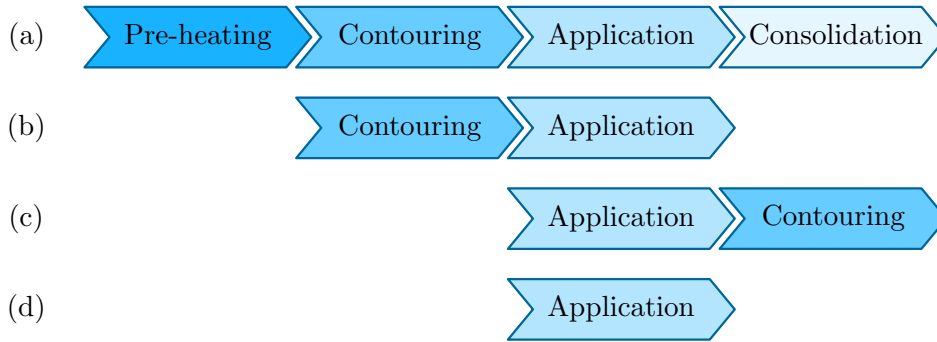


Figure 4.1: Process steps for the contouring and application of deformable materials. (a) Complete process chain, (b) Process steps considered in this concept study, (c) Alternate order of the process steps, (d) Reduced process chain for concepts related to additive processes.

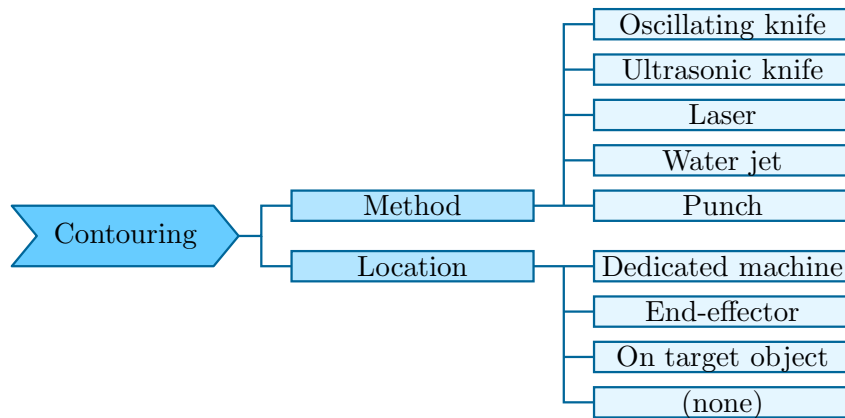


Figure 4.2: Classes and categories of the process step *contouring*.

In the following subsections, the two process steps *contouring* and *application* are considered in more detail.

Contouring

The process step *contouring* is classified with respect to the *method*, i.e. which physical principle is used to perform the contouring operation, and *location*, i.e. the place where the contouring step is performed, see Fig. 4.2.

The contouring method is mainly determined by the properties of the deformable material and the desired properties of the cutting line. Technical textiles in the FRP sector are mainly cut using oscillating and ultrasonic knives and water jet cutters [88, 89]. In the textile and apparel industry, deformable materials are predominantly contoured using oscillating or rolling knives and punching machines. Laser cutting is a contact-free contouring method, which is only applicable to some materials [88], since it can leave burn marks at the cutting line.

The second class considers the *location* where the contouring process step takes place. The different categories are described in the following:

Dedicated machine In this category, a dedicated, stationary machine is used to perform the contouring process. Widely used are cutting tables in the FRP

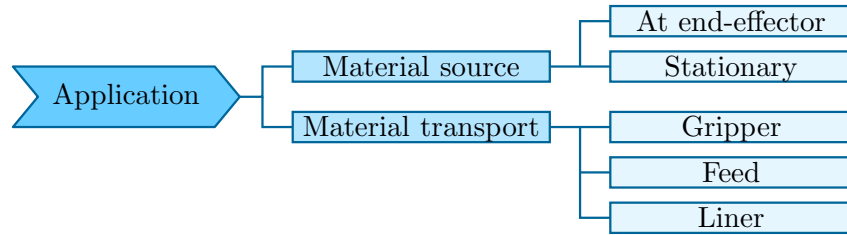


Figure 4.3: Classes and categories of the process step *application*.

sector or in the textile industry [88].

End-effector The cutting mechanism is integrated into the application tool [9, 90, 91], which mostly allows to cut only simple contours. At the same time, this integration increases the complexity, size and weight of the application tool, which in turn increases the payload requirements for the robot and reduces the dexterity and flexibility for the application process [36].

On target object Contouring can also be performed directly on the target object after transferring the raw deformable material to the surface of the target object. However, this raises three additional problems: Firstly, prior to contouring, the deformable material has a larger and more areal extent which is challenging to apply to doubly-curved surfaces without wrinkles. In particular, if the material is not tensile, wrinkles inevitably occur on doubly-curved surfaces. Secondly, contouring the thin layer of deformable material reliably while strictly preserving the integrity of the underlying target 3D object is a challenging task. This significantly restricts the admissible contouring mechanisms and deformable materials. Thirdly, after contouring, the excess material has to be removed from the target 3D object, which requires additional tools and mechanisms. Due to these three issues, it is advantageous to perform contouring prior to the application process step. Thus, this category is not further investigated in the concept study.

(none) The contouring process step can be omitted when additive materials and processes are used during the application step. Additive materials can be applied either as discrete patches [30, 48, 86, 87] or as a continuous stream, e. g., 3D printing [85].

Application

The *application* process step is classified with respect to the *location of the material source* and the *material transport*, as illustrated in Fig. 4.3.

The location of the material source is subdivided into the categories *at end-effector*, where the pre-cut deformable components are stored at the end-effector in form of rolls or stacks [9], and *stationary*, where the deformable components are supplied from a stationary unit [30, 42–46, 91].

The material transport is classified into the following categories, see Fig. 4.3.

Gripper Most works in the literature use grippers with different physical gripping principles to perform the material transport. Mechatronic, shape-adaptive

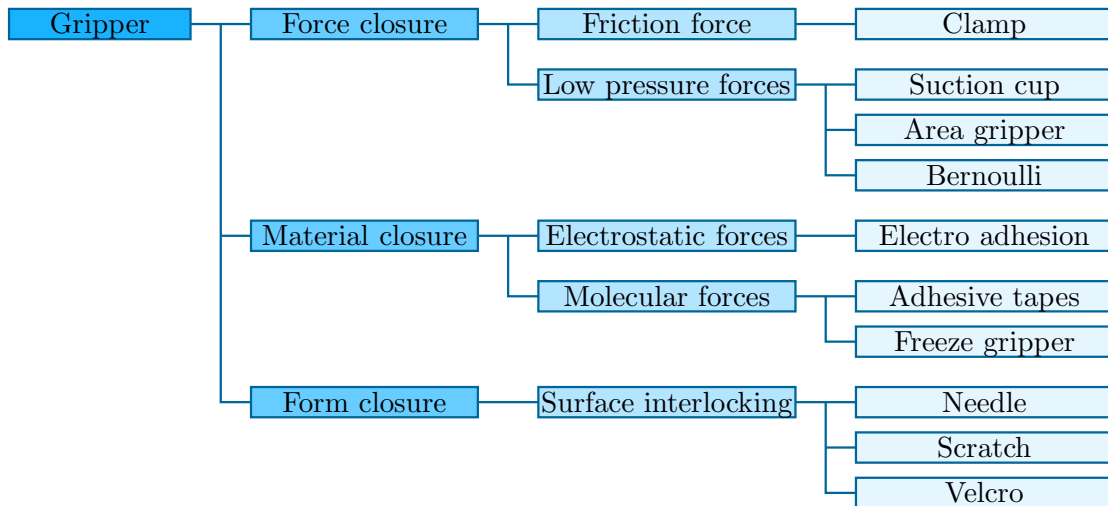


Figure 4.4: Overview of physical gripping principles [92].

gripper solutions [42, 44, 45], low-pressure area grippers [43] as well as standard grippers [47] were proposed in the literature to grasp and transport deformable materials. For consumer goods and technical textiles, gripping principles which do not introduce foreign substances or impair the deformable material are to be preferred [92], cf. Fig. 4.4. Hence, suitable grippers are clamps, suction cups, low-pressure area grippers, BERNOULLI grippers and electro adhesion grippers.

Feed Using feeding mechanisms, grasping of the deformable material is circumvented. Systems like ATL and AFP [9] directly feed the raw material and apply it to the freeform 3D surface using a draping roll.

Liner A so-called liner is a carrier foil on which adhesive deformable material is transported [50, 93, 94]. Similar to a feeding mechanism, grasping of the deformable material is not required. Additionally, the full object state of the deformable component is controlled since it is precisely held in place by the liner and the mechanical feeding mechanism throughout the feeding and application process. The pre-cut components can be separated efficiently from the residual material if the cutting contours of the components are simply connected shapes [50].

4.1.3 Robot Employment and Kinematics

Essentially, the handling process is further classified in terms of the robot employment, i. e. the number of robots utilized in the overall process, and the robot kinematics, i. e. the relation between the moving and the stationary system components.

Different categories for the number of robots utilized in a solution are illustrated in Fig. 4.5. In this context, a mechatronic solution (see Fig. 4.5a) is considered as a custom-built machine to transfer deformable components to 2D or 3D objects at fixed positions using tailored mechanisms [42, 44, 45, 95]. Such approaches do not provide the necessary flexibility with respect to the target 3D object and are not further investigated in this concept study. Figure 4.5b illustrates low-pressure area

4 Concept Study on Tape Application

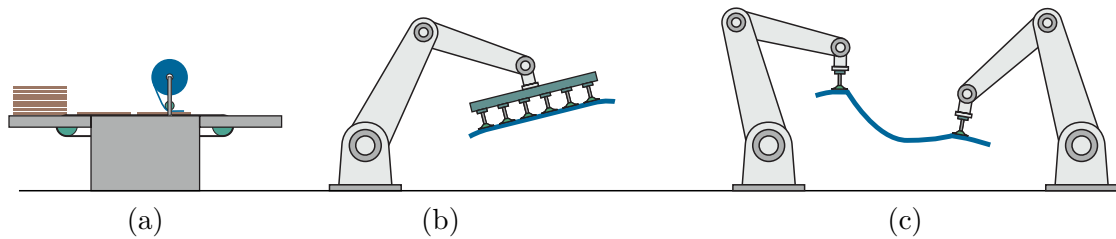


Figure 4.5: General considerations for the robot employment. (a) Mechatronic solution, (b) Single-robot solution with area- or multi-gripper, (c) Collaborative manipulation with a multi-robot solution.

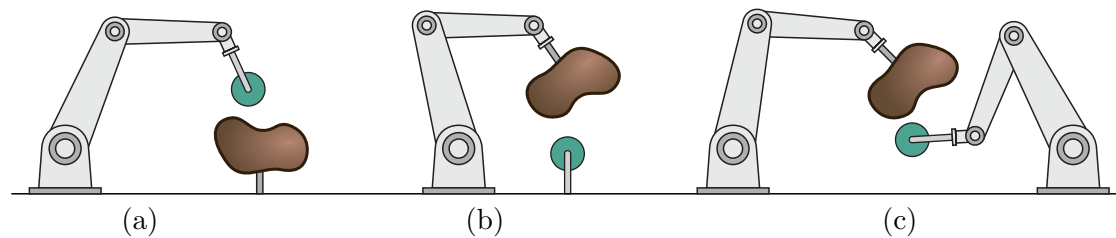


Figure 4.6: General considerations for the robot kinematics. (a) Stationary target 3D object and moving tool, (b) Stationary tool and moving target 3D object, (c) Moving tool and target 3D object.

grippers [43, 96] and multi-point grippers [54, 95, 97]. Such gripping tools are very complex and require often a high-payload robot for manipulation and, consequently, the flexibility with respect to the target 3D object shape is also quite limited. In the literature, most works investigate single-robot solutions to manipulate deformable materials. In contrast, employing multiple robots requires more complex collaborative coordination of the individual robots [46, 47, 98], but allows to use standard gripper components and provides a larger degree of flexibility.

Figure 4.6 illustrates three different options for the relative motion between the robot tool and the target 3D object. First, in Fig. 4.6a, the target 3D object is stationary while the tool is moving. This case is most common in the literature and also in commercial solutions [9, 86]. However, the tools to grasp and manipulate the deformable materials [43, 96] or to apply and consolidate these materials to the target 3D object [9] are large and require high-payload robots. Additionally, the range of motion is limited due to the size of the tool. Second, Fig. 4.6b depicts the kinematically reversed situation where the tool is stationary and the target 3D object is moving. Such an arrangement is especially suitable if the target 3D object is passive, i. e. without functional components like heating, venting or cooling systems, and if the target 3D object is suitably sized [99]. Note that reversing the relative motion between the robot tool and the target 3D object, i. e. changing from Fig. 4.6a to Fig. 4.6b, is possible for most solutions, but not always advantageous. Third, the flexibility of a robotic solution improves significantly if the number of DoF is increased, i. e. by using additional prismatic or rotational external axes or an additional robot, which is illustrated in Fig. 4.6c. Existing solutions in the literature use an additional rotating axis [53, 100], while the commercial solution SAMBA PRO [48] uses a 6-DoF industrial robot to position and orient the target 3D object and a 3-DoF delta robot to handle and place the deformable components.

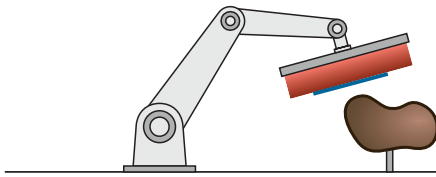


Figure 4.7: Shape-adaptive gripper.

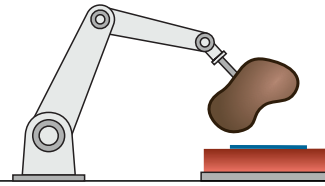


Figure 4.8: Shape-adaptive table.

4.2 Concepts

Based on the fundamental considerations and categories of the previous sections, ten distinct concepts are presented in the following. Each concept is first categorized with respect to the *robot employment* and the *robot kinematics*, described in Section 4.1.3 “Robot Employment and Kinematics”, as well as the *contouring location*, *material source* and *material transport*, introduced in Section 4.1.2 “Process Steps”. Successively, the basic functional principle of the respective concept is detailed and references to the literature and to commercial solutions are given. The qualitative evaluation of the proposed concepts is performed in the next section.

4.2.1 Shape-Adaptive Gripper

Robot employment	Robot kinematics	Contouring location	Material source	Material transport
Single robot	Moving tool	Dedicated machine	Stationary	Gripper

The first concept, schematically depicted in Fig. 4.7, utilizes a single robot with a *shape-adaptive gripper* to transfer the pre-cut deformable components from a dedicated contouring machine to the freeform 3D surface. The shape-adaptive gripper is a low-pressure area gripper, which has a compliant foam surface to adapt to the target 3D object.

Low-pressure area grippers are widely used in the literature, like granulate-filled form-adaptive grippers [43, 101], a selective area gripper prototyped in [44] and a cylindrical area gripper with integrated heaters [96]. Additionally, shape-adaptive grippers are often constructed as multi-point grippers with passive mechanical or mechatronic adaptation mechanisms [54, 95, 102]. The delta robot in the commercial solution SAMBA PRO [48] uses a shape-adaptive gripper with a significant compliant layer for the application step.

4.2.2 Shape-Adaptive Table

Robot employment	Robot kinematics	Contouring location	Material source	Material transport
Single robot	Moving 3D object	Dedicated machine	Stationary	Conveyor belt

The concept *shape-adaptive table* is kinematically reversed in comparison to the previous concept, see Section 4.1.3 “Robot Employment and Kinematics”. The schematic drawing in Fig. 4.8 illustrates this single-robot solution, in which the deformable material is pre-cut and prepared on a compliant table. The moving 3D object is then pushed by the robot into the compliant layer in order to transfer the deformable component to the target 3D object.

To the best of the authors knowledge, this concept to perform the application of deformable materials to target 3D objects was not published in the literature and is

4 Concept Study on Tape Application

not available as a commercial solution.

4.2.3 Tape Dispenser Tool

Supply at End-Effector

Robot employment	Robot kinematics	Contouring location	Material source	Material transport
Single robot	Moving tool	Dedicated machine	At end-effector	Liner

The robot-mounted tape dispenser tool with supply at the end-effector stores the pre-cut deformable components on a liner in form of a roll, see Fig. 4.9. Using a peeling mechanism the deformable material is separated from the liner and a compliant draping roll is used to transfer the material to the target 3D surface.

In the literature, many works associated to continuous tape placement for the FRP sector were published, i.e. ATL and AFP [9, 36], which are also well established commercially. A prototype for a continuous tape application system for a masking tape is presented in [53], which also incorporates object scanning and automatic path planning. The commercial solution ACCESS [50] uses pre-cut tapes on a liner to store the material at the end-effector and dispenses them in the given order onto the target 3D object.

Stationary Supply

Robot employment	Robot kinematics	Contouring location	Material source	Material transport
Single robot	Moving tool	Dedicated machine	Stationary	Liner

Figure 4.10 depicts the previous concept with a stationary supply, which feeds the pre-cut tapes to the robot-mounted application tool using a liner.

An implementation for continuous tape placement from a stationary supply was demonstrated in, e.g., [100] for a robotic winding cell and in [103] for a force-based AFP process. In systems like [103], the robot motion is limited significantly by the stationary feeding mechanism. Hence, additional DoF, like a moving or rotating workpiece table, are required to retain the flexibility. Commercial implementations perform a robotic taping task with a continuous tape from a stationary source [99] and build up the layers of FRP components similar to AFP utilizing a stationary supply [91]. However, solutions with pre-cut tapes provided by a stationary supply have not yet been published to the best of the author's knowledge.

4.2.4 Stationary Tape Dispenser

Liner

Robot employment	Robot kinematics	Contouring location	Material source	Material transport
Single robot	Moving 3D object	Dedicated machine	Stationary	Liner

This approach is depicted in Fig. 4.11 and uses a stationary dispensing mechanism and a liner to transport the deformable material. A single robot moves the target 3D object accordingly to perform the application process with the compliant draping roll.

This concept is consequently the kinematically reversed approach of the two previous solutions described in Section 4.2.3 “Tape Dispenser Tool”, cf. Fig. 4.6. Implementations of such an approach have neither been found in the literature nor in commercial

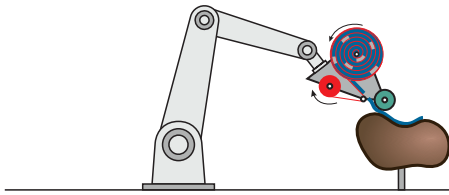


Figure 4.9: Tape dispenser tool with supply at end-effector.

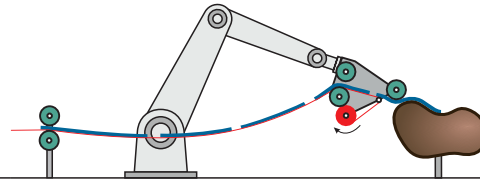


Figure 4.10: Tape dispenser tool with stationary supply.

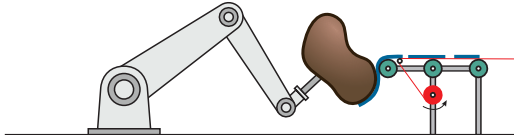


Figure 4.11: Stationary tape dispenser with liner.

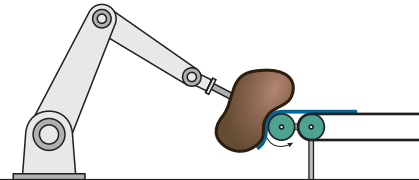


Figure 4.12: Stationary tape dispenser with conveyor belt.

solutions.

Conveyor Belt

Robot employment	Robot kinematics	Contouring location	Material source	Material transport
Single robot	Moving 3D object	Dedicated machine	Stationary	Conveyor belt

Similar to the previous concept, a single robot is used to perform appropriate draping motions in order to transfer the deformable material to the target 3D object. A conveyor belt transports the pre-cut deformable components to the dispensing mechanism of the stationary tape dispenser. This approach is illustrated in Fig. 4.12.

While no similar approaches are found in the literature, a commercial implementation is available for continuous tapes, i. e. a stationary tape dispenser for the continuous application of a vacuum tape [99].

4.2.5 Roll-Up Tool

Robot employment	Robot kinematics	Contouring location	Material source	Material transport
Single robot	Moving tool	Dedicated machine	Stationary	Gripper

The concept *roll-up tool*, see Fig. 4.13, uses a low-pressure area gripper with a cylindrical shape to pick up a pre-cut deformable component in a rolling motion from a dedicated contouring machine. This component is then transferred to the target 3D object using a reversed rolling motion.

The works [96, 104, 105] implement this approach for the application of technical textiles onto molds in the FRP sector. Integrated heaters precondition the deformable material according to the requirements of the draping process.

4.2.6 Multi-Robot Cell

Robot employment	Robot kinematics	Contouring location	Material source	Material transport
Multi-robot	Moving tool	Dedicated machine	Stationary	Gripper

In the *multi-robot cell* concept, two robots are utilized for transporting and draping of the deformable material from a stationary contouring machine, see Fig. 4.14.

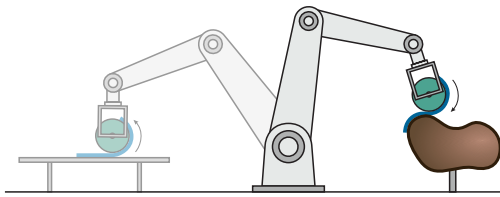


Figure 4.13: Roll-up tool.

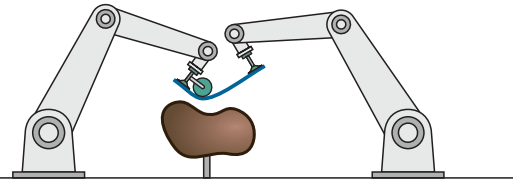


Figure 4.14: Multi-robot cell.

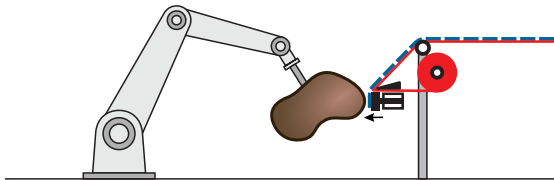


Figure 4.15: Additive method: Unit patch application.

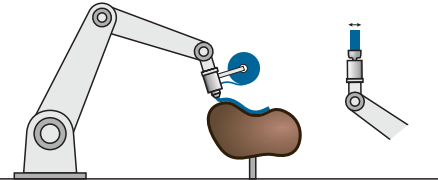


Figure 4.16: Additive method: 3D Printing.

Both robots are equipped with standard grippers, while one robot additionally has a compliant draping roll mounted on the flange. By performing coordinated robot motions, the deformable component is picked up from the stationary contouring machine, tensioned using the draping roll and brought into contact with the target 3D object. The draping motion is performed by the first robot while the tension is maintained using the second robot.

In the literature, several two-robot solutions were proposed. The work [70] uses the two-armed BAXTER robot to wind towels around 3D objects using a kinematic planning approach. With an FRP application in mind, [98] implements a dual-robot approach for handling technical textiles using custom-built gripper systems. Similarly, [106] represents a large-scale implementation of this concept. Recently, also a prototype for a commercial system called “LOWFLIP” (Low Cost Flexible Integrated Composite Process) [46] was published. In this work, two position-controlled 6-axis robots are used to handle and tension the strip while a third position-controlled robot consolidates the deformable material on the target 3D object. A closed-loop force-controlled system was proposed by [47] for the handling of strip-like fiber glass textiles using a gantry robot with three robot arms.

4.2.7 Additive Methods

Unit Patch Application

Robot employment	Robot kinematics	Contouring location	Material source	Material transport
Single robot	Moving 3D object	(none)	Stationary	Feed

In this concept, the shape of the deformable component is not contoured from an areal raw material, but is built up from a large number of individual small entities, the so-called *unit patches*. Thus, the contouring step is omitted in this solution. The unit patches are provided as pre-cut entities on a liner, as illustrated in Fig. 4.15, and are transferred to the moving 3D object using an electromagnetically actuated stamping mechanism or using an air-blast principle.

As of writing this thesis, such a concept for creating deformable components directly on the target object has not yet been proposed in the literature or is commercially

used. However, fast air-blast mechanisms for up to 800 unit patches per minute [93, 94] for transferring unit patches are commercially available. These solutions constitute the basic building blocks of the proposed approach.

3D Printing

Robot employment	Robot kinematics	Contouring location	Material source	Material transport
Single robot	Moving tool	(none)	At end-effector	Liner

By reducing the unit patch size of the previous concept to an infinitesimal size, the discrete patches become a continuum, i.e. a viscous fluid. Similar to the previous concept, the shape on the target 3D object is created by building it from individual lines of printed material, as shown schematically in Fig. 4.16. Moreover, a wider printing nozzle can be used to create areal shapes and to reduce processing time.

The 3D printing technology, in particular fused deposition modeling (FDM), has become a manufacturing method for rapid prototyping, but also for mass production in the last decades [85]. To increase the overall flexibility, also industrial robots are used for the movement of the print head or the build plate of the 3D printing system. Commercial examples are [107–109], which are designed for large-scale 3D printing in construction industry and architecture. Those methods use simple layer-by-layer methods to build up the objects.









In contrast, full 6-DoF movement is utilized in the printing process of advanced manufacturing approaches presented in the literature. The works [110, 111] exploit the flexibility of high-DoF systems to precisely manufacture thin freeform parts and avoid the stair-step effect known from standard 3D printing processes. An application to construct composite parts using a continuous glass fiber strand is given in [112], which can create freeform FRP components. Also in the context of FRP, the work [113] presents a combination of AFP and a 3D printing process, which is used to fill the gaps occurring during the lay-up of the fiber parts. Advanced algorithms achieve support-free 3D printing using a stationary print-head and a moving build plate mounted on a 6-DoF robot [114], and generate collision-free robot trajectories [115]. Finally, classical 2D printing directly on the freeform 3D surfaces is demonstrated in [116, 117] using a 6-DoF robot with serial kinematics. Moreover, 3D printing is demonstrated in [111] using a 6-DoF GOUGH-STEWART mechanism, which is a robot with parallel kinematics.

4.3 Evaluation

In this section, the ten distinct concepts proposed in the previous section are qualitatively evaluated and compared. The evaluation criteria are derived from Section 4.1.1 “Problem Statement” and are listed in Table 4.1.

The performance criteria *accuracy*, *speed* and *flexibility* rate each concept with the categories **low**, **medium** or **high** and the respective scores 0.0, 0.5 and 1.0 are assigned. The rows *normal force* and *tension force* indicate the capability to establish force-controlled applications and are categorized as **no** and **yes**, giving a score of 0.0 and 1.0, respectively. Finally, the economic suitability of each concept is rated in terms of *complexity* and *risk of design* and the categories **high**, **medium** or **low** with the corresponding scores 0.0, 0.5 and 1.0. Note the reverse order in coloring

Table 4.1: Evaluation criteria and associated categories and scores.

Criterion	Description	0.0	0.5	1.0
Accuracy 	Accuracy with which the deformable material can be placed on the target 3D object	low	medium	high
Speed 	Amount of deformable material, which can be transferred to the target object per unit time	low	medium	high
Flexibility 	Versatility with respect to the shape of the deformable material and the shape of the target 3D object	low	medium	high
Normal force 	Capability to impose a defined normal force during application	no		yes
Tension force 	Capability to impose a defined tension force during application	no		yes
Complexity 	Overall difficulty and effort for the development and implementation of the concept using existing and proven technology	high	medium	low
Risk of design 	Assessment of fundamental issues in the concept which need proof-of-concept	high	medium	low
Overall score 	Sum of all scores for each individual concept			

and scoring of the economic criteria compared to the performance criteria.

The results of the evaluation for the ten concepts proposed in Section 4.2 “Concepts” are summarized in Table 4.2 and are discussed in detail in the following for each individual evaluation criterion. For the following discussion, the concepts are numbered from #1 to #10.





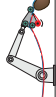



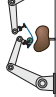


Accuracy  *Accuracy* is the expected ability of a concept to accurately place a deformable component on the desired location on the target 3D object. The first two concepts #1 “Shape-adaptive gripper” and #2 “Shape-adaptive table” provide low control over the position of the deformable component due to the compliant shape-adaptive surface of the gripper and the table, respectively. Similarly, concept #7 “Roll-up tool” requires a distinct compliant layer to allow for sufficient adaptation to the target 3D object. In contrast to #1 and #2, medium accuracy is expected, as the roll-up tool has a line-contact between the tool and the target 3D object, rather than an areal contact. Thus,

Table 4.2: Qualitative evaluation table for the concepts presented in Section 4.2 “Concepts”.

Number	#1	#2	#3	#4	#5	#6	#7	#8	#9	#10
Label	“Shape-adaptive gripper”	“Shape-adaptive table”	“Tape dispenser tool with supply at end-effector”	“Tape dispenser tool with stationary supply”	“Stationary tape dispenser with liner”	“Stationary tape dispenser with conveyor belt”	“Roll-up tool”	“Multi-robot cell”	“Unit patch application”	“3D Printing”
Sketch										
Accuracy	low	low	high	high	high	high	medium	high	high	high
Speed	low	medium	medium	medium	high	high	low	low	medium	low
Flexibility	low	low	medium	medium	medium	medium	low	medium	high	high
Normal force	no	no	yes	yes	yes	yes	yes	yes	yes	no
Tension force	no	no	yes	yes	yes	yes	no	yes	no	no
Complexity	high	high	low	low	low	medium	high	medium	medium	low
Risk of design	low	medium	medium	medium	medium	low	low	low	high	low
Overall score	1.0	1.0	5.5	5.5	6.0	6.0	2.5	5.0	4.0	4.0


4 Concept Study on Tape Application


the contact point between the roll-up tool and the target 3D object is more clearly defined. The remaining concepts #3, #4, #5 and #6 and #9 are based on a liner or a conveyor belt to feed the material and, hence, provide high accuracy. High accuracy is also expected for concept #8 “Multi-robot cell”, as the deformable material is grasped from the cutting table and placed on the target 3D object precisely using the available robot accuracy. Similarly, high accuracy is also expected for concept #10 “3D Printing”, where the material is directly applied to the target 3D object without any intermediate step.


Speed 🌀 The criterion *speed* evaluates the amount of deformable material which can be transferred to the target 3D object in a given time period. Thus, the highest speeds are expected for the concepts #5 “Stationary tape dispenser with liner” and #6 “Stationary tape dispenser with conveyor belt”, proposed in Section 4.2.4, as only the target 3D object mounted on the robot is the moving mass in these concepts. Moreover, the contouring and the application step can be performed in parallel. The speed of concept #2 “Shape-adaptive table” is considered medium due to the required additional process step to transfer the deformable component from the contouring machine to the shape-adaptive table. Heavy robot tools limit the processing speed for concepts #3 and #4, where the former even incorporates the material supply. Furthermore, concept #9 “Unit patch application” is considered a medium-speed solution, as the areal deformable components are built up from a large number of small entities. Similarly, in #10 “3D Printing”, the material is applied line-wise with rather small line width and, thus, the speed is rated low. Low application speeds are also expected for #1 “Shape-adaptive gripper” and #7 “Roll-up tool” due to the large mass of the gripping tool, which limits the movement dynamics. Additionally, the low-pressure area gripping principle used in these concepts provides low gripping forces, which also limits the acceleration and deceleration exerted on the grasped deformable material. Finally, #8 “Multi-robot cell” is also considered a low-speed solution, since the two robots have to repeatedly move between the contouring machine and the target 3D object for each deformable component and the application is performed by a sequence of robot motions, see [47].

Flexibility 🌀 The criterion *Flexibility* assesses the versatility of the proposed concepts with respect to the shape of the deformable components and of the target 3D objects. The criterion incorporates the ability of the concepts to drape deformable material on convex and concave areas with small and large curvature. To this end, the concepts #1 “Shape-adaptive gripper” and #2 “Shape-adaptive table” provide the least flexibility, especially for concave surfaces with high curvature. Similarly, the flexibility of #7 “Roll-up tool” is mainly determined by the roll radius, which is desired to be small for concave areas. The circumference of the roll also determines the maximum length of the deformable component and therefore limits the flexibility of this approach. Concepts #3 to #6 are rated with medium flexibility. While these concepts involve a draping roll with a small radius, the deformable component has to be applied to the target 3D object in a single continuous robot motion, which limits the versatility of these approaches. The flexibility is also limited for concept #8 “Multi-robot cell” due to the limited robot workspace and the re-

quired overlap of the workspaces of the two robots. The two concepts involving additive methods, i. e. #9 “Unit patch application” and #10 “3D Printing”, provide the most flexibility, since the robot motion does not need to be a continuous motion. Thus, the robot tool or the target 3D object can be reoriented at any time during the application process, which strongly increases the reachability on the target 3D object.


Normal force  The criterion *normal force* determines whether a concept is capable of imposing a defined normal force on the deformable material during the application process. The concepts #1 “Shape-adaptive gripper” and #2 “Shape-adaptive table” can generate a normal force, however, a defined interaction force between the compliant shape-adaptive surface and the target 3D object cannot be achieved. The large-area contact of the compliant layer of the gripper or the table causes an imprecise interaction between the compliant layer and the target 3D object. Moreover, concept #10 “3D Printing” cannot impose normal forces during material application since the 3D printing material is transferred to the surface in liquid form and turns solid after cooling. The remaining concepts #3 “Tape dispenser tool with supply at end-effector” to #9 “Unit patch application” rely on a point contact or a line contact for the force interaction with the target 3D object and, thus, can apply a defined normal force during the application process.


Tension force  The criterion *tension force* indicates whether a concept is capable of applying defined tension forces to the deformable material during application. Concepts #1 “Shape-adaptive gripper”, #2 “Shape-adaptive table” and #7 “Roll-up tool” rely on the rather small gripping forces of a low-pressure area gripper and, thus, cannot impose desired tension forces. Similarly, #9 “Unit patch application” can only impose normal forces by utilizing the stamping mechanism. As the 3D printing material in #10 “3D Printing” is transferred in melted form and turns solid after cooling on the surface, tension forces cannot be generated in the applied material during the application process. In contrast, the liner-based methods #3, #4 and #5 can provide tension forces during the application process by relying on the adhesion between the liner and the deformable material. Similarly, #6 “Stationary tape dispenser with conveyor belt” allows for tension forces, when an additional actuated clamping roll on the conveyor belt is used to tension the deformable material. With a suitable choice for the gripping principle to grasp and transport the deformable material, tension forces can also be exerted in concept #8 “Multi-robot cell”, see [47].

Complexity  The *complexity* rating assesses the overall difficulty and effort for the development and implementation of each proposed concept based on existing and proven technology. High complexity indicates that most aspects of a concept have to be newly developed and cannot be sourced from commercial or standard solutions. Concepts #1, #2 and #7 require a fully custom-designed tool for the transfer of the deformable material. Hence, the complexity of these concepts is rated high. An additional solution is required for #2 to transport the deformable components from the contouring machine to the shape-adaptive table. Though Concept #8 “Multi-robot cell” is built from standard robotics

4 Concept Study on Tape Application

hardware components only, it requires a more complex software solution to coordinate the multiple robot arms and grippers, which yields a medium rating for the complexity. The complexity is also rated medium for #6 “Stationary tape dispenser with conveyor belt”, as an additional supporting system is required to individualize the pre-cut deformable components prior feeding them with the conveyor belt. Medium complexity is estimated for #9 “Unit patch application”, since a fast stamping or air-blast mechanism has to be developed for this concept. Concepts #3, #4 and #5 use a liner during contouring, storing, transporting and applying the deformable components to the target 3D object. As these tasks are well known in the industry, standard components can be used and the complexity of these solutions is considered to be low. Finally, solution #10 “3D Printing” is rated with low complexity, as it uses a standard 3D printing tool mounted on the robot end-effector.

Risk of design  *Risk of design* refers to the percentage of each design, where a proof-of-concept is pending and fundamental issues may occur. The solutions and demonstrations known from the literature or from industrial applications serve as a starting point for this assessment. In this sense, concepts #1, #7 and #8 were already published in a similar form, which is outlined in the respective subsection of each concept. Similarly, #10 “3D Printing” relies on standard components and yields a low risk rating. Concept #6 “Stationary tape dispenser with conveyor belt” is also rated low, as it combines a kinematically reversed version of ATL and AFP [9] with an individualization step for the deformable components [44]. For concepts #3, #4 and #5, the amount of tension forces which can be imposed during the application process is not known in advance and must be experimentally validated. Hence, a medium risk rating is set for these concepts. For concept #2, the layout of the deformable material on the compliant layer of the shape-adaptive table is considered to be solved. However, transferring deformable material to a 3D object using a pushing motion requires further experimental investigations. High risk is estimated for #9 “Unit patch application”, as the combination of a robot motion with a fast and repetitive application of unit patches yet needs experimental approval.

Overall score  For each qualitative category, the score according to Table 4.1 is assigned and summed for each concept to yield the *overall score*, which ranges from 0.0 to 7.0. The overall scores of this qualitative study show that the most suitable approaches for the application task are #5 “Stationary tape dispenser with liner” and #6 “Stationary tape dispenser with conveyor belt”. Moreover, also the liner-based methods #3 and #4 show high scores.

4.4 Discussion

The goal of the concept study conducted in this chapter is to find the most suitable approach for the given task stated in Section 4.1.1 “Problem Statement”. In this section, the selection of the most suitable concept is described first and afterwards the limitations and possible remedies of the selected concept are discussed.

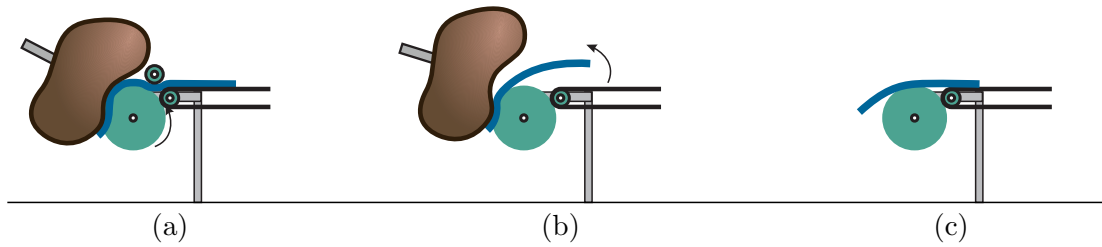


Figure 4.17: Considerations for #6 “Stationary tape dispenser with conveyor belt”. (a) Additional actuated clamping roll to allow for tension forces during the application process. (b) Lift-off of the deformable material at the end of the draping process. (c) Lift-off of the deformable material at the initial position.

4.4.1 Concept Selection

The evaluation of the previous section resulted in the two most promising concepts #5 “Stationary tape dispenser with liner” and #6 “Stationary tape dispenser with conveyor belt” with a score of 6.0, which is close to the maximum of 7.0. Both concepts, see Fig. 4.11 and Fig. 4.12, provide high accuracy for the placement of the deformable component on the target 3D object, since the deformable components are fed in a controlled and accurate way to the draping roll and the positioning of the target 3D object is accomplished by a (calibrated) industrial robot. High depositing speeds are expected for both concepts because the contouring process and the application process can be parallelized. Moreover, the application process is performed simultaneously with the feeding of the deformable material, i. e. separate gasping and transporting steps are not required for these concepts. The flexibility for both concepts is rated medium since the draping process requires a single continuous robot motion, which is limited by the workspace of the robot and the joint limits. However, using a proper placement of the stationary tape dispenser in the workspace of the robot as well as a thorough path planning, the limited flexibility is expected to be remedied. With the robot-mounted moving target 3D object, the complex and heavy contouring machine remains stationary and can be optimized for high contouring and feeding speeds. Furthermore, also the material source is stationary in these two concepts, which circumvents down-time for refilling materials.

4.4.2 Limitations and Remedies

Both concepts #5 and #6 are capable of imposing a defined normal force during the application process when a force/torque (F/T) sensor mounted on the robot flange is used during motion control. In order to apply tension forces in concept #6, an additional actuated clamping roll is required to tension the deformable material during application, see Fig. 4.17a. In the case of #5, the adhesive forces between the liner and the deformable material are able to generate a limited amount of tension forces without a clamping roll.

Further considerations for the application process are illustrated in Fig. 4.17b and Fig. 4.17c, which apply to both concepts #5 and #6. As shown in Fig. 4.17b, the deformable material can lift off from the feeding mechanism at the end of the application process if the material is too stiff. This undesired behavior can be

4 Concept Study on Tape Application

resolved by adding a (passive) clamping roll. A lift-off situation can also occur at the beginning of the application process, which can be remedied by using the principle of a low-pressure area gripper for the compliant layer of the draping roll. The areal low-pressure forces hold the deformable material on the draping roll in place until the first contact between the draping roll and the target 3D object occurs.

5

Application of Curved Tapes on 3D Objects

Based on the results of Chapter 4 “[Concept Study on Tape Application](#)”, this chapter deals with the implementation and demonstration of the selected concepts for the application of (curved) pre-cut adhesive tapes on freeform 3D surfaces. In particular, the selected concepts #5 “[Stationary tape dispenser with liner](#)” and #6 “[Stationary tape dispenser with conveyor belt](#)” use a single robot with the target 3D object mounted on the end-effector and a stationary tape application tool. Thus, the approach provides high flexibility with respect to the shape of the target 3D objects and the pre-cut tapes, as well as the lay-up location.

This implementation is an experimental validation of the surface-based path following control concept, introduced in Chapter 3. In the tape application process, this control concept is used to perform draping motions on known target 3D objects, i. e. traversing the tape application tool along a surface-based path. Additionally, the approach takes into account the kinematic constraints and redundancies to achieve a versatile and flexible solution. The proposed solution is suited for different applications in the production of textiles, apparel and consumer goods, in the industry of fiber reinforced plastics for the lay-up of technical textiles, and in the packaging industry.

The experimental setup, its hardware and software structure, is explained in detail in the first section, followed by an overview of the implemented tape application process and its individual process steps. Afterwards, the terms of 3D tape application paths and ribbons are introduced. In the fourth section, the control concept derived in Chapter 3 “[Surface-Based Path Following Control](#)” is applied to the tape application process by considering the kinematic requirements of this task. After describing the details of the implementation on the real-time hardware in the fifth section, the experimental results are presented in the final section of this chapter.

Large parts of this chapter will be published in similar form in [118].

5 Application of Curved Tapes on 3D Objects

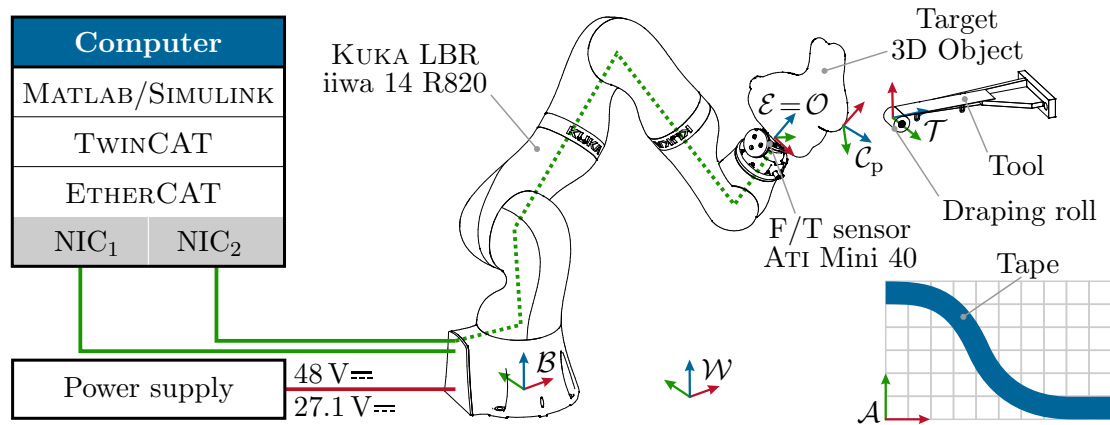


Figure 5.1: Schematic drawing of the experimental setup with coordinate frames for the tape application process.

5.1 Experimental Setup

The experimental setup is depicted in Fig. 5.1 as schematic drawing and consists of the robot KUKA LBR iiwa 14 R820, equipped with the 6-axis force/torque (F/T) sensor ATI Mini 40, a power supply, a desktop computer and the passive, wall-mounted tape application tool with a compliant draping roll, which will be detailed in Section 5.1.2 “Tape Application Tool” below. The target 3D object is mounted on the tool side of the F/T sensor. The robot and the F/T sensor are interfaced by two network interface cards (NIC) via the industrial protocol ETHERCAT. The controller is implemented as MATLAB/SIMULINK module, which is executed in the real-time automation software BECKHOFF TWINCAT.

In the following subsections, the coordinate frames and the tape application tool used in this application are described in detail, followed by a discussion about the characteristics of the experimental setup.

5.1.1 Coordinate Frames

The robot base frame \mathcal{B} and the tape application tool frame \mathcal{T} are defined stationary relative to the inertial (world) coordinate frame \mathcal{W} , see Fig. 5.1. Note that the y -axis of the tool frame \mathcal{T} (in green) is aligned with the draping roll axis. The end-effector frame \mathcal{E} is attached to the tool side of the F/T sensor and coincides with the object frame \mathcal{O} of the target 3D object, i. e. $\mathcal{E} = \mathcal{O}$. The position and orientation of the contact point on the target 3D object is described by the contact frame \mathcal{C}_p . The pre-cut adhesive tape is given in its planar state, i. e. before being transferred to the freeform 3D surface, in the planar coordinate frame \mathcal{A} .

5.1.2 Tape Application Tool

Based on the results of Chapter 4 “Concept Study on Tape Application” and considerations discussed in Section 4.4 “Discussion”, a prototypical design for the tape application tool is presented in this section. The two concepts #5 “Stationary tape dispenser with liner” and #6 “Stationary tape dispenser with conveyor belt” received the highest scores in the evaluation in Section 4.3 “Evaluation”. It is ad-

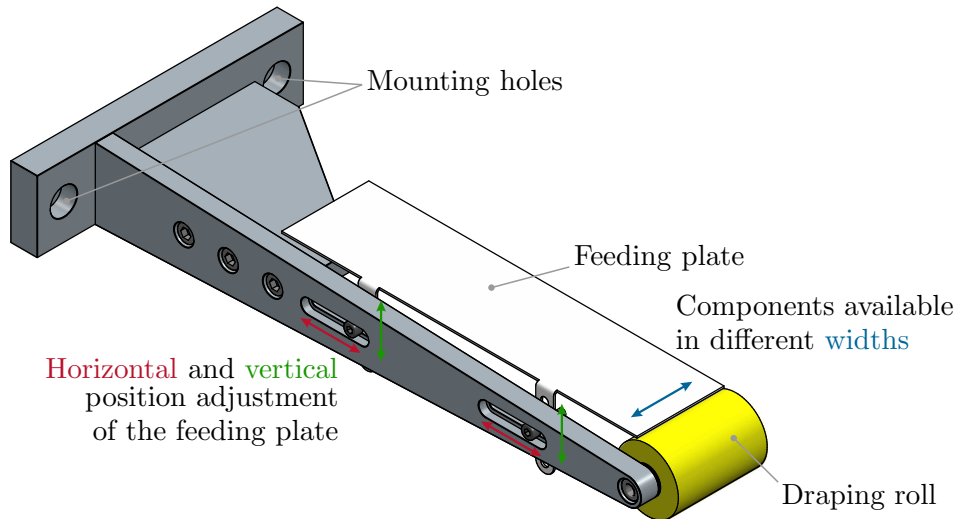


Figure 5.2: Drawing of the experimental tape application tool for the application process comprising a feeding plate and a passive non-actuated draping roll with a compliant layer.

vantageous to capture the basic principle of both concepts in the first design of the tape application tool, i. e. the application process of deformable materials and the robot motion, rather than the contouring or feeding process. From the view of the application process, the two concepts #5 and #6 are equal, since both concepts utilize a compliant draping roll for the interaction with the target 3D object. This allows to represent both concepts with a single prototypical design.

A detailed drawing of the experimental tape application tool is depicted in Fig. 5.2, which comprises a (passive) draping roll with a compliant layer and a feeding plate. The draping roll is not actuated and is supported by ball bearings. The position of the feeding plate can be adjusted accordingly using two orthogonal slotted holes. These components are manufactured in different widths, i. e. 30 mm, 50 mm and 100 mm, to allow for a wide variety of different shapes and sizes of the deformable material.

As the feeding mechanism in this prototypical design is simplified, the pre-cut deformable material is manually laid on the feeding plate with the adhesive side up. The robot moves the target 3D object to the draping roll and establishes the physical contact with the deformable material on the draping roll. In the further application process, the deformable component is clamped between the compliant draping roll and the target 3D object and is simultaneously fed during the draping motion. The non-actuated compliant draping roll is a suitable component for the interaction with the target 3D object, since it feeds the material at the desired speed. This mechanism relies on the tangential friction forces imposed on the draping roll, which are significantly larger than the friction torques caused by the ball bearings of the draping roll and the inertial torques originating from the draping roll inertia. The contouring and the feeding process are not considered with the proposed tape application tool. Due to the absence of an actuated clamping roll, see Section 4.4.2 “Limitations and Remedies”, tangential forces cannot be imposed during the application process using this first prototype.

5 Application of Curved Tapes on 3D Objects

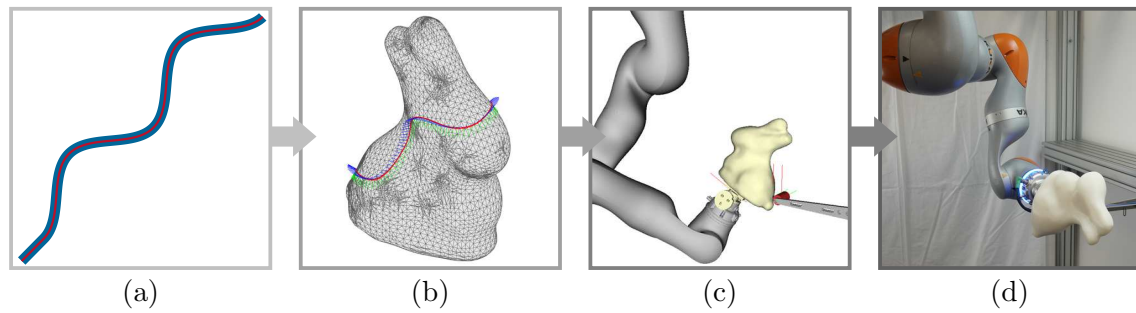


Figure 5.3: Tape application process overview: (a) 2D tape application path, (b) 3D path mapping, (c) Robot starting pose, (d) Preparation and execution.

5.1.3 Characteristics

The experimental setup depicted in Fig. 5.1 exhibits several characteristics, which are detailed in the following:

- In contrast to most works in the literature [9, 36, 43, 54, 95, 102], the draping tool in this work is stationary and the target 3D object is moving. While the relative motion between the tool and the workpiece is kinematically equivalent for the proposed prototypical design, it allows to remove the complex and heavy tape application tool [36] from the robot, see Section 4.3 “Evaluation”. Additionally, the tape supply as well as a contouring and separation mechanism can be incorporated into the stationary tool.
- The F/T sensor is mounted on the robot flange, which is industry standard and hence easy to integrate into a robot system.
- The experiments shown in this chapter focus on the interaction normal forces of the application process and consider the robot kinematics and dynamics between the compliant draping roll and the target 3D object.
- As the target 3D object is mounted on the robot end-effector, the maximum size of the target 3D object is given by the workspace and the maximum payload of the robot.
- The non-actuated, compliant draping roll allows only to impose normal forces throughout the tape application process. While this is sufficient for many applications [9, 40, 119], adding an additional actuated clamping roll also allows for tape tension forces during the process.

5.2 Process Overview

Using the previously described experimental setup, the tape application process is illustrated in Fig. 5.3 and consists of the following steps:

- (a) *2D tape application path*: A planar pre-cut tape is given by its shape and the corresponding planar tape application path (red line).
- (b) *3D path mapping*: The geometry and curvature of the planar tape application path is mapped onto the CAD model of the target 3D object, which creates a 3D tape application path described by a natural ribbon, see Section 3.2.6

“Curved Paths”. Thus, the planar and the 3D tape application path represent a matching pair of target lines [70].

- (c) *Robot starting pose*: The tape application process is simulated to determine a suitable starting joint configuration for the robot which results in a collision-free execution and has a reasonable reserve with respect to the joint limits.
- (d) *Preparation and execution*: The pre-cut tape is manually placed in the required starting position on the feeding plate of the application tool and the robot performs the compliance-controlled tape application process.

5.3 Tape Application Paths

A pre-cut adhesive tape is fully described by its planar tape application path given in the planar coordinate system \mathcal{A} only [70], see Fig. 5.3a. In order to perform the application process using surface-based path following control, the planar path is mapped onto the freeform 3D surface, creating a 3D tape application path in the object frame \mathcal{O} .

First, the geodesic curvature $\kappa_g(p)$ according to (3.17), as well as the lateral and geodesic positions $\pi_l(p)$ and $\pi_g(p)$ from (3.19) and (3.20), respectively, are calculated from the planar tape application path in the planar coordinate frame \mathcal{A} . Second, the 3D tape application path is calculated from these quantities, which describe all geometric properties of the planar path. The path is computed in surface coordinates $\mathbf{s}^T = [s_1 \ s_2]$ by integrating the system of differential equations (3.24) using the geodesic curvature $\kappa_g(p)$ and the initial values (3.16). The initial values define the starting point $\mathbf{s}_0^T = [s_{1,0} \ s_{2,0}]$ and the starting direction $\mathbf{t}_0 = s'_{1,0}\boldsymbol{\sigma}_{s_1} + s'_{2,0}\boldsymbol{\sigma}_{s_2}$ and are given by the desired placement of the tape on the freeform 3D surface. Hence, the 2D planar path in the planar frame \mathcal{A} and the 3D path in the object frame \mathcal{O} represent a matching pair of target lines [70]. Finally, the calculated path $\boldsymbol{\pi}(p)$ from (3.24) is complemented with the surface normal vector field $\boldsymbol{\sigma}_n(\mathbf{s}(p))$ to constitute the natural ribbon $(\boldsymbol{\pi}(p), \boldsymbol{\sigma}_n(\mathbf{s}(p)))$, i. e. the 3D tape application ribbon.

5.4 Tape Application Controller

The tape application controller performs the tape application process by traversing a 3D tape application ribbon $(\boldsymbol{\pi}(p), \boldsymbol{\sigma}_n(\mathbf{s}(p)))$, i. e. a path $\boldsymbol{\pi}(p)$ defined on a freeform 3D surface complemented with the surface normal vector field $\boldsymbol{\sigma}_n(\mathbf{s}(p))$, with the draping roll. This task is illustrated in Fig. 5.4. During the draping process, the robot motion must prevent any turns of the draping roll, described by the tool frame \mathcal{T} , around the surface normal vector $\boldsymbol{\sigma}_n(\mathbf{s}(p))$ to avoid wrinkles and distortions of the applied tape. To this end, the parallel contact frame \mathcal{C}_p introduced in Section 3.3.2 “Parallel Contact Frame” provides the required properties, see Fig. 5.4. Additionally, the rotation of the tool frame \mathcal{T} around the draping roll axis is free to a certain extent and, hence, poses a kinematic redundancy for the robot motion. The interaction between the draping roll and the freeform 3D surface uses the compliance controller defined in Section 3.5.1 “Impedance Control”, which is robust against errors in the tangential and lateral position, as well as deviations in the orientation from the

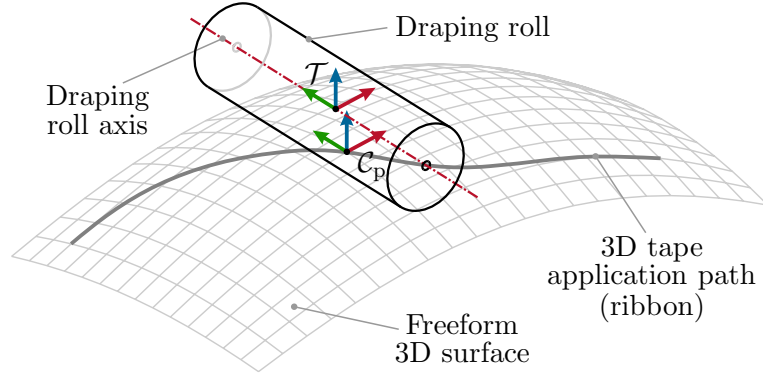


Figure 5.4: Schematic drawing of the task performed by the tape application controller. The underlying parallel contact frame \mathcal{C}_p prevents turns of the draping roll around the surface normal vector.

surface normal vector.

In the following, the tape application controller is presented based on the control concept introduced in Chapter 3 “Surface-Based Path Following Control”. First, the kinematic equations for the tape application process are derived, which take into account the stationary tape application tool frame \mathcal{T} . Based on these relations, the controller is designed, which incorporates the kinematic constraints and redundancies for the tape application process. Finally, optimization procedures are presented to find the optimal robot/tool position for a given target 3D object and the optimal initial robot configuration for a given 3D tape application path.

5.4.1 External Tool Kinematics

As shown in Fig. 5.1, the demonstrator setup uses an inertially fixed tape application tool with the tool frame \mathcal{T} . On the contrary, the 3D tape application ribbon $(\boldsymbol{\pi}(p), \boldsymbol{\sigma}_n(s(p)))$ is described in the object frame \mathcal{O} , which is identical to the end-effector frame \mathcal{E} . In terms of homogeneous transformations, see Section 2.1.1 “Homogeneous Transformations”, the kinematic relations are described by

$$\mathbf{H}_{\mathcal{O}}^{\mathcal{T}}(\mathbf{q}) = \mathbf{H}_{\mathcal{O}}^{\mathcal{E}} \mathbf{H}_{\mathcal{E}}^{\mathcal{B}}(\mathbf{q}) \mathbf{H}_{\mathcal{B}}^{\mathcal{W}} \mathbf{H}_{\mathcal{W}}^{\mathcal{T}}. \quad (5.1)$$

In this setup, $\mathcal{E} = \mathcal{O}$ and thus, $\mathbf{H}_{\mathcal{O}}^{\mathcal{E}} = \mathbf{I}$. Note that (5.1) contains the inverse transformation of the forward kinematics of the robot $\mathbf{H}_{\mathcal{B}}^{\mathcal{E}}(\mathbf{q})$ in (2.6). Based on (5.1), the output $\mathbf{y} \in \mathbb{R}^6$ of the system (3.59) for this application is chosen as Cartesian position $\mathbf{y}_t \in \mathbb{R}^3$ and orientation $\mathbf{y}_r \in \mathbb{R}^3$ of the tool frame \mathcal{T} with respect to the object frame \mathcal{O} in the form, cf. (2.7),

$$\mathbf{y} = \begin{bmatrix} \mathbf{y}_t \\ \mathbf{y}_r \end{bmatrix} = \begin{bmatrix} \mathbf{d}_{\mathcal{O}}^{\mathcal{T}}(\mathbf{q}) \\ \phi(\mathbf{R}_{\mathcal{O}}^{\mathcal{T}}(\mathbf{q})) \end{bmatrix} = \mathbf{h}(\mathbf{q}). \quad (5.2)$$

Similar to (2.12), the analytical Jacobian $\mathbf{J}(\mathbf{q})$ for the output (5.2) is given by

$$\dot{\mathbf{y}} = \begin{bmatrix} \dot{\mathbf{y}}_t \\ \dot{\mathbf{y}}_r \end{bmatrix} = \left(\frac{\partial \mathbf{h}}{\partial \mathbf{q}} \right) (\mathbf{q}) \dot{\mathbf{q}} = \mathbf{J}(\mathbf{q}) \dot{\mathbf{q}}, \quad (5.3)$$

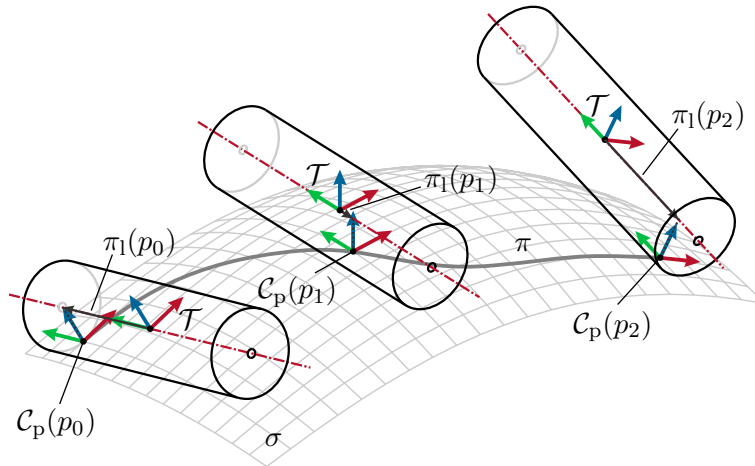


Figure 5.5: Geometric relationships of a draping motion along a curved path π on a doubly-curved surface σ for multiple path positions $p_0 < p_1 < p_2$.

5.4.2 Controller Design

In this section, the tape application controller is designed using the theoretical foundations of Chapter 3 “Surface-Based Path Following Control”. In the following subsections, the kinematic constraints and redundancies, as well as the task space and the nullspace controllers are discussed.

Kinematic Constraints

The geometric relationships of a draping motion along a curved path π on a doubly-curved surface σ are illustrated in Fig. 5.5 for multiple path positions $p_0 < p_1 < p_2$. The tape application controller takes into account the kinematic constraints imposed by the tape application process by utilizing the parallel contact frame $\mathcal{C}_p(p)$, i. e. rotations of the draping roll around the surface normal vector have to be prevented to avoid wrinkles and distortions in the applied tape, see Fig. 5.5. This property is provided by the parallel contact frame $\mathcal{C}_p(p)$. Additionally, the relative motion between the tool frame \mathcal{T} and the contact frame $\mathcal{C}_p(p)$ along the draping roll axis must be considered to prevent a sliding motion of the draping roll in lateral direction. Instead, the draping roll must be tilted around the parallel surface tangent vector (red vector in Fig. 5.5), which moves the contact point appropriately in lateral direction using the calculated lateral position $\pi_1(p)$ (black arrows in Fig. 5.5).

Coordinate Transformation

The coordinate transformation of the tape application process uses the parallel projection operator $P_p(\mathbf{y}_t)$ with the condition (3.44) and the parallel contact frame $\mathcal{C}_p(p)$ given in (3.43). The parallel contact frame $\mathcal{C}_p(p)$ is derived from the 3D tape application ribbon $(\pi(p), \sigma_n(\mathbf{s}(p)))$ and the parallel tangent vector field $\pi_p(p)$, which is calculated from (3.41) with the initial conditions (3.42). Thus, the coordinate transformation is given by (3.55) with the analytical Jacobian (5.3).

This choice for the parallel contact frame precisely matches the kinematic constraints of the draping process, as described in Section 5.4.2 “Kinematic Constraints” and illustrated in Fig. 5.5. On the one hand, the desired orientation of the draping roll

5 Application of Curved Tapes on 3D Objects

axis is given by the \mathbf{e}_2 -axis (green vector in Fig. 5.5) of the parallel contact frame $\mathcal{C}_p(p)$ for all $p \in I$, see (3.43). This prevents rotations of the draping roll around the surface normal vector. On the other hand, curved paths have to be traversed by tilting the draping roll with respect to the \mathbf{e}_1 -axis (red vector in Fig. 5.5) of the parallel contact frame $\mathcal{C}_p(p)$. Simultaneously, the contact point between the draping roll and the freeform 3D surface shifts accordingly along the lateral direction. This displacement is taken into account by moving the tool frame \mathcal{T} with respect to the parallel contact frame $\mathcal{C}_p(p)$ along the \mathbf{e}_2 -axis by the lateral position $\pi_1(p)$.

Single-Axis Tool Redundancy and Feedback Linearization

During the tape application process, the contact point between the draping roll and the freeform 3D surface can move freely – up to a given extent limited by the mechanical construction – around the circumference of the draping roll. Thus, the tape application tool exhibits a single-axis tool redundancy for the rotation around the y -axis of the tool frame \mathcal{T} .

Following the lines of Section 3.6.1 “Single-Axis Tool Redundancy”, the TAIT-BRYAN convention $\phi = \phi_{zxy}(\mathbf{R}_O^T)$ is chosen to represent the orientation with the redundant tool axis $r = y$. Then the reduced task space is derived according to (3.83) and (3.84), based on the coordinate transformation (3.55). Finally, the static state feedback (3.86) is applied to the rigid-body system (3.59) with (3.60) which yields the linear system (3.87) in the reduced coordinates $\tilde{\mathbf{y}}$.

Task Space Controller

Compliance control, as introduced in (3.67), is implemented for the reduced task space of the tape application process in the form

$$\tilde{\mathbf{v}} = \ddot{\tilde{\mathbf{y}}}^d + (\mathbf{M}^d)^{-1} \left(-\mathbf{D}^d(\dot{\tilde{\mathbf{y}}} - \dot{\tilde{\mathbf{y}}}^d) - \mathbf{K}^d(\tilde{\mathbf{y}} - \tilde{\mathbf{y}}^d) \right), \quad (5.4)$$

with the constant diagonal controller gain matrices \mathbf{M}^d , \mathbf{K}^d and \mathbf{D}^d as defined in (3.66). While a F/T sensor is present on the robot flange, see Section 5.1 “Experimental Setup”, it is used to verify the interaction forces between the tool and the target 3D object only. The desired trajectory $(\tilde{\mathbf{y}}^d, \dot{\tilde{\mathbf{y}}}^d, \ddot{\tilde{\mathbf{y}}}^d)$ is given as a \mathcal{C}^2 -trajectory in terms of position, velocity and acceleration. Thus, the chosen control scheme is robust against errors in the tangential and lateral position, as well as in the orientation of the non-redundant axes x and z of the tool frame \mathcal{T} .

The tape application path is traversed with a suitable \mathcal{C}^2 -trajectory for ξ_1^d , which transitions the tangential coordinate from the start position $\xi_1^d = 0$ mm to the end of the tape. The desired trajectory ξ_3^d specifies the draping roll motion along the surface normal vector and allows to approach the draping roll, establish and release the contact with the target 3D object. The draping roll axis is – in the absence of control errors – aligned with the \mathbf{e}_2 -axis of the contact frame $\mathcal{C}_p(p^*)$, see Fig. 5.5. Thus, the desired trajectory for the orientation coordinates of the draping roll is given by $\xi_4^d \equiv 0$ and $\xi_5^d \equiv 0$. As the draping roll axis follows the \mathbf{e}_2 -axis of the contact frame $\mathcal{C}_p(p^*)$, choosing $\xi_2^d = -\pi_1(p^*)$ for the lateral motion of the draping roll (see Fig. 5.5) correctly takes into account the lateral movement of the contact point and prevents a lateral sliding motion of the draping roll. Instead, the roll is tilted with respect to the \mathbf{e}_1 -axis of the contact frame and the contact point

moves in lateral direction appropriately. Finally, the tape application normal force is adjusted using the impedance parameters m_3^d , k_3^d and d_3^d corresponding to the reference impedance model of the coordinate ξ_3 , see (3.65).

Nullspace Controller

In the nullspace of the tape application task, the hierarchical nullspace controller with two levels (3.81) introduced in Section 3.6.1 “Single-Axis Tool Redundancy” is implemented. The individual inputs $\boldsymbol{\tau}_{n,1}$ and $\boldsymbol{\tau}_{n,2}$ are chosen according to (3.93) and (3.95), respectively. Hence, the first level stabilizes the y -axis of the tool frame \mathcal{T} and takes into account the joint limits of the robot axes as well as the kinematic limits for the redundant tool axis. The second level stabilizes the elbow motion of the kinematically redundant 7-axis robot.

5.4.3 Optimal Initial Robot Pose

An initial robot pose for the draping motion of a given 3D tape application path is found by solving the inverse kinematics problem (2.16) for the initial contact frame $\mathcal{C}_p(p_0)$ at the beginning of the 3D tape application ribbon $(\boldsymbol{\pi}(p_0), \boldsymbol{\sigma}_n(\mathbf{s}(p_0)))$. However, the solution of this problem is not unique, since the kinematic redundancy of the robot (elbow-plane angle ψ , see (2.17)) and the single-axis tool redundancy of the draping roll (orientation coordinate ξ_6) lead to additional degrees of freedom for the inverse kinematics problem.

In general, there are different options to solve this problem. For example, a simple approach is to calculate the inverse kinematics of the first contact point only, considering all available degrees of freedom. However, this approach fails for very long application paths since it does not consider the robot motion associated with the path and the corresponding joint limits. There are also more systematic ways to solve this problem, like a geometric planning approach which chooses the robot starting pose according to the required robot motion. For example, if a tape should be wrapped 360° around the target object, the robot needs to start in an initial pose which allows for this rotation at the end-effector. Additionally, such an approach can be supported by a pre-computed database of tape locations, shapes and corresponding initial robot poses, which speeds up the search. In this work, an optimization-based approach is derived in the following to find a suitable initial robot pose for each pre-cut tape to be applied.

In general, the homogeneous transformation for the desired tool frame \mathcal{T} is given by the initial contact frame $\mathcal{C}_p(p_0)$, which is translated along the surface normal vector (z -axis) by the roll radius r_r and rotated around the redundant tool axis (y -axis) by a nullspace angle $\xi_{6,0}$, i. e.

$$\mathbf{H}_{\mathcal{O}}^{\mathcal{T}}(\xi_{6,0}) = \mathbf{H}_{\mathcal{O}}^{\mathcal{C}_p(p_0)} \mathbf{H}_{Tz,r_r} \mathbf{H}_{Ry,\xi_{6,0}} = \begin{bmatrix} \mathbf{R}_{\mathcal{O}}^{\mathcal{T}}(\xi_{6,0}) & \mathbf{d}_{\mathcal{O}}^{\mathcal{T}}(\xi_{6,0}) \\ \mathbf{0} & 1 \end{bmatrix}. \quad (5.5)$$

In the coordinates of the system output, this is

$$\mathbf{y}(\xi_{6,0}) = \begin{bmatrix} \mathbf{d}_{\mathcal{O}}^{\mathcal{T}}(\xi_{6,0}) \\ \phi(\mathbf{R}_{\mathcal{O}}^{\mathcal{T}}(\xi_{6,0})) \end{bmatrix}. \quad (5.6)$$

5 Application of Curved Tapes on 3D Objects

Note that $\xi_{6,0} \in X_6$, where X_6 is the set of admissible angles for the coordinate ξ_6 . Using the inverse kinematics introduced in (2.16), the set of all robot poses of all admissible angles $\xi_{6,0} \in X_6$ is found as the union

$$\tilde{Q} = \bigcup_{\xi_{6,0} \in X_6} \mathbf{h}^{-1}(\mathbf{y}(\xi_{6,0})) , \quad (5.7)$$

with the inverse kinematics $\mathbf{h}^{-1}(\mathbf{y})$ of (5.2). Using the above set of all admissible joint-space solutions \tilde{Q} , which incorporates the elbow-plane angle ψ and the single-axis tool redundancy angle $\xi_{6,0}$, the optimal initial robot pose \mathbf{q}_0^* is found as a solution of the dynamic optimization problem

$$\mathbf{q}_0^* = \arg \min_{\mathbf{q}_0 \in \tilde{Q}} \left(a_1 \int_{t_0}^{t_1} \|\tilde{\mathbf{b}}(t)\|^2 dt + a_2 \max_{t \in [t_0, t_1]} \|\tilde{\mathbf{b}}(t)\|_\infty + a_3 \int_{t_0}^{t_1} \|\dot{\mathbf{q}}(t)\|^2 dt \right) \quad (5.8a)$$

$$\text{s.t. (3.59) with (3.60), (3.86), (5.4), (3.81), (3.93), (3.95) ,} \quad (5.8b)$$

$$\mathbf{q}(t_0) = \mathbf{q}_0 , \quad (5.8c)$$

$$\dot{\mathbf{q}}(t_0) = \mathbf{0} , \quad (5.8d)$$

with the weights a_1 , a_2 and a_3 , and the barrier functions (3.89) and (3.92) combined to

$$\tilde{\mathbf{b}}(t) = \begin{bmatrix} \mathbf{b}(\mathbf{q}(t)) \\ b_{\xi_6}(\xi_6(t)) \end{bmatrix} . \quad (5.9)$$

Note that the constraints in (5.8b) encompass the dynamic rigid-body system of the robot including the task space and nullspace controllers. The dynamic optimization problem (5.8) is used to find the time evolution of $\mathbf{q}(t)$ and $\dot{\mathbf{q}}(t)$ for $t \in [t_0, t_1]$ with the initial conditions (5.8c) and (5.8d). For each solution of (5.8b) with $\mathbf{q}_0 \in \tilde{Q}$, the cost functional (5.8a) is evaluated. This cost functional comprises three components:

1. The integral of the norm of $\tilde{\mathbf{b}}(t)$ generates costs when the robot motion enters the proximity of a joint limit or the limit of the single-axis tool redundancy ξ_6 .
2. The maximum of the infinity-norm of $\tilde{\mathbf{b}}(t)$ punishes the highest instantaneous value in the vector of the barrier functions $\tilde{\mathbf{b}}(t)$. It is undesired for the robot to operate close to joint limits as the controller needs some reserves in view of the robustness of the solution. Due to the construction of the barrier functions (3.89), (3.90) and (3.92), this value rises drastically when a joint comes close to its limit.
3. The integral of the norm of $\dot{\mathbf{q}}(t)$ curbs the joint velocities in the optimal solution and leads to smooth solutions.

The posed problem in (5.8) is of high complexity, as it comprises the nonlinear system dynamics and control inputs (5.8b) and the nonlinear barrier functions (5.9). To circumvent these issues, the two-dimensional search space $(\xi_{6,0}, \psi)$ spanned by (5.7) and (2.17) is discretized using the discrete sets

$$\begin{aligned} X_6 &= \{0^\circ, 10^\circ, \dots, 90^\circ\} , & |X_6| &= 10 , \\ \Psi &= \{-180^\circ, -157.5^\circ, -135^\circ, \dots, 157.5^\circ\} , & |\Psi| &= 16 , \end{aligned}$$

where $|\cdot|$ denotes the cardinality of the set. Thus, the inverse kinematics (5.7) has a maximum of $8|X_6||\Psi| = 1280$ solutions. In practice, the number of physically feasible solutions is significantly reduced due to the robot joint limits listed in Appendix A.2. Therefore, the optimization problem (5.8) is feasible to be solved using the exhaustive search method.

5.5 Implementation

The tape application controller is derived in continuous time t and for smooth 3D tape application ribbon $(\boldsymbol{\pi}(p), \boldsymbol{\sigma}_n(\mathbf{s}(p)))$. For the practical implementation, a temporal discretization of the control algorithm and a spatial discretization of the target 3D objects must be performed.

The controller is implemented as MATLAB/SIMULINK module, which is executed via the real-time automation software BECKHOFF TWINCAT on a desktop computer with the sampling time $T_s = 125 \mu\text{s}$. The F/T sensor is sampled with $T_{s,F/T} = 333 \mu\text{s}$. In the following, the index k of a quantity refers to the time $t = kT_s$, $k = 0, 1, 2, \dots$, i. e. $\xi_k = \xi(t)|_{t=kT_s}$.

In this section, the basic robot control aspects of the demonstrator setup are stated first. Subsequently, discrete-space paths and surfaces are introduced and based on this, a systematic analysis of the optimal robot/tool position is presented. Using these results, the discrete-time version of the surface-based path following control is derived. Finally, mathematical relations for the contact force estimation are presented.

5.5.1 Robot Control

The robot KUKA LBR iiwa 14 R820 is controlled directly using BECKHOFF TWINCAT via ETHERCAT at torque level and without robot controller, as illustrated in Fig. 5.1. For friction compensation, the disturbance observer presented in [120] estimates the friction torques $\boldsymbol{\tau}_f$ for all joints from the motor positions $\boldsymbol{\theta}$ and the measured joint torques $\boldsymbol{\tau}$. The observer is implemented for each axis of the robot in discrete time, reading as

$$\hat{\boldsymbol{\tau}}_{f,k} = -\mathbf{F} \mathbf{B}(\dot{\boldsymbol{\theta}}_k - \hat{\dot{\boldsymbol{\theta}}}_k) \quad (5.10a)$$

$$\dot{\hat{\boldsymbol{\theta}}}_{k+1} = \dot{\hat{\boldsymbol{\theta}}}_k + T_s \mathbf{B}^{-1}(\boldsymbol{\tau}_{m,k} - \boldsymbol{\tau}_k - \hat{\boldsymbol{\tau}}_{f,k}), \quad (5.10b)$$

where $\hat{\boldsymbol{\tau}}_{f,k}$ is the estimated friction torque and $\hat{\dot{\boldsymbol{\theta}}}_k$ is the estimated motor velocity, i. e. the state of the observer. The observer parameters $\mathbf{F} = \text{diag}(F_1, F_2, \dots, F_7)$ parametrize the time constant of the observer for each axis and are listed in Table A.2 in the Appendix. The compensation is performed by adding the estimated torques $\hat{\boldsymbol{\tau}}_{f,k}$ to the motor torques $\boldsymbol{\tau}_{m,k}$, cf. (2.23),

$$\boldsymbol{\tau}_{m,k} = \mathbf{u}_k - \mathbf{K}_\tau(\boldsymbol{\tau}_k - \mathbf{u}_k) - \epsilon \mathbf{D}_\tau \dot{\boldsymbol{\tau}}_k + \hat{\boldsymbol{\tau}}_{f,k}. \quad (5.11)$$

The joint positions \mathbf{q} cannot be measured directly, but are calculated from the measured signals of the motor positions $\boldsymbol{\theta}$ and the joint torques $\boldsymbol{\tau}$ via the linear

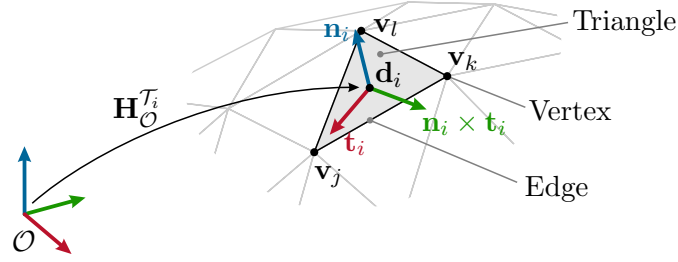


Figure 5.6: Discrete 3D object consisting of a sequence of vertices V and triangles T . Each triangle T_i exhibits a unique surface normal vector \mathbf{n}_i .

stiffness model (2.21). The time derivatives of the joint positions \mathbf{q} and joint torques $\boldsymbol{\tau}$ are calculated by approximate differentiation using a derivative element with first-order lag.

5.5.2 Discrete Surfaces

A discrete surface, also called *mesh*, consists of a set of triangles, which are interconnected by common edges and vertices as illustrated in Fig. 5.6. In contrast to non-uniform rational B-splines (NURBS) surfaces, a discrete surface is only of class \mathcal{C}^0 and is not continuously differentiable [121]. A discrete 3D object is given by a sequence of vertices V of length N and a sequence of triangles T of length M in the form

$$V = (\mathbf{v}_1, \mathbf{v}_2, \dots, \mathbf{v}_N) \quad (5.12)$$

$$T = (T_1, T_2, \dots, T_M), \quad (5.13)$$

where

$$\mathbf{v}_i = [v_{i,x} \ v_{i,y} \ v_{i,z}]^T, \quad (5.14)$$

i. e. each vertex \mathbf{v}_i , $i = 1, 2, \dots, N$, is given by its position in the object coordinate frame \mathcal{O} . Each triangle T_i , $i = 1, 2, \dots, M$, consists of the indices of three vertices in form of a 3-tuple as

$$T_i = (j, k, l), \quad \begin{aligned} i &\in \{1, 2, \dots, M\} \\ j, k, l &\in \{1, 2, \dots, N\}, \end{aligned} \quad (5.15)$$

and induces a unique triangle frame \mathcal{T}_i , see Fig. 5.6, reading as

$$\mathbf{H}_{\mathcal{O}}^{\mathcal{T}_i} = \begin{bmatrix} \mathbf{t}_i & \mathbf{n}_i \times \mathbf{t}_i & \mathbf{n}_i & \mathbf{d}_i \\ 0 & 0 & 0 & 1 \end{bmatrix}, \quad (5.16)$$

with

$$\mathbf{d}_i = \frac{1}{3}(\mathbf{v}_j + \mathbf{v}_k + \mathbf{v}_l) \quad (5.17)$$

$$\mathbf{t}_i = \frac{\mathbf{v}_j - \mathbf{d}_i}{\|\mathbf{v}_j - \mathbf{d}_i\|} \quad (5.18)$$

$$\mathbf{n}_i = \frac{(\mathbf{v}_k - \mathbf{v}_j) \times (\mathbf{v}_l - \mathbf{v}_j)}{\|(\mathbf{v}_k - \mathbf{v}_j) \times (\mathbf{v}_l - \mathbf{v}_j)\|}, \quad (5.19)$$

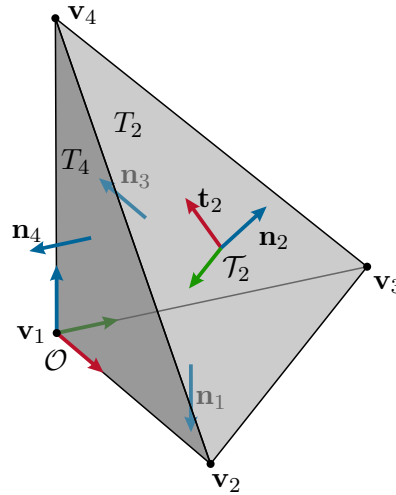


Figure 5.7: Tetrahedron consisting of four vertices V and four triangles T , which are listed in Table 5.1 and Table 5.2, respectively.

Table 5.1: Sequence of vertices V for the 3D object depicted in Fig. 5.7.

i	$v_{i,x}$	$v_{i,y}$	$v_{i,z}$
	m	m	m
1	0	0	0
2	1	0	0
3	0	1	0
4	0	0	1

Table 5.2: Sequence of triangles T for the 3D object depicted in Fig. 5.7.

i	T_i
1	(1,3,2)
2	(4,2,3)
3	(4,3,1)
4	(4,1,2)

for $i = 1, 2, \dots, M$ and with j, k, l from (5.15). This coordinate frame \mathcal{T}_i is defined relative to the object frame \mathcal{O} , has its origin \mathbf{d}_i at the center of mass of the three vertices of T_i , the x -axis pointing from the origin to the first vertex \mathbf{v}_j , and the surface normal vector \mathbf{n}_i as z -axis. Note that the order of the three vertices in each 3-tuple T_i specifies the surface normal direction using the right-hand rule.

As an example, Tables 5.1 and 5.2 list the sequence of vertices V and triangles T for the simple 3D object shown in Fig. 5.7. Moreover, this figure also depicts the triangle frame \mathcal{T}_2 according to (5.16).

5.5.3 Optimal Robot/Tool Position

In order to perform the application of deformable materials of various shapes and sizes to freeform 3D surfaces, the robot has to execute complex motions relative to the fixed tape application tool. Thus, the relative distance between the robot base frame \mathcal{B} and the tool frame \mathcal{T} is a crucial parameter for this approach. In the literature, a number of works were published with different methods for finding the optimal robot position when considering different optimization criteria. For example, kinematic manipulability [122, 123], stiffness [13, 14], cycle time [124, 125], torques [126], and combinations of these criteria [122] were proposed. In these works, the optimal robot position and orientation are typically found on the basis of a given

5 Application of Curved Tapes on 3D Objects

robot path or trajectory.

In contrast, for the problem at hand, only the target 3D object itself is given and no paths on this object are specified in advance. Thus, a novel optimization procedure is derived in the following to find the optimal relative robot/tool position such that a given target 3D object can be processed with maximum flexibility. To this end, the reachability of all triangles T of the target 3D object are considered in this optimization. Without loss of generality, this procedure can also be applied to a region of interest of the target 3D object, i. e. a subset $\tilde{T} \subseteq T$.

In the subsequent sections, the kinematic relations between the robot base frame \mathcal{B} , the tool frame \mathcal{T} and the triangle frames \mathcal{T}_i , $i = 1, 2, \dots, M$, are derived in mathematical terms. Then, the optimization problem is formulated. Finally, the optimization procedure is executed for the discrete target 3D object used in the experiments of this work.

Robot/Tool Kinematics

The homogeneous transformation between the robot base frame \mathcal{B} and the tool frame \mathcal{T} is given by

$$\mathbf{H}_{\mathcal{B}}^{\mathcal{T}} = \mathbf{H}_{\mathcal{B}}^{\mathcal{W}} \mathbf{H}_{\mathcal{W}}^{\mathcal{T}} = \mathbf{H}_{\mathcal{B}}^{\mathcal{W}} \begin{bmatrix} \mathbf{I} & \mathbf{d}_{\mathcal{W}}^{\mathcal{T}} \\ \mathbf{0} & 1 \end{bmatrix} \mathbf{H}_{\text{Ry}, -\frac{\pi}{2}}, \quad (5.20)$$

where the last transformation $\mathbf{H}_{\text{Ry}, -\frac{\pi}{2}}$ aligns the orientation of the tool frame \mathcal{T} as depicted in Fig. 5.1. Note that the tool frame origin $\mathbf{d}_{\mathcal{W}}^{\mathcal{T}}$ is the optimization variable to be determined and the transformation $\mathbf{H}_{\mathcal{B}}^{\mathcal{W}}$ is the known mounting position of the robot in the world frame \mathcal{W} .

An arbitrary contact frame \mathcal{C} on a triangle T_i , $i = 1, 2, \dots, M$, is given by the homogeneous transformation in the form, see (5.16),

$$\mathbf{H}_{\mathcal{O}}^{\mathcal{C}}(i, \theta) = \mathbf{H}_{\mathcal{O}}^{\mathcal{T}_i} \mathbf{H}_{\text{Rz}, \theta}, \quad (5.21)$$

where $\theta \in \Theta = [0, 2\pi)$ denotes an arbitrary rotation angle around the surface normal vector \mathbf{n}_i of the triangle frame \mathcal{T}_i . Thus, in order to establish contact with the draping roll in the contact frame \mathcal{C} , the tool frame \mathcal{T} has to be positioned with respect to the object frame \mathcal{O} at, see also (5.5),

$$\mathbf{H}_{\mathcal{O}}^{\mathcal{T}}(i, \theta, \xi_{6,0}) = \mathbf{H}_{\mathcal{O}}^{\mathcal{C}}(i, \theta) \mathbf{H}_{\text{Tz}, r_1} \mathbf{H}_{\text{Ry}, \xi_{6,0}} = \begin{bmatrix} \mathbf{R}_{\mathcal{O}}^{\mathcal{T}}(i, \theta, \xi_{6,0}) & \mathbf{d}_{\mathcal{O}}^{\mathcal{T}}(i, \theta, \xi_{6,0}) \\ \mathbf{0} & 1 \end{bmatrix}, \quad (5.22)$$

where $\xi_{6,0} \in X_6$ is an additional DoF originating from the single-axis tool redundancy of the draping roll. Hence, each triangle T_i , $i = 1, 2, \dots, M$, in (5.22) can be reached with the draping roll with different rotation angles θ and $\xi_{6,0}$ by positioning the tool frame \mathcal{T} according to $\mathbf{H}_{\mathcal{O}}^{\mathcal{T}}(i, \theta, \xi_{6,0})$.

Optimization Problem

The optimization process for the relative distance $\mathbf{d}_{\mathcal{W}}^{\mathcal{T}}$ takes into account the sequence of all triangles T of a given target 3D object as defined in (5.13) and does not specialize on a specific surface-based path $\pi(p)$. This has the advantage that the relative distance $\mathbf{d}_{\mathcal{W}}^{\mathcal{T}}$ is adjusted for an optimal overall reachability of all triangles of a target 3D object and the paths do not have to be known in advance.

The objective function to be maximized in the course of the optimization process is derived in the following. For a given tool frame origin $\mathbf{d}_{\mathcal{W}}^T$, this function evaluates the total number of different rotation angles θ with which each triangle T_i , $i = 1, 2, \dots, M$, can be reached. Using the task space coordinates of (5.22) in the form

$$\mathbf{y}(i, \theta, \xi_{6,0}) = \begin{bmatrix} \mathbf{d}_{\mathcal{O}}^T(i, \theta, \xi_{6,0}) \\ \phi(\mathbf{R}_{\mathcal{O}}^T(i, \theta, \xi_{6,0})) \end{bmatrix} \quad (5.23)$$

in

$$\tilde{Q}(i, \theta) = \bigcup_{\xi_{6,0} \in X_6} \mathbf{h}^{-1}(\mathbf{y}(i, \theta, \xi_{6,0})) \quad (5.24)$$

yields all solutions of the inverse kinematics for a given triangle $T_i \in T$ and rotation angle θ . By discretizing θ over the admissible range Θ using an equidistant grid with the increment $\Delta\theta$ and $N_{\Delta\theta}$ points, the number of reachable angles θ is counted for each triangle T_i with

$$N_i = \sum_{k=0}^{N_{\Delta\theta}-1} \begin{cases} 1 & \text{if } \tilde{Q}(i, k\Delta\theta) \neq \emptyset \\ 0 & \text{otherwise} \end{cases} \quad (5.25)$$

Using (5.25), the optimal robot/tool position $(\mathbf{d}_{\mathcal{W}}^T)^*$ is found as

$$(\mathbf{d}_{\mathcal{W}}^T)^* = \arg \max_{\mathbf{d}_{\mathcal{W}}^T \in \mathbb{R}^3} \frac{1}{MN_{\Delta\theta}} \sum_{i=1}^M N_i, \quad (5.26)$$

where the total number of reachable angles θ with any admissible redundancy angle $\xi_{6,0} \in X_6$ and any admissible elbow-plane angle $\psi \in \Psi$ for all triangles T is maximized. Note that the factor $1/MN_{\Delta\theta}$ normalizes the objective function to unity, see (5.13) and (5.25).

Demonstrator Target 3D Object

The optimization procedure (5.26) is applied to the demonstrator target 3D object shown in Fig. 5.3b. A preliminary MONTE-CARLO analysis of the objective function of (5.26) is conducted to identify a good starting solution for a subsequent direct-search optimization.

The MONTE-CARLO analysis is performed by evaluating 5000 points in the cuboid volume

$$\begin{bmatrix} -1.1 \text{ m} \\ -1 \text{ m} \\ 0.5 \text{ m} \end{bmatrix} \leq \mathbf{d}_{\mathcal{W}}^T \leq \begin{bmatrix} 0 \text{ m} \\ 1 \text{ m} \\ 2.1 \text{ m} \end{bmatrix}, \quad (5.27)$$

for a ceiling-mounted robot with

$$\mathbf{H}_{\mathcal{W}}^{\mathcal{B}} = \begin{bmatrix} 1 & 0 & 0 & 0 \text{ m} \\ 0 & -1 & 0 & 0 \text{ m} \\ 0 & 0 & -1 & 1.9 \text{ m} \\ 0 & 0 & 0 & 1 \end{bmatrix} \quad (5.28)$$

5 Application of Curved Tapes on 3D Objects

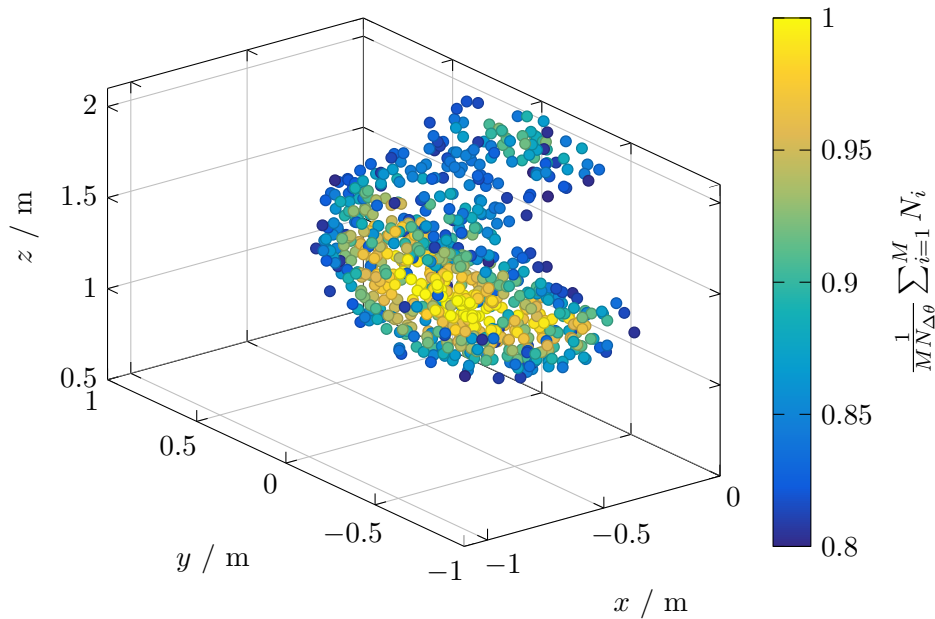


Figure 5.8: Objective function values for the preliminary MONTE-CARLO analysis of (5.26).

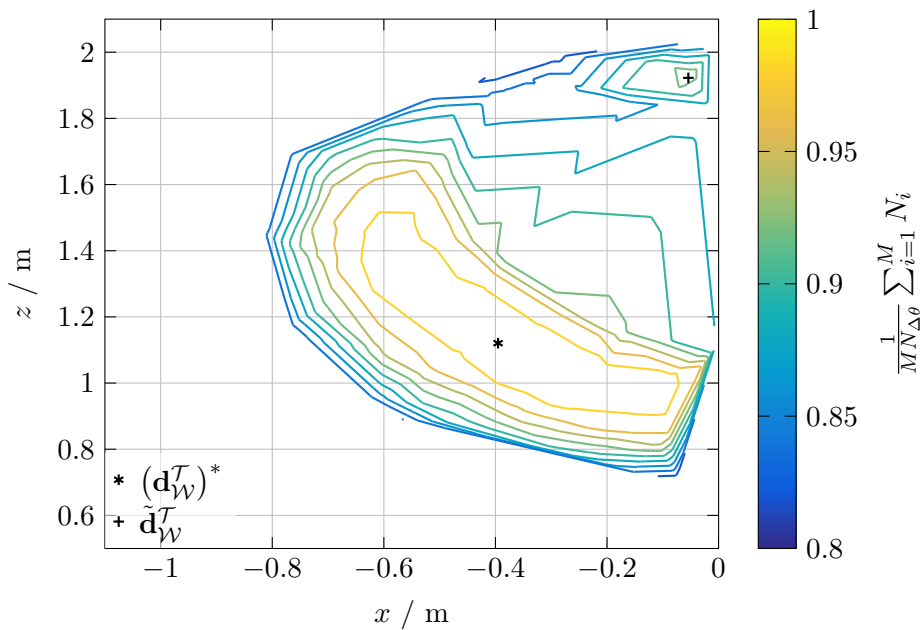


Figure 5.9: Contour plot of the plane $y = 0$ of Fig. 5.8. The black asterisk indicates the optimal robot/tool position $(\mathbf{d}_{\mathcal{W}}^T)^*$ and the black cross marks the local optimum $\tilde{\mathbf{d}}_{\mathcal{W}}^T$.

and the draping roll radius $r_r = 17.5$ mm. The resulting objective function values (5.26) of each robot/tool position $\mathbf{d}_{\mathcal{W}}^{\mathcal{T}}$ exceeding 0.8 is displayed in Fig. 5.8 and a contour plot for the intersection plane $y = 0$ is shown in Fig. 5.9. Note that due to performance aspects [59] the inverse kinematics algorithm based on homogeneous transformations as introduced in Section 2.1.4 “Inverse Kinematics” is utilized. These preliminary results show a mirror symmetry with respect to the plane $y = 0$ and the existence of a distinct maximum for the optimal robot/tool position $\mathbf{d}_{\mathcal{W}}^{\mathcal{T}}$.

The best solution of Fig. 5.8 is further refined by applying the NELDER-MEAD simplex algorithm [127] to (5.26). This heuristic direct search method does not need the gradient of the objective function. Figure 5.9 indicates the found optimal robot/tool position $(\mathbf{d}_{\mathcal{W}}^{\mathcal{T}})^*$ at

$$(\mathbf{d}_{\mathcal{W}}^{\mathcal{T}})^* = \begin{bmatrix} -0.395 \text{ m} \\ 0.016 \text{ m} \\ 1.121 \text{ m} \end{bmatrix} \quad (5.29)$$

and a local optimum $\tilde{\mathbf{d}}_{\mathcal{W}}^{\mathcal{T}}$ at

$$\tilde{\mathbf{d}}_{\mathcal{W}}^{\mathcal{T}} = \begin{bmatrix} -0.054 \text{ m} \\ 0.001 \text{ m} \\ 1.922 \text{ m} \end{bmatrix}, \quad (5.30)$$

with the objective function values of 0.9999 and 0.9331, respectively. For $(\mathbf{d}_{\mathcal{W}}^{\mathcal{T}})^*$ from (5.29), the reachability value $N_i/N_{\Delta\theta}$, $i = 1, 2, \dots, M$, for each triangle $T_i \in T$ of the demonstrator object is depicted in Fig. 5.10. The corresponding histogram for the distribution of the triangle reachability value $N_i/N_{\Delta\theta}$ is shown in Fig. 5.11 with a logarithmic y -axis. This evaluation reveals that merely 0.35 % of all triangles $T_i \in T$ exhibit a reachability value $N_i/N_{\Delta\theta}$ below 0.95. The red frame in Fig. 5.10 marks the respective triangles on the target 3D object. Thus, the optimal robot/tool position $(\mathbf{d}_{\mathcal{W}}^{\mathcal{T}})^*$ allows to reach all triangles and almost any orientation θ using some elbow-plane angle ψ and draping roll angle $\xi_{6,0}$.

5.5.4 Discrete Tape Application Paths

If the target 3D object is given as discrete surface, the procedure of Section 3.2.6 “Curved Paths” has to be adapted to account for the properties of discrete-space objects.

As in the continuous case, the path geometry is computed in terms of the geodesic curvature $\kappa_g(p)$, the lateral position $\pi_1(p)$ and the geodesic position $\pi_g(p)$ from the planar parametrized path $\boldsymbol{\pi}(p)$ in the planar coordinate system \mathcal{A} (see Fig. 3.3). The path on the discrete surface is calculated using Algorithm 1. For a given starting point $\boldsymbol{\sigma}(\mathbf{s}_0)$ on the surface and a tangent direction \mathbf{t}_0 , Algorithm 1 maps the planar path using the geodesic curvature $\kappa_g(p)$ onto the target 3D object, as illustrated in Fig. 5.12. By piecewise integration of (3.24), a continuous tape application path is calculated on each triangle. At the edges and vertices, the adjacent triangle and the corresponding starting point and tangent direction are found using method2b [121]. Using the current tangent direction of the tape application path \mathbf{t}_i on the

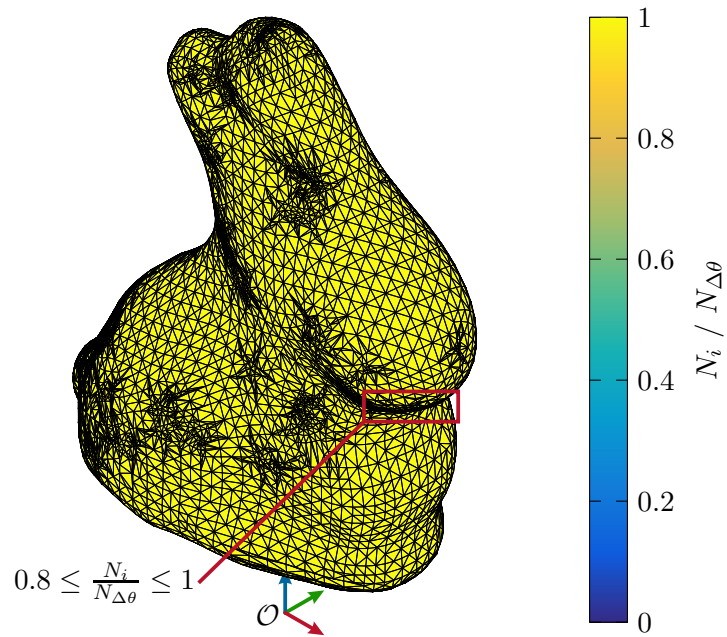


Figure 5.10: Reachability value $N_i/N_{\Delta\theta}$ for each triangle $T_i \in T$ of the demonstrator target 3D object.

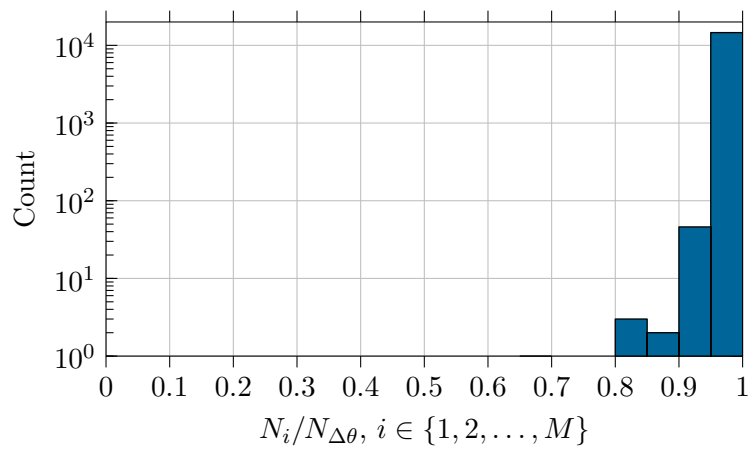


Figure 5.11: Logarithmic histogram of the reachability value $N_i/N_{\Delta\theta}$ for all triangles $T_i \in T$ of the demonstrator target 3D object.

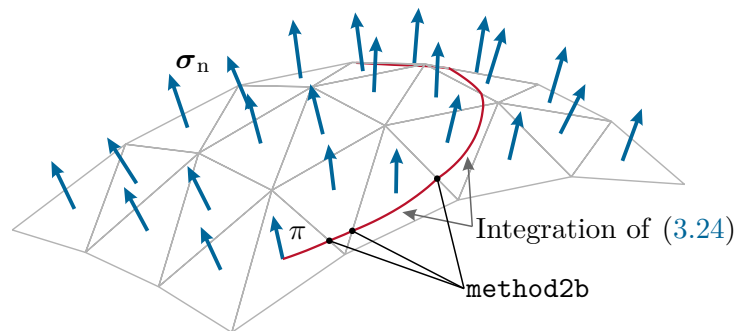


Figure 5.12: Triangle mesh surface with surface normal field σ_n and path π . The path π is calculated by piecewise integration of (3.24) and using method2b [121].

Algorithm 1 Map curved path on discrete surface

-
- 1: Initialize $\boldsymbol{\pi}(p_0) = \boldsymbol{\sigma}(\mathbf{s}_0)$
 - 2: Initialize $\boldsymbol{\pi}'(p_0) = \mathbf{t}_0$
 - 3: Find initial triangle containing $\boldsymbol{\pi}(p_0)$
 - 4: **for all** $p \in I$ **do**
 - 5: $\mathbf{s}_0 \leftarrow$ Current position $\boldsymbol{\pi}(p)$ in triangle coordinates
 - 6: $\mathbf{s}'_0 \leftarrow$ Current tangent $\boldsymbol{\pi}'(p)$ in triangle coordinates
 - 7: Integrate (3.24) using $\kappa_g(p)$ until an edge or vertex is reached at $p = p_e$
 - 8: $\boldsymbol{\pi}(p_e) \leftarrow \boldsymbol{\sigma}([s_1 \ s_2]^T)$
 - 9: $\boldsymbol{\pi}'(p_e) \leftarrow s'_1 \boldsymbol{\sigma}_{s_1} + s'_2 \boldsymbol{\sigma}_{s_2}$
 - 10: Transition to adjacent triangle using `method2b` [121]
 - 11: **end for**
-

triangle T_i , this algorithm computes the direction \mathbf{t}_{i+1} on the next triangle T_{i+1} by intersecting the triangle T_{i+1} with a plane constructed from the normal vector of the next triangle \mathbf{n}_{i+1} , the current tangent direction \mathbf{t}_i and position $\boldsymbol{\pi}(p_i)$.

As the discrete surface and the resulting path are of class \mathcal{C}^0 due to the vertices and edges between the triangles, the path has to be further smoothed before applying the control strategy. Hence, the path points are sampled equidistantly and are interpolated using \mathcal{C}^3 B-splines [128] to satisfy the smoothness requirements for the control strategy. Moreover, the *cumulative form* [129] is used to interpolate the orientations of the corresponding normal vectors as quaternions. In this form, quaternions are composed of an initial quaternion and a sequence of angular rotations, which are activated smoothly and sequentially by real-valued basis functions.

5.5.5 Discrete Surface-Based Path Following Control

In this section, the discrete-time version of the surface-based path following control for the tape application process is derived. As the tape application process uses the parallel contact frame $\mathcal{C}_p(p)$, introduced in (3.43), a discrete-time implementation of this frame is computed. Moreover, discretized implementations for the parallel projection operator $P_p(\mathbf{y}_t)$ with the condition (3.44) and the integral for the tangential coordinate ξ_1 in (3.48) are developed in the following.

Discrete-time Parallel Contact Frame

As highlighted in Section 5.4.2 “Kinematic Constraints”, the parallel contact frame $\mathcal{C}_p(p)$ introduced in Section 3.3.2 “Parallel Contact Frame” accurately describes the motion of the draping roll traversing along a surface-based path on a freeform 3D surface. Specifically, this frame avoids rotations around the surface normal vector. In other words, the unit vector field $\mathbf{e}_1(p)$ of $\mathcal{C}_p(p)$ in (3.43) is required to be a parallel vector field on the surface σ . According to (3.8), the derivative of this parallel vector field $\mathbf{e}_1(p)$ only comprises a vector component normal to the surface. A different path-based frame in differential geometry is the so-called *parallel transport frame*, which has similar properties. The parallel transport frame of a path does not rotate around the path tangent vector and the derivatives of the two transversal vectors are scalar multiples of the path tangent vector [24]. Hence, these similarities allow

5 Application of Curved Tapes on 3D Objects

to use the discrete-time implementation for the parallel transport frame according to [24] and adapt it to the parallel contact frame.

As the path $\boldsymbol{\pi}(p)$ and its surface normal vector field $\boldsymbol{\sigma}_n(\mathbf{s}(p))$ are interpolated independently using B-splines, the orthogonality property of the 3D tape application ribbon $(\boldsymbol{\pi}(p), \boldsymbol{\sigma}_n(\mathbf{s}(p)))$ is lost. To recover this property, the surface normal vector field is orthonormalized with respect to the path tangent (unit) vector field $\boldsymbol{\pi}'(p)$ using the GRAM-SCHMIDT process [130] in the form

$$\mathbf{e}_3(p) = \frac{\boldsymbol{\sigma}_n(\mathbf{s}(p)) - \boldsymbol{\sigma}_n^T(\mathbf{s}(p))\boldsymbol{\pi}'(p)\boldsymbol{\pi}'(p)}{\|\boldsymbol{\sigma}_n(\mathbf{s}(p)) - \boldsymbol{\sigma}_n^T(\mathbf{s}(p))\boldsymbol{\pi}'(p)\boldsymbol{\pi}'(p)\|}. \quad (5.31)$$

Using (5.31), the discrete-time parallel tangent vector field $\mathbf{e}_{1,k}$ is calculated from the discrete-time orthonormalized vector field $\mathbf{e}_{3,k} = \mathbf{e}_3(p_k)$ as, see [24, 131],

$$\mathbf{e}_{1,k} = \frac{\mathbf{e}_{1,k-1} - \mathbf{e}_{3,k}^T \mathbf{e}_{1,k-1} \mathbf{e}_{3,k}}{\sqrt{1 - (\mathbf{e}_{3,k}^T \mathbf{e}_{1,k-1})^2}} \quad (5.32a)$$

$$\mathbf{e}_{2,k} = \mathbf{e}_{3,k} \times \mathbf{e}_{1,k}. \quad (5.32b)$$

The initial tangent vector $\mathbf{e}_{1,0}$ is chosen as $\mathbf{e}_{1,0} = \boldsymbol{\pi}'(p_0)$ to coincide with the path tangent $\boldsymbol{\pi}'(p_0)$ at p_0 . Note that, compared to the parallel transport frame in [24, 131], the roles of the tangent and normal vector in (5.32a) are interchanged due to the geometric relations of the parallel contact frame illustrated above. With (5.32), the discrete-time implementation of the parallel contact frame $\mathcal{C}_p(p)$ from (3.43) is complete.

Discrete-time Parallel Projection Operator

The constraint of the projection operator $P_p(\mathbf{y}_t)$ in (3.44) is solved numerically with the NEWTON iteration

$$p_{k,i} = p_{k,i-1} - \frac{f(p_{k,i-1})}{f'(p_{k,i-1})}, \quad (5.33)$$

with $i = 1, 2, \dots$, and $f(p_{k,i}) = (\mathbf{y}_t - \boldsymbol{\pi}(p_{k,i}))^T \mathbf{e}_{1,k}$. The iteration is initialized with the path parameter of the previous time step, i. e. $p_{k,0} = p_{k-1}^*$ and terminates with $|p_{k,i} - p_{k,i-1}| < \varepsilon$, $\varepsilon > 0$. The resulting path parameter, denoted by p_k^* , indicates the projected position on the path. Note that due to exclusion of turning points, see Section 3.3.2 “Parallel Contact Frame”, a surface-based path π can only exhibit one solution of (3.44). Finally, the integral in (3.48) is solved numerically using the explicit EULER method

$$\xi_{1,k} = \xi_{1,k-1} + (p_k^* - p_{k-1}^*)(\boldsymbol{\pi}'(p_k^*))^T \mathbf{e}_{1,k}. \quad (5.34)$$

5.5.6 Contact Force Estimation

The contact forces and torques $\hat{\mathbf{f}}_e$ in the parallel contact frame $\mathcal{C}_p(p^*)$ cannot be measured directly on the surface of the target 3D object. Moreover, the measured forces and torques ${}_{\mathcal{E}}\mathbf{f}_s$ at the tool side of the F/T sensor also comprise the gravitational and dynamic forces of the target 3D object, which have to be compensated. The left index \mathcal{E} of ${}_{\mathcal{E}}\mathbf{f}_s$ refers to the coordinate frame of reference in which the force is described.

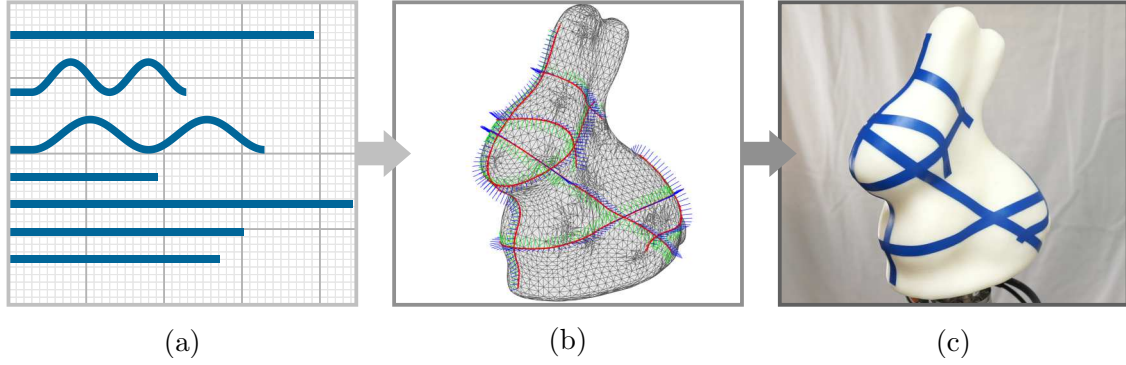


Figure 5.13: Experimental results of the tape application process on a 3D-printed object: (a) Pre-cut tapes (b) Projected paths on the target 3D object (c) Completed tape application process.

Experiments show that for slow and moderate end-effector tangential velocities it is sufficient to compensate only for the gravitational forces $\mathbf{f}_p^T = [0 \ 0 \ m_p g \ 0]$ of the payload mass m_p , where g is the gravitational acceleration. These gravitational forces \mathbf{f}_p are transformed to the end-effector frame \mathcal{E} using a force transformation, reading as [56]

$$\varepsilon \mathbf{f}_p = \begin{bmatrix} \mathbf{R}_{\mathcal{E}}^{\mathcal{W}}(\mathbf{q}) & \mathbf{0} \\ \mathbf{S}(\varepsilon \mathbf{p}_p) \mathbf{R}_{\mathcal{E}}^{\mathcal{W}}(\mathbf{q}) & \mathbf{R}_{\mathcal{E}}^{\mathcal{W}}(\mathbf{q}) \end{bmatrix} \mathbf{f}_p, \quad (5.35)$$

where $\varepsilon \mathbf{p}_p$ denotes the position vector of the center of mass of the payload in the end-effector frame \mathcal{E} . Note that the skew-symmetric operator $\mathbf{S}(\cdot)$ from (2.11) is applied to $\varepsilon \mathbf{p}_p$ in (5.35). The total external force $\varepsilon \mathbf{f}_e$ is calculated as

$$\varepsilon \mathbf{f}_e = \varepsilon \mathbf{f}_s - \varepsilon \mathbf{f}_p \quad (5.36)$$

and is again transformed using

$$\hat{\mathbf{f}}_e = \begin{bmatrix} \mathbf{R}_{\mathcal{E}}^{C_p} & \mathbf{0} \\ \mathbf{S}(\boldsymbol{\pi}(p^*)) \mathbf{R}_{\mathcal{E}}^{C_p} & \mathbf{R}_{\mathcal{E}}^{C_p} \end{bmatrix}^{-1} \varepsilon \mathbf{f}_e = [\hat{f}_{e,1} \ \hat{f}_{e,2} \ \dots \ \hat{f}_{e,6}]^T \quad (5.37)$$

to the current contact frame $C_p(p^*)$. Finally, the generalized external forces $\boldsymbol{\tau}_e$ in the state feedback (3.61) are calculated from the transformed external force (5.37) in the form

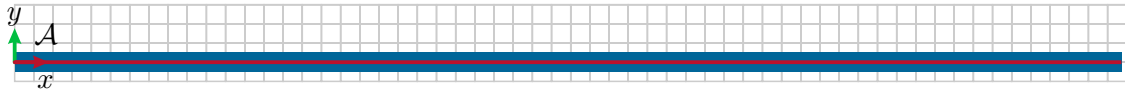
$$\boldsymbol{\tau}_e = \hat{\mathbf{J}}^T(\mathbf{q}) \hat{\mathbf{f}}_e. \quad (5.38)$$

5.6 Experimental Results

The surface-based path following control concept, adapted to the tape application process in Section 5.4 “Tape Application Controller” and extended for discrete-time implementation using discrete-space 3D objects in Section 5.5 “Implementation”, is demonstrated on a 3D-printed object, as shown in Fig. 5.13. The paths of the pre-cut tapes in (a) are mapped onto the discrete surface of the target 3D object in (b). The result of the tape application process is depicted in (c). In Table 5.3, the seven tapes of the experiments are listed with the respective length L_i , width W_i and geodesic length $\pi_{g,i}(L_i)$, $i = 1, 2, \dots, 7$. The barrier function parameters and the

Table 5.3: Geometry of the tapes depicted in Fig. 5.13a for the experimental tape application process.

i	Name	Curved	L_i mm	$\pi_{g,i}(L_i)$ mm	W_i mm
1	around	No	392	392	10
2	back	Yes	372	325	50
3	back-across	Yes	292	228	50
4	ears	No	192	192	10
5	left	No	442	442	10
6	mouth	No	302	302	10
7	silhouette	No	272	272	10

**Figure 5.14:** Tape “around” (see Table 5.3) and tape application path (red) for the experimental results shown in Fig. 5.15.

controller parameters of the tape application process are listed in the Appendix in Appendix A.2 and Table A.4, respectively. The optimal initial robot poses for each pre-cut tape is found using exhaustive search as detailed in Section 5.4.3 “Optimal Initial Robot Pose” with $a_1 = a_2 = a_3 = 1$. The contact forces and torques $\hat{\mathbf{f}}_e$, which are obtained as described in Section 5.5.6 “Contact Force Estimation”, are used to verify the interaction forces only and are not used for feedback in these experiments. In the following two subsections, the tape application procedures for the straight tape “around” (see Table 5.3) with a length of 392 mm and the curved tape “back” with a geodesic length of 325 mm are discussed. A video of the complete demonstration is found at www.acin.tuwien.ac.at/52f5.

5.6.1 Straight Tape

In this section, the application of the pre-cut tape “around” with a straight tape application path (see Table 5.3), depicted in Fig. 5.14, is described in detail. The measurement signals of the tape application process are shown in Fig. 5.15. In this figure, individual graphs are shown for the path-based position coordinates ξ_i and the corresponding desired values ξ_i^d , $i = 1, 2, 3$, the control errors $\tilde{\mathbf{e}}$ for the reduced task space $\tilde{\mathbf{y}}$, the angle of the redundant axis $\xi_6 - \xi_{6,0}$, the barrier function values $\mathbf{b}(\mathbf{q})$ and $b_{\xi_6}(\mathbf{q})$, the system inputs \mathbf{u} from (3.60), the motor torques $\boldsymbol{\tau}_m$ from (2.23) including friction compensation $\boldsymbol{\tau}_f$, the interaction forces and torques $\hat{\mathbf{f}}_e$ and the joint positions \mathbf{q} . The graphs are subdivided into three phases ①-③, as detailed in the following:

- ① *Contact establishment:* For each point along the surface-based path, the coordinate axis \mathbf{e}_3 of the parallel contact frame $\mathcal{C}_p(p)$ is parallel to the surface normal vector $\boldsymbol{\sigma}_n(\mathbf{s}(p))$. Thus, the corresponding coordinate ξ_3 is used for the approaching motion of the target 3D object towards the draping roll. Us-

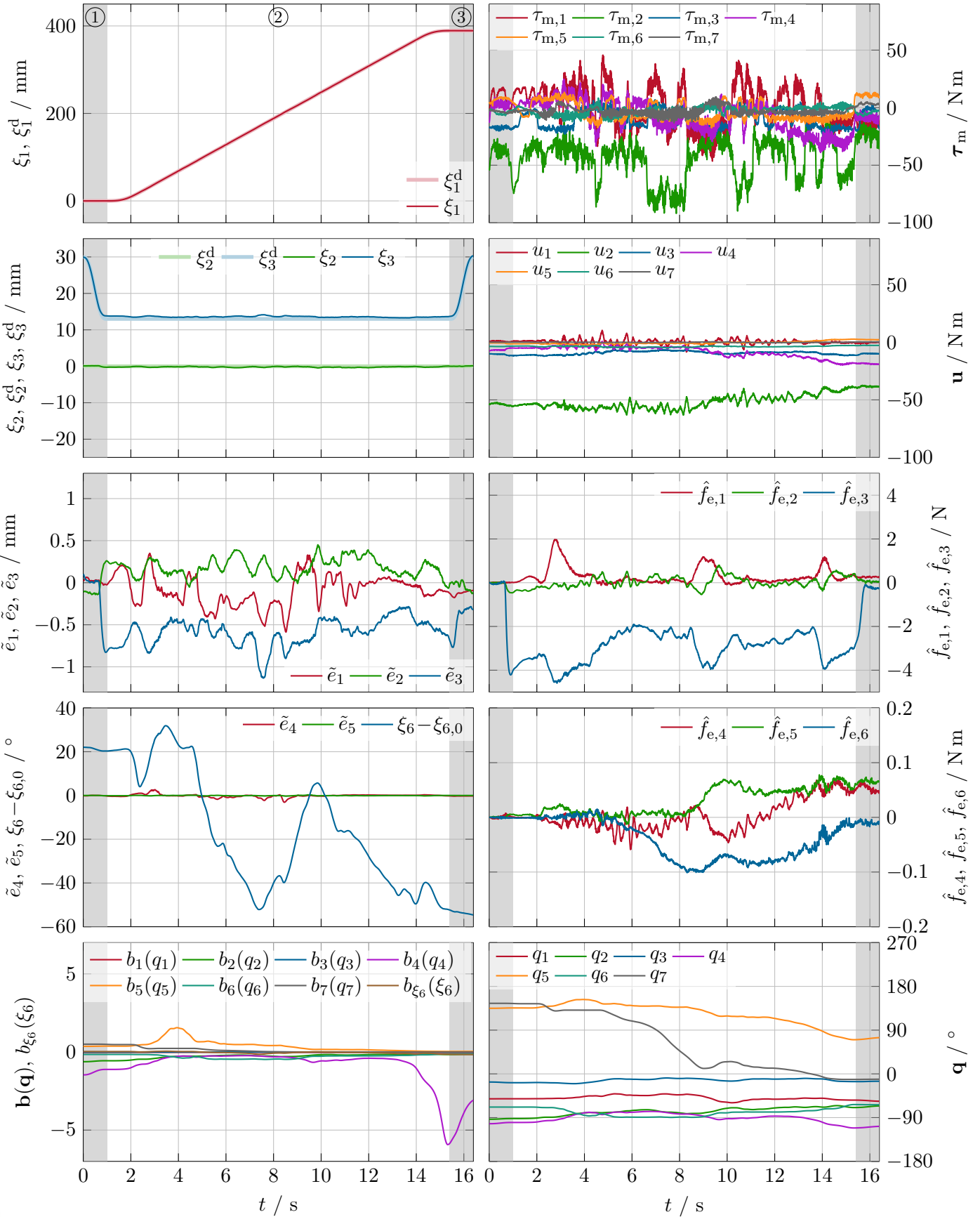


Figure 5.15: Experimental results of the tape application process of a straight tape. ① Contact establishment, ② Compliance-based tape application, ③ Contact release.

ing a \mathcal{C}^2 -trajectory from $\xi_3 = 30$ mm to $\xi_3 = 14$ mm, the target 3D object approaches the draping roll and comes into contact. Recalling the draping roll radius $r_r = 17.5$ mm and that the origin of the TCP frame \mathcal{T} lies on the draping roll axis, the final position $\xi_3 = 14$ mm implies that the target 3D object pushes 3.5 mm into the compliant layer of the draping roll. In combination with the impedance controller and its parameters, this results in the surface normal contact force $\hat{f}_{e,3}$ of approximately 4 N, while the other forces and torques remain close to zero. Moreover, the control errors $\tilde{\mathbf{e}}$ are also below 0.1 mm for positions and 0.2° for the orientation, while the redundant axis angle starts at approximately 22° . This non-zero redundant axis angle is the result of the optimization process of the initial robot configuration in Section 5.4.3 “Optimal Initial Robot Pose”. Note that the control parameters in Table A.4 are chosen such that the redundant axis ξ_6 is influenced by a restoring force term k_6^d and a damping term d_5^d . Thus, this angle is adjusted automatically using the nullspace controller, which damps the motion in the redundant tool axis and takes into account the respective joint and axis limits.

- ② *Compliance-based tape application:* In the second phase, the tape application is performed using the surface-based path following controller (3.86) and (5.4) with the nullspace controller from Section 5.4.2 “Nullspace Controller”. In the reduced path coordinates $\tilde{\mathbf{y}}$, the contact point moves from $\xi_1 = 0$ mm to $\xi_1 = 392$ mm with a maximum velocity of $\dot{\xi}_1 = 30$ mm/s using a \mathcal{C}^2 -trajectory. While the control errors \tilde{e}_1 and \tilde{e}_2 for the geodesic direction ξ_1 and the lateral direction ξ_2 stay below 0.6 mm, the controller adjusts the position ξ_3 along the surface normal direction according to the impedance model. Thus, the control strategy is able to comply with uncertainties related to the target 3D object and with the position errors of the robot manipulator. Throughout the process, the surface normal force $\hat{f}_{e,3}$ remains the dominant component. While the estimated surface tangent forces $\hat{f}_{e,1}$ and $\hat{f}_{e,2}$ are mostly below 1 N, the torques $\hat{f}_{e,4}$, $\hat{f}_{e,5}$ and $\hat{f}_{e,6}$ stay well below 100 mN m. Moreover, the orientation is tracked with small control errors \tilde{e}_4 and \tilde{e}_5 of less than 3° .

The angle $\xi_6 - \xi_{6,0}$ changes significantly in the range from -55° to 32° and, thus, the robot motion clearly exploits the available single-axis tool redundancy of the draping roll. Simultaneously, the barrier functions $\mathbf{b}(\mathbf{q})$ and $b_{\xi_6}(\xi_6)$ guard the joint limits of the robot q_i and \bar{q}_i , $i = 1, \dots, 7$, and the axis limits $\underline{\xi}_6$ and $\bar{\xi}_6$ of the redundant draping roll axis, respectively. At $t = 5$ s, q_5 approaches the upper joint limit of $\bar{q}_5 = 170^\circ$ and $b_5(q_5)$ becomes active, which initiates a nullspace motion in the coordinate ξ_6 towards $\xi_6 = 0$ in order to avoid this joint limit. Similarly, $b_4(q_4)$ intervenes slightly at $t = 10.7$ s and more strongly at $t = 16.3$ s due to the lower joint limit $\underline{q}_4 = -120^\circ$ of q_4 , which leads to a reduction of ξ_6 to prevent approaching the joint limit. The time evolution of \mathbf{q} shows that the tape application process for the straight tape is mostly performed using axes q_5 and q_7 , while the other axes only exhibit little motion.

The top right graphs in Fig. 5.15 also display the controller torques \mathbf{u} of (3.60) and the motor torques $\boldsymbol{\tau}_m$ introduced in (2.23) with the additional friction compensation $\boldsymbol{\tau}_f$. The difference between $\boldsymbol{\tau}_m$ and \mathbf{u} shows the presence of significant friction and elasticity in the drive train of the robot joints.

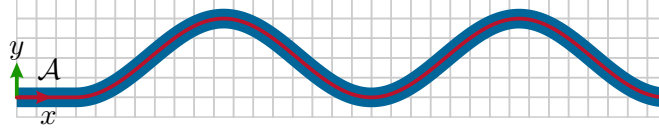


Figure 5.16: Tape “back” (see Table 5.3) and tape application path (red) for the experimental results shown in Fig. 5.17.

- ③ *Contact release:* The contact between the draping roll and the target 3D object is released at $t = 16.5$ s by moving the target 3D object from $\xi_3 = 14$ mm to $\xi_3 = 30$ mm again. Note that after release, minor estimated torques $\hat{f}_{e,4}$, $\hat{f}_{e,5}$, and $\hat{f}_{e,6}$ remain due to the imperfect compensation of the payload mass.

5.6.2 Curved Tape

In this section, the application of the curved tape “back” (see Table 5.3), depicted in the planar coordinate system \mathcal{A} in Fig. 5.16, is described. The measurement signals for the tape application process are displayed in Fig. 5.17. The individual graphs are arranged in the same way as in the previous subsection and are subdivided into three phases ①-③:

- ① *Contact establishment:* Analogously to the previous experiment, the contact between the target 3D object and the draping roll is established by moving the target 3D object in the reduced coordinates $\tilde{\mathbf{y}}$ from $\xi_3 = 30$ mm to $\xi_3 = 14$ mm. This pushes the target 3D object 3.5 mm into the compliant draping roll. The surface normal force $\hat{f}_{e,3}$ is approximately 3 N during the first contact. In this experiment, the coordinate of the redundant axis ξ_6 has an initial value of $\xi_{6,0} = 40^\circ$, which was found as the optimal initial pose for the robot.
- ② *Compliance-based tape application:* The tape application process is performed by moving the geodesic coordinate from $\xi_1 = 0$ mm to $\xi_1 = 325$ mm with a velocity of $\dot{\xi}_1 = 30$ mm/s. Simultaneously, the lateral motion along the draping roll axis is given by $\xi_2^d = -\pi_1(p)$, which correctly takes into account the lateral movement of the contact point, see Section 3.2.6 “Curved Paths” and Section 5.4.2 “Task Space Controller”. The geometric relations are also illustrated for curved paths in Fig. 3.3, cf. Fig. 5.5, and are applied to the tape depicted in Fig. 5.16.

The position trajectory in the surface-based coordinates $\tilde{\mathbf{y}}$ is followed with low control errors \tilde{e}_1 and \tilde{e}_2 for ξ_1 and ξ_2 below 1.2 mm. The position along the surface normal vector ξ_3 is adjusted by the controller according to the impedance model and slightly larger control errors \tilde{e}_3 appear. Throughout the tape application process, the orientation errors \tilde{e}_4 and \tilde{e}_5 remain below 0.8° . While the draping roll is in contact with the target 3D object, the surface normal force $\hat{f}_{e,3}$ remains dominant. Simultaneously, $\hat{f}_{e,1}$ and $\hat{f}_{e,2}$ stay mostly below 1 N and the torques mostly below 100 mN m.

For this experiment, the nullspace controller utilizes the angle of the redundant axis $\xi_6 - \xi_{6,0}$ in a large range from -74° to 40° . An automatic adjustment of the angle ξ_6 occurs at $t = 2.5$ s, as the robot joint q_6 approaches the respective upper joint limit $\bar{q}_6 = 120^\circ$. Additionally at $t = 7.2$ s, the barrier function

5 Application of Curved Tapes on 3D Objects

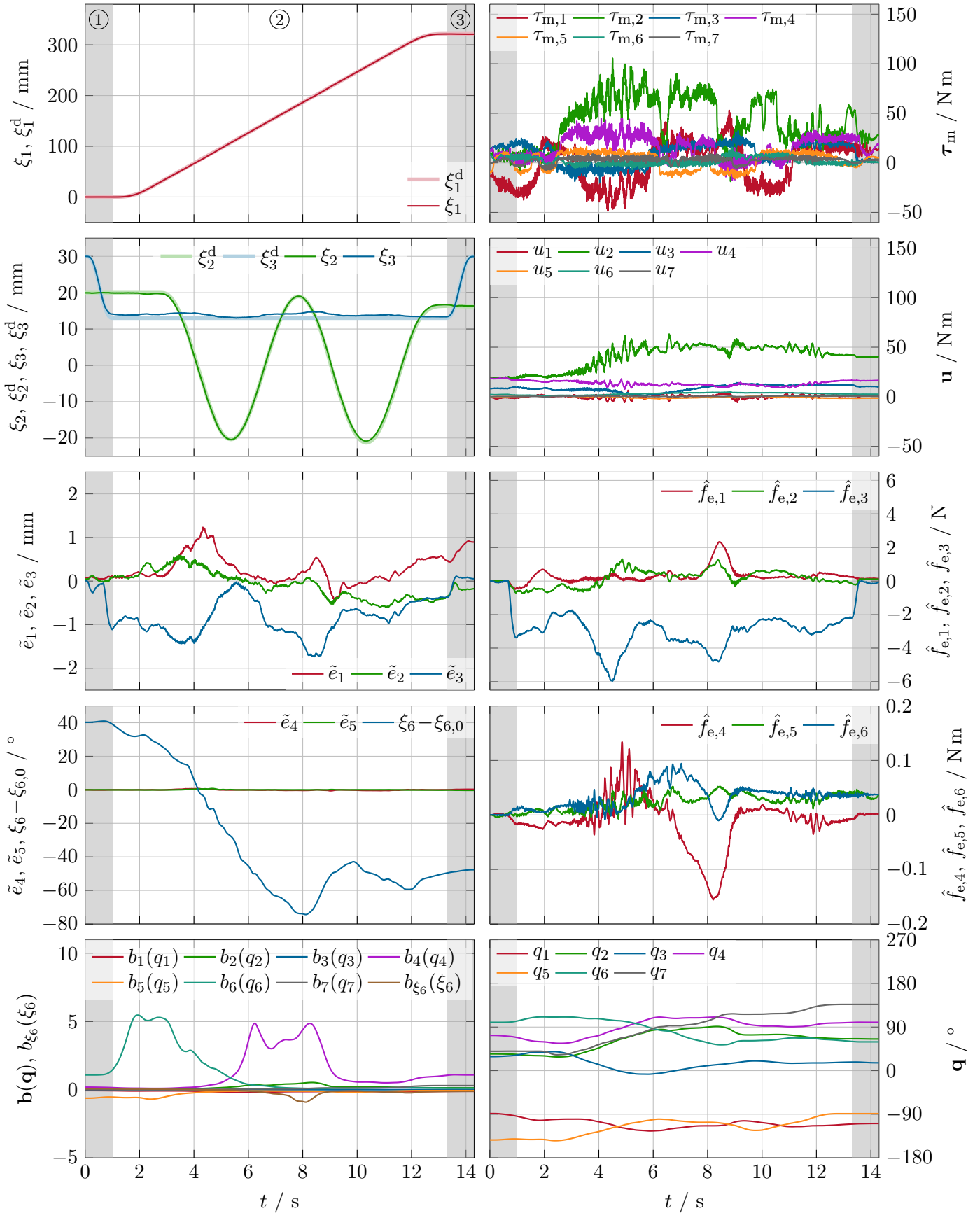


Figure 5.17: Experimental results of the tape application process of a curved tape. ① Contact establishment, ② Compliance-based tape application, ③ Contact release.

$b_4(\mathbf{q})$ causes a nullspace motion leading to a significant decrease of the angle ξ_6 , which prevents reaching the upper joint limit $\bar{q}_4 = 120^\circ$. Afterwards at $t = 9$ s, the redundant axis ξ_6 comes close to its lower axis limit of $\underline{\xi}_6 = -90^\circ$. This gives rise to additional torques in the nullspace $\boldsymbol{\tau}_n$, opposing the effects of $b_4(\mathbf{q})$. As a result, the robot motion remains close to $\xi_6 = -50^\circ$.

- ③ *Contact release:* The surface contact with the draping roll is released by moving the target 3D object away from the draping roll, i.e. in surface-based coordinates the robot moves from $\xi_3 = 14$ mm to $\xi_3 = 30$ mm. While the contact forces $\hat{f}_{e,1}$, $\hat{f}_{e,2}$, and $\hat{f}_{e,3}$ become close to zero, small residual torques $\hat{f}_{e,5}$ and $\hat{f}_{e,6}$ remain due to the imperfect contact force estimation.

5.6.3 Discussion

The experiments shown and described in the two previous sections demonstrate the feasibility of the proposed approach for the application of (curved) pre-cut tapes on freeform 3D surfaces. Surface-based path following control systematically generates the complex robot motion to appropriately perform the draping process by providing intuitive trajectories in the surface-based path coordinates. The contact forces and torques are estimated with respect to the parallel contact frame $\mathcal{C}_p(p)$ and, thus, have a clear physical meaning in the contact point of the surface. Throughout the tape application processes, the normal force $\hat{f}_{e,3}$ remained the main interaction force between the draping roll and the target 3D object. The robot motion systematically incorporates the single-axis tool redundancy of the draping roll, which provides additional flexibility for the tape application process and is used to avoid joint limits. Hence, the experiments show that the proposed method is capable of applying long tapes on surfaces with high curvature.



Die approbierte gedruckte Originalversion dieser Dissertation ist an der TU Wien Bibliothek verfügbar.
The approved original version of this doctoral thesis is available in print at TU Wien Bibliothek.

6

Conclusions and Outlook

In this thesis, a novel control concept to traverse known freeform 3D surfaces with robotic tools was developed. To this end, surface-based path following control was derived, which is the main contribution of this work. This control concept incorporates a coordinate transformation which takes into account the distinct normal vector of the underlying surface and the tangent vector of the associated path. In order to provide high flexibility and versatility, kinematic redundancies of the robot tools as well as kinematic constraints of the industrial processes are considered systematically. In this way, the proposed control approach is applicable to different industrial processes to be performed on freeform 3D surfaces, e. g., polishing, cutting and draping. The feasibility of the proposed control approach was experimentally demonstrated with the application of pre-cut tapes to freeform 3D surfaces.

Surface-based path following control was presented as a modular and versatile control concept. The schematic drawing in Fig. 6.1 illustrates the modular structure as an overview. The main building block of the control concept is the coordinate transformation for the surface-based coordinates, introduced in Section 3.3, which was derived for the natural contact frame in Section 3.3.1 and the parallel contact frame in Section 3.3.2. If the robotic tool exhibits a single-axis tool redundancy, as presented in Section 3.6.1, this can be incorporated into the coordinate transformation. Thus, the coordinate of the redundant axis is moved to the nullspace. Using the feedback linearization from Section 3.4 and the hierarchical nullspace controller from Section 3.6, the task space controller and the nullspace controller can act independently on the robotic system in an intuitive way. Furthermore, the contact force estimation derived in Section 5.5.6 provides an estimate of the external forces in surface-based coordinates, which allows a clear physical interpretation of the interaction forces. In Section 3.5, different task space controllers were formulated in the surface-based coordinates, i. e., impedance control, admittance control, compliance control, and force control. The path progress is an additional degree of freedom in path following control. Four different modes of operation were proposed in Sec-

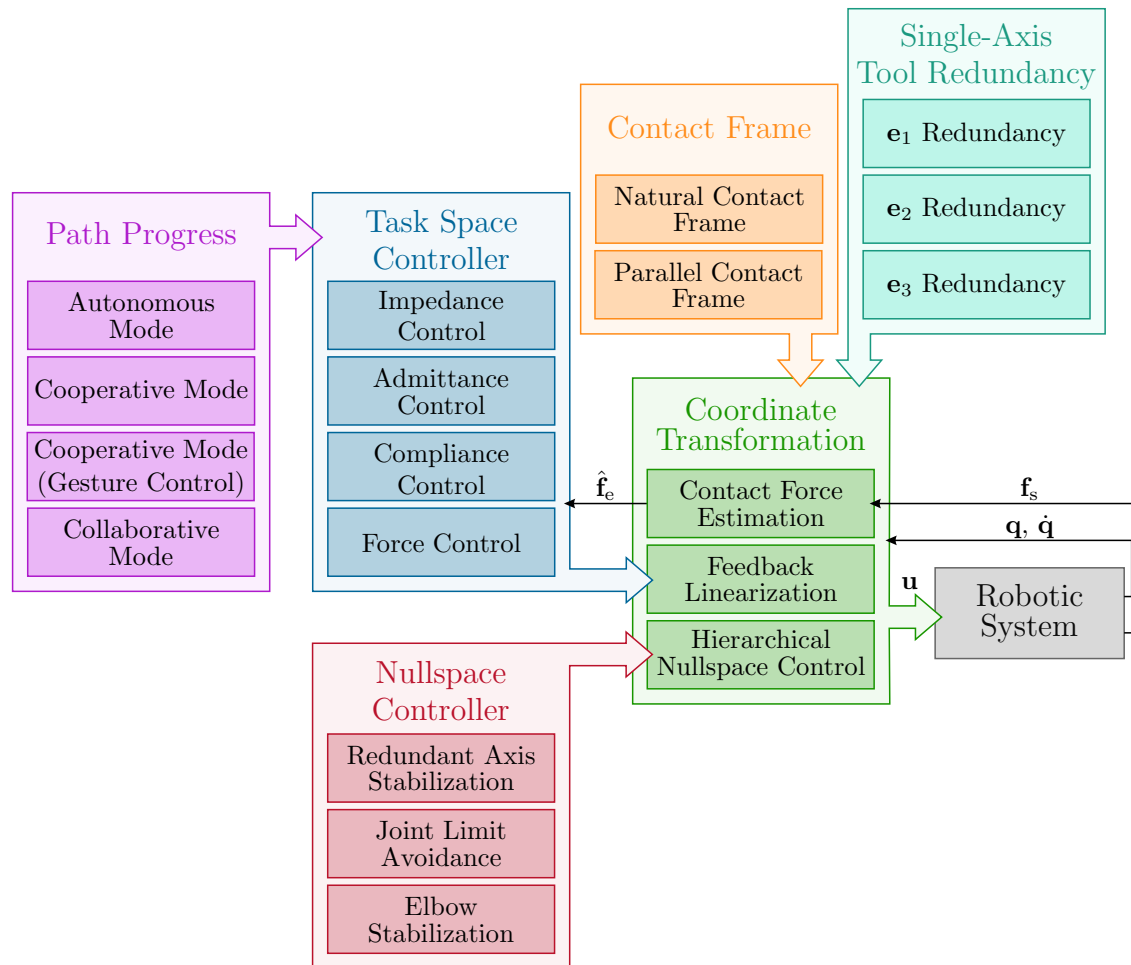


Figure 6.1: Modular structure of the surface-based path following control concept.

tion 3.7 with an emphasis on physical human-robot interaction (pHRI), i. e., the autonomous mode, two cooperative modes, and a collaborative mode. Finally, for nullspace control, the stabilization of the redundant axis, joint limit avoidance, and elbow stabilization were presented in Section 3.6, which act in different hierarchical levels on the robotic system.

6.1 Conclusions

Path following control separates the robot motion into a geometric path in task space and the time evolution of the path progress. In contrast to classical path following control, the control concept presented in Chapter 3 “Surface-Based Path Following Control” systematically takes into account the surface normal vector of an underlying freeform 3D surface and the path tangent vector of the corresponding surface-based path. Two different so-called contact frames were proposed and are chosen to comply with the application at hand: The natural contact frame is used for tasks where the tool orientation follows the path tangent, e. g. sewing or cutting. If turns of the tool around the surface normal vector have to be prevented, such as for draping applications, the parallel contact frame is utilized. Each contact frame also has its corresponding projection operator.

A coordinate transformation to transform a robotic system into surface-based path coordinates was formulated. Feedback linearization is applied to the robotic system, which results in a new system dynamics with linear input/output behavior. This allows to formulate standard controllers in the new surface-based path coordinates. Impedance control, admittance control, and force control were presented, which can also be combined to a hybrid controller. Four different modes for the time evolution of the path parameter were presented with an emphasis on pHRI applications: an autonomous mode for continuous automatic processes, two cooperative modes, which allow to stop the robot motion by human intervention, and a collaborative mode, which enables the human to guide the robot tool along the surface-based path.

In this work, industrial processes on freeform 3D surfaces are described in terms of kinematic constraints, i. e. forbidden rotations around specific tool axes, and kinematic redundancies, i. e., axes around which the tool is free to rotate. The draping process of pre-cut tapes on freeform 3D surfaces was shown to underlie kinematic constraints, i. e., the draping roll must not rotate around the surface normal vector in order to prevent wrinkles, and to provide a kinematic redundancy, which allows for free rotation around the draping roll axis to a large extent. These so-called single-axis tool redundancies are systematically incorporated into the surface-based path following control concept by choosing the proper minimal representation for the orientation and projecting the path-based system output to a reduced 5-dimensional output. In this way, the task space coordinate for the redundant tool axis is shifted to the nullspace, where it is stabilized using a hierarchical nullspace controller.

The aim of Chapter 4 “[Concept Study on Tape Application](#)” was to find a suitable concept for the fast and versatile application of pre-cut tapes to freeform 3D surfaces. A general analysis of this industrial process was concerned with the robot kinematics and robot employment as well as with the individual process steps *contouring* and *application*. This analysis was used to structure the concept study and to give a broad overview of commercial solutions and approaches published in the literature. Ten distinct concepts were presented and qualitatively evaluated in terms of accuracy, speed, flexibility, capability to impose defined normal and tension forces to the applied material, complexity and risk of the design. The two best approaches of this concept study, i. e. #5 “[Stationary tape dispenser with liner](#)” and #6 “[Stationary tape dispenser with conveyor belt](#)”, use a stationary application tool with material supply, while the target 3D object is moved by a robot. Due to the similarity of these two solutions, a single simplified tape application tool, comprising a passive draping roll and a feeding plate, was designed.

In Chapter 5 “[Application of Curved Tapes on 3D Objects](#)”, the surface-based path following control concept from Chapter 3 is utilized for the industrial process introduced in Chapter 4, i. e., the application of (curved) pre-cut adhesive tapes on freeform 3D surfaces. To perform the tape application, the deformable material is fed from a stationary feeding plate using a draping roll and the target 3D object is moved appropriately by a robot to perform a draping motion. The kinematic constraints of the draping process were met by utilizing the parallel contact frame. The draping roll axis was identified as a redundant tool axis. This redundancy was used to improve the process flexibility and to take into account the joint limits of

the robot. The robot/tool position was determined as a solution to an optimization problem using a direct search method. Also, the optimal initial robot pose for each tape application motion was found by minimizing a suitable cost function. For practical implementation, a time-discrete formulation of the control algorithm presented in Chapter 3 “[Surface-Based Path Following Control](#)” and a spatial discretization of the target 3D object was performed. The feasibility of the proposed control approach was experimentally shown using the concept from Chapter 4 with a custom-designed tape application tool and a 3D-printed target object. Seven straight and curved tapes with a geodesic length of 192 mm to 442 mm were applied to the target 3D object with application speeds of up to 30 mm/s.

The surface-based path following control concept presented in this work was formulated in a modular and generalized way. Thus, the methods, algorithms, and solutions can be applied to a wide range of industrial processes with different kinematic and dynamic requirements to be met on the freeform 3D surfaces.

6.2 Outlook

Workpiece Path Planning

With the industrial process presented in Chapter 5 “[Application of Curved Tapes on 3D Objects](#)”, a large number of pre-cut adhesive tapes can be applied to a target 3D object. However, the optimization algorithm proposed in Section 5.4.3 “[Optimal Initial Robot Pose](#)” only considers the application of single tapes and, thus, the overall process for all tapes is not optimized.

For non-overlapping adhesive tapes, the order of the individual tape application motions can be further optimized such that a minimal overall process time is achieved. Thus, path planning for a complete workpiece can be interpreted as a traveling salesman problem (TSP) [132]. In this context, each tape represents a vertex in a graph and the edges between the vertices represent the traveling moves, i. e., the collision-free robot motions from the end of one tape to the initial pose of the next tape. For each tape, a large number of initial poses are feasible and, thus, each vertex in the TSP graph can be reached via a large number of edges. A cost value representing the transition time is assigned to each traveling move. The solution of the TSP then yields the time-optimal order of the tape application motions and the optimal initial robot pose for each individual tape.

Increase Technology Readiness Level

The technology readiness level (TRL) estimates the maturity of a technology [133]. The demonstrations shown in Chapter 5 “[Application of Curved Tapes on 3D Objects](#)” represent a proof-of-concept of the proposed method for the application of pre-cut tapes to small- and medium-sized target 3D objects. However, the contouring and the feeding mechanism have not been considered in this work and several manual process steps are necessary for the proposed workflow, i. e. preparing the tape on the feeding plate and mounting the workpiece on the robot end-effector. Thus, the experimental setup is considered as TRL 3 according to [133]. In order to integrate this process into an industrial application, TRL 6 or higher is required,

Table 6.1: Industrial processes with associated kinematic constraints and redundancies.

Process	Kinematic constraint	Kinematic redundancy
Polishing		
Laser cutting	Tool axis inside tolerance cone of surface normal	Rotation around surface normal
Spray painting with circular nozzle		
Spray painting with non-circular nozzle	Tool axis aligned with surface normal, rotation around surface normal vector	(none)
Sewing		
Ultrasonic cutting	Tool orientation aligned with path tangent	Rotation around path tangent
Draping	Rotation around surface normal vector	Rotation around tool axis
Tape application		
Glueing	Tool axis inside tolerance cone of surface normal	Rotation around all axes
Welding		

i. e. a full prototype in the operational environment. Therefore, further steps have to be performed to develop a fully automated process chain which can be used in an industrial setting, including a contouring and a feeding mechanism. The surface-based path following control concept is advantageous for this implementation, as the path progress can be utilized to synchronize an automatic feeding mechanism with the draping motion.

Industrial Processes

Surface-based path following control was presented as a modular control concept to describe the robot motion with respect to a surface-based path and its underlying surface. In surface-based path coordinates, different standard controllers are applicable and kinematic constraints and redundancies can be systematically taken into account. Therefore, the proposed approach is useful for a number of industrial processes performed on freeform 3D surfaces. Table 6.1 lists some example processes with the associated kinematic constraints and redundancies, which constitute future use cases for the proposed method.



Die approbierte gedruckte Originalversion dieser Dissertation ist an der TU Wien Bibliothek verfügbar.
The approved original version of this doctoral thesis is available in print at TU Wien Bibliothek.

A

Parameters

A.1 Kinematic Parameters

Table A.1: Parameters of the kinematic model of the KUKA LBR iiwa 14 R820.

i	$d_{i,y}$ mm	$d_{i,z}$ mm	α_i rad
1	0	152.5	0
2	0	207.5	$-\frac{\pi}{2}$
3	-232.5	0	$\frac{\pi}{2}$
4	0	187.5	$\frac{\pi}{2}$
5	212.5	0	$-\frac{\pi}{2}$
6	0	187.5	$-\frac{\pi}{2}$
7	-79.6	0	$\frac{\pi}{2}$
8	-	72.4	-

A.2 Controller Parameters

Table A.2: Parameters for the torque controller (5.11) and the disturbance observer (5.10) in Section 5.5.1 “Robot Control”.

i	$K_{\tau,i}$	$D_{\tau,i}$	F_i
1	4	0.015	200
2	4	0.015	200
3	4	0.015	300
4	5	0.02	300
5	3	0.01	500
6	2.5	0.01	1000
7	2.5	0.01	1000

Table A.3: Barrier function parameters for Section 5.4.3 “Optimal Initial Robot Pose”.

i	\underline{b}_i	\bar{b}_i	\underline{q}_i °	\bar{q}_i °
1	2	2	-170	170
2	2	2	-120	120
3	2	2	-170	170
4	2	2	-120	120
5	2	2	-170	170
6	2	2	-120	120
7	2	2	-175	175

Table A.4: Controller and barrier function parameters for the dynamic optimization problem in Section 5.4.3 “Optimal Initial Robot Pose” and for the experiments in Section 5.6 “Experimental Results”.

Symbol	Value	Unit
\underline{b}_{ξ_6}	1	
\bar{b}_{ξ_6}	1	
$\underline{\xi}_6$	-90	°
$\bar{\xi}_6$	90	°
$\xi_{6,0}$	0	°
k_1^d, \dots, k_5^d	900	N/m
d_1^d, \dots, d_5^d	60	N s/m
k_6^d	1	N/m
d_6^d	2	N s/m
m_1^d, \dots, m_6^d	1	kg
\mathbf{K}_n	diag([1, 1, 1, 1, 1, 1, 1])	N/m
\mathbf{D}_n	diag([2, 2, 2, 2, 2, 2, 2])	N s/m

Bibliography

- [1] V. Villani, F. Pini, F. Leali, and C. Secchi, “Survey on human–robot collaboration in industrial settings: Safety, intuitive interfaces and applications,” *Mechatronics*, vol. 55, pp. 248–266, 2018.
- [2] Z. Pan, J. Polden, N. Larkin, S. Van Duin, and J. Norrish, “Recent Progress on Programming Methods for Industrial Robots,” in *Proceedings of the International Symposium on Robotics (ISR) and the German Conference on Robotics (ROBOTIK)*, Munich, Germany, 2010, pp. 619–626.
- [3] K. M. Muthiah, S. H. Huang, and S. Mahadevan, “Automating factory performance diagnostics using overall throughput effectiveness (OTE) metric,” *The International Journal of Advanced Manufacturing Technology*, vol. 36, no. 7–8, pp. 811–824, 2008.
- [4] C. Connolly, “Technology and applications of ABB RobotStudio,” *Industrial Robot*, vol. 36, no. 6, pp. 540–545, 2009.
- [5] A. Montaqim. (2015) Offline programming software for industrial robots from RoboDK offers hundreds of virtual industrial robots from top robotics companies. *Robotic and Automation News*. (2020, June 11). [Online]. Available: <https://roboticsandautomationnews.com/2015/07/14/offline-programming/540/>
- [6] International Federation of Robotics. Executive Summary World Robotics 2019 Industrial Robots. (2020, June 11). [Online]. Available: <https://ifr.org/downloads/press2018/ExecutiveSummaryWR2019IndustrialRobots.pdf>
- [7] J. N. Pires, T. Godinho, and P. Ferreira, “CAD interface for automatic robot welding programming,” *Industrial Robot*, vol. 31, no. 1, pp. 71–76, 2004.
- [8] T. Wagner, “Integrated robotic gluing system,” in *Proceedings of the International Symposium on Robotics (ISR) and the German Conference on Robotics (ROBOTIK)*, Munich, Germany, 2010, pp. 835–837.
- [9] D. H.-J. Lukaszewicz, C. Ward, and K. D. Potter, “The engineering aspects of automated prepreg layup: History, present and future,” *Composites Part B: Engineering*, vol. 43, no. 3, pp. 997–1009, 2012.
- [10] Y. Takeuchi, D. Ge, and N. Asakawa, “Automated Polishing Process with a Human-like Dexterous Robot,” in *Proceedings of the IEEE International Conference on Robotics and Automation (ICRA)*, Atlanta, Georgia, USA, 1993, pp. 950–956.
- [11] H. Chen, W. Sheng, N. Xi, M. Song, and Y. Chen, “Automated Robot Trajec-

Bibliography

- tory Planning for Spray Painting of Free-Form Surfaces in Automotive Manufacturing,” in *Proceedings of the IEEE International Conference on Robotics and Automation (ICRA)*, vol. 1, Washington, District of Columbia, USA, 2002, pp. 450–455.
- [12] G. Biegelbauer, M. Richtsfeld, W. Wohlkinger, M. Vincze, and M. Herkt, “Optical Seam Following for Automated Robot Sewing,” in *Proceedings of the IEEE International Conference on Robotics and Automation (ICRA)*, Rome, Italy, 2007, pp. 4758–4763.
- [13] S. Caro, C. Dumas, S. Garnier, and B. Furet, “Workpiece Placement Optimization for Machining Operations with a KUKA KR270-2 Robot,” in *Proceedings of the IEEE International Conference on Robotics and Automation (ICRA)*, Karlsruhe, Germany, 2013, pp. 2921–2926.
- [14] U. Schneider, J. R. D. Posada, and A. Verl, “Automatic Pose Optimization for Robotic Processes,” in *Proceedings of the IEEE International Conference on Robotics and Automation (ICRA)*, Seattle, Washington, USA, 2015, pp. 2054–2059.
- [15] J. N. Pires, *Industrial Robots Programming: Building Applications for the Factories of the Future*. New York: Springer Science & Business Media, 2007.
- [16] W. Van Loock, G. Pipeleers, M. Diehl, J. De Schutter, and J. Swevers, “Optimal Path Following for Differentially Flat Robotic Systems Through a Geometric Problem Formulation,” *IEEE Transactions on Robotics*, vol. 30, no. 4, pp. 980–985, 2014.
- [17] G.-C. Chiu and M. Tomizuka, “Contouring Control of Machine Tool Feed Drive Systems: A Task Coordinate Frame Approach,” *IEEE Transactions on Control Systems Technology*, vol. 9, no. 1, pp. 130–139, 2001.
- [18] T. Faulwasser, T. Weber, P. Zometa, and R. Findeisen, “Implementation of Nonlinear Model Predictive Path-Following Control for an Industrial Robot,” *IEEE Transactions on Control Systems Technology*, vol. 25, no. 4, pp. 1505–1511, 2017.
- [19] C. Nielsen, C. Fulford, and M. Maggiore, “Path Following Using Transverse Feedback Linearization: Application to a Maglev Positioning System,” in *Proceedings of the American Control Conference (ACC)*, St. Louis, Missouri, USA, 2009, pp. 3045–3050.
- [20] A. Hladio, C. Nielsen, and D. Wang, “Path Following for a Class of Mechanical Systems,” *IEEE Transactions on Control Systems Technology*, vol. 21, no. 6, pp. 2380–2390, 2013.
- [21] V. A. Toponogov, *Differential Geometry of Curves and Surfaces*. Boston: Birkhäuser, 2006.
- [22] R. J. Gill, D. Kulić, and C. Nielsen, “Spline Path Following for Redundant Mechanical Systems,” *IEEE Transactions on Robotics*, vol. 31, no. 6, pp. 1378–1392, 2015.
- [23] R. L. Bishop, “There is More than One Way to Frame a Curve,” *The American*

- Mathematical Monthly*, vol. 82, no. 3, pp. 246–251, 1975.
- [24] B. Bischof, T. Glück, and A. Kugi, “Combined Path Following and Compliance Control for Fully Actuated Rigid Body Systems in 3-D Space,” *IEEE Transactions on Control Systems Technology*, vol. 25, no. 5, pp. 1750–1760, 2017.
- [25] I. Kaminer, A. Pascoal, E. Xargay, N. Hovakimyan, C. Cao, and V. Dobrokhodov, “Path Following for Unmanned Aerial Vehicles Using \mathcal{L}_1 Adaptive Augmentation of Commercial Autopilots,” *Journal of Guidance, Control, and Dynamics*, vol. 33, no. 2, pp. 550–564, 2010.
- [26] T. Oliveira, P. Encarnação, and A. P. Aguiar, “Moving Path Following for Autonomous Robotic Vehicles,” in *Proceedings of the European Control Conference (ECC)*, Zurich, Switzerland, 2013, pp. 3320–3325.
- [27] B. Bischof, T. Glück, M. Böck, and A. Kugi, “A Path/Surface Following Control Approach to Generate Virtual Fixtures,” *IEEE Transactions on Robotics*, vol. 34, no. 6, pp. 1577–1592, 2018.
- [28] M. Saadat and P. Nan, “Industrial applications of automatic manipulation of flexible materials,” *Industrial Robot*, vol. 29, no. 5, pp. 434–442, 2002.
- [29] P. Taylor and G. Taylor, “Progress Towards Automated Garment Manufacture,” in *Sensory Robotics for the Handling of Limp Materials*, ser. NATO ASI Series (Series F: Computer and Systems Sciences), P. Taylor, Ed. Berlin Heidelberg: Springer, 1990, vol. 64, pp. 97–109.
- [30] P. Boisse, Ed., *Advances in Composites Manufacturing and Process Design*, ser. Composites Science and Engineering. Cambridge: Woodhead Publishing, 2015, no. 56.
- [31] S. Jadhav, G. Sharma, A. Daberao, and S. Gulhane, “Improving Productivity of Garment Industry with Time Study,” *International Journal on Textile Engineering and Processes*, vol. 3, no. 3, pp. 1–6, 2017.
- [32] M. Marcelo, G. Avila, M. Cruz, B. Prado, and M. Navarro, “Process Improvement and Utilization of Machines in the Production Area of a Shoe Manufacturing Company,” in *Proceedings of the IEEE International Conference on Industrial Engineering and Engineering Management (IEEM)*, Bali, Indonesia, 2016, pp. 701–705.
- [33] R. Lässig, M. Eisenhut, A. Mathias, R. T. Schulte, F. Peters, T. Kühmann, T. Waldmann, and W. Begemann, “Series production of high-strength composites: Perspectives for the German engineering industry,” Roland Berger Strategy Consultants, Tech. Rep., 2012, (2020, June 11). [Online]. Available: https://www.vdma.org/documents/266675/2307595/RBSC_VDMA_Composite_Studie_FINAL_en.pdf
- [34] H. B. Olsen and J. J. Craig, “Automated composite tape lay-up using robotic devices,” in *Proceedings of the IEEE International Conference on Robotics and Automation (ICRA)*, Atlanta, Georgia, USA, 1993, pp. 291–297.
- [35] R. Buckingham and G. Newell, “Automating the manufacture of composite broadgoods,” *Composites Part A: Applied Science and Manufacturing*, vol.

Bibliography

- 27A, no. 3, pp. 191–200, 1996.
- [36] A. Björnsson, M. Jonsson, and K. Johansen, “Automated material handling in composite manufacturing using pick-and-place systems – a review,” *Robotics and Computer-Integrated Manufacturing*, vol. 51, pp. 222–229, 2018.
- [37] S. Lankalapalli and J. W. Eischen, “Optimal Pick-up Locations for Transport and Handling of Limp Materials: Part I: One-Dimensional Strips,” *Textile Research Journal*, vol. 73, no. 9, pp. 787–796, 2003.
- [38] —, “Optimal Pick-up Locations for Transport and Handling of Limp Materials: Part II: Two-Dimensional Parts,” *Textile Research Journal*, vol. 73, no. 10, pp. 867–874, 2003.
- [39] M. Elkington, D. Bloom, C. Ward, A. Chatzimichali, and K. Potter, “Hand layup: understanding the manual process,” *Advanced Manufacturing: Polymer & Composites Science*, vol. 1, no. 3, pp. 138–151, 2015.
- [40] M. Elkington, C. Ward, and K. D. Potter, “Automated Layup of Sheet Prepregs on Complex Moulds,” in *Proceedings of the International Society for the Advancement of Material and Process Engineering (SAMPE) Technical Conference*, Long Beach, California, USA, 2016.
- [41] M. Elkington, “Automated Composite Draping: A Review,” in *Proceedings of the International Society for the Advancement of Material and Process Engineering (SAMPE) Technical Conference*, Seattle, Washington, USA, 2017.
- [42] G. Fantoni, M. Santochi, G. Dini, K. Tracht, B. Scholz-Reiter, J. Fleischer, T. K. Lien, G. Seliger, G. Reinhart, J. Franke, H. N. Hansen, and A. Verl, “Grasping devices and methods in automated production processes,” *CIRP Annals - Manufacturing Technology*, vol. 63, no. 2, pp. 679–701, 2014.
- [43] C. Löchte, H. Kunz, R. Schnurr, F. Dietrich, A. Raatz, K. Dilger, and K. Dröder, “Form-Flexible Handling Technology for Automated Preforming,” in *Proceedings of International Conference on Composite Materials (ICCM)*, Montreal, Canada, 2013, pp. 2130–2141.
- [44] G. Reinhart and G. Straßer, “Flexible gripping technology for the automated handling of limp technical textiles in composites industry,” *Production Engineering*, vol. 5, no. 3, pp. 301–306, 2011.
- [45] G. Straßer, “Greiftechnologie für die automatisierte Handhabung von technischen Textilien in der Faserverbundfertigung,” in *Forschungsberichte IWB*, G. Reinhart and M. Zäh, Eds. Munich: Herbert Utz Verlag, 2012, vol. 256.
- [46] M. Szceny, F. Heieck, S. Carosella, P. Middendorf, H. Sehrschön, and M. Schneiderbauer, “The advanced ply placement process – an innovative direct 3D placement technology for plies and tapes,” *Advanced Manufacturing: Polymer & Composites Science*, vol. 3, no. 1, pp. 2–9, 2017.
- [47] S. Flixeder, T. Glück, and A. Kugi, “Force-based cooperative handling and lay-up of deformable materials: Mechatronic design, modeling, and control of a demonstrator,” *Mechatronics*, vol. 47, pp. 246–261, 2017.
- [48] Cevotec GmbH. SAMBA PRO. (2020, June 11). [Online]. Available:

<https://www.cevotec.com/>

- [49] C. Ward, V. Bhatnagar, and K. Potter, “Developing an Automated System for the Removal of Protective Films from Pre-Preg Material, to Remove a Manufacturing Bottleneck in Terms of Pick and Place Automation,” in *Proceedings of the Society for the Advancement of Material and Process Engineering (SAMPE) Europe Technical Conference (SETEC)*, vol. 13, Wuppertal, Germany, 2013.
- [50] Fives Metal Cutting | Composites. FOREST-LINÉ ATLAS, ACCESS. (2020, June 11). [Online]. Available: <https://metal-cutting-composites.fivesgroup.com/>
- [51] R. Paton, “Forming technology for thermoset composites,” in *Composites Forming Technologies*, A. C. Long, Ed. Cambridge: Woodhead Publishing, 2007, pp. 239–255.
- [52] Q. Yuan, T. S. Lembono, Y. Zou, and I.-M. Chen, “Automatic Robot Taping: Auto-Path Planning and Manipulation,” in *Proceedings of the IEEE International Conference on Cybernetics and Intelligent Systems (CIS) and IEEE Conference on Robotics, Automation and Mechatronics (RAM)*, Angkor Wat, Cambodia, 2015, pp. 175–180.
- [53] Q. Yuan, T. S. Lembono, I.-M. Chen, S. N. Landén, and V. Malmgren, “Automatic Robot Taping with Force Feedback,” in *Proceedings of the IEEE International Conference on Robotics and Automation (ICRA)*, Singapore, 2017, pp. 1821–1826.
- [54] C. Brecher, M. Emonts, B. Ozolin, and R. Schares, “Handling of preforms and prepregs for mass production of composites,” in *Proceedings of the International Conference on Composite Materials (ICCM)*, vol. 28, Montreal, Canada, 2013.
- [55] KUKA Roboter GmbH, “LBR iiwa Betriebsanleitung,” Manual, 2015.
- [56] B. Siciliano, L. Sciavicco, L. Villani, and G. Oriolo, *Robotics: Modelling, Planning and Control*. London: Springer, 2010.
- [57] M. Shimizu, H. Kakuya, W.-K. Yoon, K. Kitagaki, and K. Kosuge, “Analytical Inverse Kinematic Computation for 7-DOF Redundant Manipulators With Joint Limits and Its Application to Redundancy Resolution,” *IEEE Transactions on Robotics*, vol. 24, no. 5, pp. 1131–1142, 2008.
- [58] M. Pfurner, “Closed form inverse kinematics solution for a redundant anthropomorphic robot arm,” *Computer Aided Geometric Design*, vol. 47, pp. 163–171, 2016.
- [59] C. Hartl-Nesic and M. Meiringer, “Computational Performance of the Forward and Inverse Kinematics of an Anthropomorphic Robot Arm,” in *Proceedings of the Austrian Robotics Workshop (ARW) & Austrian Association for Pattern Recognition (OAGM) Workshop*, Steyr, Austria, 2019, pp. 115–116.
- [60] C. Ott, *Cartesian Impedance Control of Redundant and Flexible-Joint Robots*. Berlin Heidelberg: Springer, 2008.

Bibliography

- [61] A. De Luca and W. J. Book, “Robots with Flexible Elements,” in *Springer Handbook of Robotics*, B. Siciliano and O. Khatib, Eds. Berlin Heidelberg: Springer, 2016, pp. 287–319.
- [62] M. W. Spong, “Modeling and Control of Elastic Joint Robots,” *Journal of Dynamic Systems, Measurement, and Control*, vol. 109, no. 4, pp. 310–318, 1987.
- [63] A. Dolgui and A. Pashkevich, “Manipulator motion planning for high-speed robotic laser cutting,” *International Journal of Production Research*, vol. 47, no. 20, pp. 5691–5715, 2009.
- [64] M. P. Do Carmo, *Differential Geometry of Curves and Surfaces*, 2nd ed. Mineola: Dover Publications, 2016.
- [65] S. Sternberg, *Lectures on Differential Geometry*. Englewood Cliffs: Prentice Hall, 1964.
- [66] L. Perko, *Differential Equations and Dynamical Systems*, 3rd ed., ser. Texts in Applied Mathematics, J. Marsden, L. Sirovich, and M. Golubitsky, Eds. New York: Springer, 2001, vol. 7.
- [67] H.-C. Song, J.-H. Yong, Y.-J. Yang, and X.-M. Liu, “Algorithm for orthogonal projection of parametric curves onto B-spline surfaces,” *Computer-Aided Design*, vol. 43, no. 4, pp. 381–393, 2011.
- [68] J. Xu, X. Zhang, S. Wang, and J. Wu, “Tool path generation for pattern sculpting on free-form surfaces,” *The International Journal of Advanced Manufacturing Technology*, vol. 67, no. 9-12, pp. 2469–2476, 2013.
- [69] L. Yan, Z. C. Chen, Y. Shi, and R. Mo, “An accurate approach to roller path generation for robotic fibre placement of free-form surface composites,” *Robotics and Computer-Integrated Manufacturing*, vol. 30, no. 3, pp. 277–286, 2014.
- [70] N. Hayashi, T. Tomizawa, T. Suehiro, and S. Kudoh, “Dual Arm Robot Fabric Wrapping Operation Using Target Lines,” in *Proceedings of the IEEE International Conference on Robotics and Biomimetics (ROBIO)*, Bali, Indonesia, 2014, pp. 2185–2190.
- [71] W. J. Rugh, “Linear System Theory,” in *Information and System Sciences Series*, 2nd ed., T. Kailath, Ed. Upper Saddle River: Prentice Hall, 1996.
- [72] C. Hartl-Nesic, B. Bischof, T. Glück, and A. Kugi, “Pfadfolgeregelung mit Konzepten für den Pfadfortschritt: Ein Assemblierungsszenario,” *at – Automatisierungstechnik*, vol. 68, no. 1, pp. 44–57, 2020.
- [73] A. O. Ignatyev, “Stability of a Linear Oscillator with Variable Parameters,” *Electronic Journal of Differential Equations*, vol. 1997, no. 17, pp. 1–6, 1997.
- [74] S. Chiaverini, B. Siciliano, and L. Villani, “A Survey of Robot Interaction Control Schemes with Experimental Comparison,” *IEEE Transactions on Mechatronics*, vol. 4, no. 3, pp. 273–285, 1999.
- [75] A. Dietrich, C. Ott, and A. Albu-Schäffer, “An Overview of Null Space Projections for Redundant, Torque Controlled Robots,” *The International Journal*

- of *Robotics Research*, vol. 34, no. 11, pp. 1385–1400, 2015.
- [76] S. Boyd and L. Vandenberghe, *Convex Optimization*. Cambridge: Cambridge University Press, 2004.
- [77] X. Xiang, C. Liu, L. Lapiere, and B. Jouvencel, “Synchronized path following control of multiple homogenous underactuated AUVs,” *Journal of Systems Science and Complexity*, vol. 25, no. 1, pp. 71–89, 2012.
- [78] B. Bischof, “Path and Surface Following Control for Industrial Robotic Applications,” in *Modellierung und Regelung komplexer dynamischer Systeme*, A. Kugi and K. Schlacher, Eds. Aachen: Shaker, 2020, vol. 47.
- [79] B. Bischof, T. Glück, M. Böck, and A. Kugi, “Path Following Control for Elastic Joint Robots,” *IFAC-PapersOnLine*, vol. 50, no. 1, pp. 4806–4811, 2017.
- [80] S. Flixeder, “Force-Based Cooperative Manipulation of Highly Deformable Materials,” in *Modellierung und Regelung komplexer dynamischer Systeme*, A. Kugi and K. Schlacher, Eds. Aachen: Shaker, 2017, vol. 36.
- [81] M. A. Krasnosel’skii and A. V. Pokrovskii, *Systems with Hysteresis*. Berlin Heidelberg: Springer, 1989.
- [82] Q. Yuan, I.-M. Chen, T. S. Lembono, S. N. Landén, and V. Malmgren, “Automatic robot taping system with compliant force control,” *The International Journal of Advanced Manufacturing Technology*, vol. 94, no. 9-12, pp. 4105–4113, 2018.
- [83] C. Hartl-Nesic, T. Glück, A. Kugi, T. Feix, and C. Dyckmans, “Method for Placing of Components,” US Patent 16/752,558, 2020.
- [84] H. Mattila, Ed., *Intelligent textiles and clothing*. Cambridge: Woodhead Publishing, 2006.
- [85] T. D. Ngo, A. Kashani, G. Imbalzano, K. T. Nguyen, and D. Hui, “Additive manufacturing (3D printing): A review of materials, methods, applications and challenges,” *Composites Part B: Engineering*, vol. 143, pp. 172–196, 2018.
- [86] B. Fischer, B. Horn, C. Bartelt, and Y. Blößl, “Method for an Automated Optimization of Fiber Patch Placement Layup Designs,” *International Journal of Composite Materials*, vol. 5, no. 2, pp. 37–46, 2015.
- [87] G. Gardiner, “Airbus A350 update: BRaF & FPP,” *High-Performance Composites*, vol. 20, no. 1, pp. 32–39, 2012, (2020, June 11). [Online]. Available: <https://www.compositesworld.com/articles/airbus-a350-update-braf-fpp>
- [88] I. Vilumsone-Nemes, *Industrial Cutting of Textile Materials*, 2nd ed. Duxford: Woodhead Publishing, 2018.
- [89] M. T. Kordi, *Entwicklung von Roboter-Endeffektoren zur automatisierten Herstellung textiler Preforms für Faserverbundbauteile*. Aachen: Shaker, 2009.
- [90] L. Lin, L. Yong, W. Liwei, and X. Jun, “PMAC-based Tracking Control System for 8-axis Automated Tape-laying Machine,” *Chinese Journal of Aeronautics*, vol. 22, no. 5, pp. 558–563, 2009.

Bibliography

- [91] Y. Grohmann, N. Stoffers, A. Kühn, and T. Mahrholz, “Development of the Direct Roving Placement Technology (DRP),” in *Proceedings of the European Conference on Composite Materials (ECCM)*, Munich, Germany, 2016.
- [92] J. Reiff-Stephan, “Greifer für biegeschlaffe Materialien,” *A&D Kompendium*, pp. 282–284, 2005.
- [93] Westmark Labels & Marking. Label Aire 3111 High Speed Air Blow. (2020, June 11). [Online]. Available: <https://www.westmarklm.com/>
- [94] cab Produkttechnik. Hermes+ Print and Apply System with Applicator 6114 (Air Jet Box). (2020, June 11). [Online]. Available: <https://www.cab.de/en/>
- [95] C. Brecher, C. Kukla, R. Schares, M. Emonts, and M. Haus, “Form-Adaptive Gripping System for Light-Weight Productions,” in *Proceedings of the International Conference on Composite Materials (ICCM)*, Copenhagen, Denmark, 2015.
- [96] C. Ehinger and G. Reinhart, “Robot-based automation system for the flexible preforming of single-layer cut-outs in composite industry,” *Production Engineering*, vol. 8, no. 5, pp. 559–565, 2014.
- [97] T. Gerngroß, “Projekt AZIMUT - Automatisierungslösungen für große Faserverbundbauteile in der Luftfahrt,” *Ingenieurspiegel*, pp. 72–74, 2015.
- [98] A. Björnsson, M. Jonsson, D. Eklund, J. E. Lindbäck, and M. Björkman, “Getting to grips with automated prepreg handling,” *Production Engineering*, vol. 11, no. 4-5, pp. 445–453, 2017.
- [99] Lohmann GmbH & Co. KG. Adhesive Devices Robotic Application. (2020, June 11). [Online]. Available: <https://www.lohmann-tapes.com/>
- [100] J. Scholliers and H. Van Brussel, “Computer-integrated filament winding: computer-integrated design, robotic filament winding and robotic quality control,” *Composites Manufacturing*, vol. 5, no. 1, pp. 15–23, 1994.
- [101] E. Brown, N. Rodenberg, J. Amend, A. Mozeika, E. Steltz, M. R. Zakin, H. Lipson, and H. M. Jaeger, “Universal robotic gripper based on the jamming of granular material,” *Proceedings of the National Academy of Sciences*, vol. 107, no. 44, pp. 18 809–18 814, 2010.
- [102] J. Brinker, M. Müller, J. Paris, M. Hüsing, and B. Corves, “Mechanism Design for Automated Handling and Multiaxial Draping of Reinforcing Textiles,” in *Proceedings of the ASME International Design Engineering Technical Conferences (IDETC) and Computers and Information in Engineering Conference (CIE)*, Charlotte, North Carolina, USA, 2016.
- [103] P. Zhao, B. Shirinzadeh, Y. Shi, S. Cheuk, and L. Clark, “Multi-pass layup process for thermoplastic composites using robotic fiber placement,” *Robotics and Computer-Integrated Manufacturing*, vol. 49, pp. 277–284, 2018.
- [104] C. A. Ehinger, “Automatisierte Montage von Faserverbund-Vorformlingen,” in *Forschungsberichte IWB*, G. Reinhart and M. Zäh, Eds. Munich: Herbert Utz Verlag, 2013, vol. 268.
- [105] A. Angerer, C. Ehinger, A. Hoffmann, W. Reif, G. Reinhart, and G. Strasser,

- “Automated Cutting and Handling of Carbon Fiber Fabrics in Aerospace Industries,” in *Proceedings of the IEEE International Conference on Automation Science and Engineering (CASE)*, Toronto, Canada, 2010, pp. 861–866.
- [106] S. Bayer and F. Krebs, “Multifunktionale Zelle: Vision, Realisierung, Leistungsdaten,” DLR, DLR, Tech. Rep., 2015, (2020, June 11). [Online]. Available: https://www.dlr.de/bt/Portaldata/35/Resources/dokumente/zlp-kolloquium_2015/Multifunktionale_Zelle-Vision,_Realisierung,_Leistungsdaten.pdf
- [107] AiBuild. AiCELL. (2020, June 11). [Online]. Available: <https://ai-build.com/>
- [108] S. Giannakopoulos and A. Markopoulou. Pylos. Institute for advanced architecture of Catalonia. (2020, June 11). [Online]. Available: <http://pylos.iaac.net/>
- [109] T. Shelton, “Cellular fabrication,” *Technology/Architecture + Design*, vol. 1, no. 2, pp. 251–253, 2017.
- [110] D. Chakraborty, B. A. Reddy, and A. R. Choudhury, “Extruder path generation for Curved Layer Fused Deposition Modeling,” *Computer-Aided Design*, vol. 40, no. 2, pp. 235–243, 2008.
- [111] X. Song, Y. Pan, and Y. Chen, “Development of a Low-Cost Parallel Kinematic Machine for Multidirectional Additive Manufacturing,” *Journal of Manufacturing Science and Engineering*, vol. 137, no. 2, 2015.
- [112] M. Invernizzi, G. Natale, M. Levi, S. Turri, and G. Griffini, “UV-Assisted 3D Printing of Glass and Carbon Fiber-Reinforced Dual-Cure Polymer Composites,” *Materials*, vol. 9, p. 583, 2016.
- [113] M. Rakhshbahar and M. Sinapius, “A Novel Approach: Combination of Automated Fiber Placement (AFP) and Additive Layer Manufacturing (ALM),” *Journal of Composites Science*, vol. 2, no. 3, p. 42, 2018.
- [114] C. Dai, C. C. Wang, C. Wu, S. Lefebvre, G. Fang, and Y.-J. Liu, “Support-Free Volume Printing by Multi-Axis Motion,” *ACM Transactions on Graphics*, vol. 37, no. 4, pp. 1–14, 2018.
- [115] Y. Huang, J. Zhang, X. Hu, G. Song, Z. Liu, L. Yu, and L. Liu, “Frame-Fab: Robotic Fabrication of Frame Shapes,” *ACM Transactions on Graphics*, vol. 35, no. 6, pp. 1–11, 2016.
- [116] M. De Gier, “Control of a robotic arm: Application to on-surface 3D-printing,” Master’s thesis, TU Delft, Delft Center for Systems and Control, 2015.
- [117] C. Wögerer, M. Mühlberger, M. Ikeda, J. Kastner, N. C. Chitturi, and A. Pichler, “Inkjet Printings on FFF printed curved surfaces,” in *Proceedings of the Fraunhofer Direct Digital Manufacturing Conference (DDMC)*, Berlin, Germany, 2018, pp. 108–114.
- [118] C. Hartl-Nesic, T. Glück, and A. Kugi, “Surface-based Path Following Control: Application of Curved Tapes on 3D Objects,” *IEEE Transactions on Robotics*, 2020, conditionally accepted.
- [119] D. Do, L. Ma, R. Paton, S. John, and I. Herszberg, “Automated consolidation

Bibliography

- during the manufacture of composite material based components,” in *Proceedings of International Conference on Composite Materials (ICCM)*, Paris, France, 1999.
- [120] L. Le-Tien, A. Albu-Schäffer, K. Janschek, and G. Hirzinger, “Entkopplungsregelung und Reibungskompensation für einen Roboter mit elastischen verkoppelten Gelenken,” *at – Automatisierungstechnik*, vol. 58, no. 9, pp. 499–511, 2010.
- [121] G. R. Kumar, P. Srinivasan, V. D. Holla, K. Shastri, and B. Prakash, “Geodesic curve computations on surfaces,” *Computer Aided Geometric Design*, vol. 20, no. 2, pp. 119–133, 2003.
- [122] G. Pamanes and S. Zeghloul, “Optimal placement of robotic manipulators using multiple kinematic criteria,” in *Proceedings of the IEEE International Conference on Robotics and Automation (ICRA)*, Sacramento, California, USA, 1991, pp. 933–938.
- [123] H. Fang, S. Ong, and A. Nee, “Robot path planning optimization for welding complex joints,” *The International Journal of Advanced Manufacturing Technology*, vol. 90, no. 9-12, pp. 3829–3839, 2017.
- [124] B. Kamrani, V. Berbyuk, D. Wäppling, U. Stickelmann, and X. Feng, “Optimal robot placement using response surface method,” *The International Journal of Advanced Manufacturing Technology*, vol. 44, no. 1-2, pp. 201–210, 2009.
- [125] J. T. Feddema, “Kinematically Optimal Robot Placement for Minimum Time Coordinated Motion,” in *Proceedings of the IEEE International Conference on Robotics and Automation (ICRA)*, Minneapolis, Minnesota, USA, 1996, pp. 3395–3400.
- [126] G.-C. Vosniakos and E. Matsas, “Improving feasibility of robotic milling through robot placement optimisation,” *Robotics and Computer-Integrated Manufacturing*, vol. 26, no. 5, pp. 517–525, 2010.
- [127] J. A. Nelder and R. Mead, “A simplex method for function minimization,” *The Computer Journal*, vol. 7, no. 4, pp. 308–313, 1965.
- [128] L. Piegl and W. Tiller, *The NURBS Book*, 2nd ed. Berlin Heidelberg: Springer, 1997.
- [129] M.-J. Kim, M.-S. Kim, and S. Y. Shin, “A General Construction Scheme for Unit Quaternion Curves with Simple High Order Derivatives,” in *Proceedings of the Special Interest Group on Graphics and Interactive Techniques (SIGGRAPH)*, Los Angeles, California, USA, 1995, pp. 369–376.
- [130] P. J. Olver and C. Shakiban, *Applied Linear Algebra*, 2nd ed., ser. Undergraduate Texts in Mathematics, S. Axler and K. Ribet, Eds. Cham: Springer, 2018.
- [131] A. J. Hanson, *Visualizing Quaternions*, ser. Interactive 3D Technology, D. Eberly, Ed. San Francisco: Morgan Kaufmann Publishers, 2006.
- [132] M. M. Flood, “The Traveling-Salesman Problem,” *Operations Research*, vol. 4, no. 1, pp. 61–75, 1956.

- [133] J. C. Mankins, "Technology Readiness Levels," Advanced Concepts Office, Office of Space Access and Technology, NASA, Tech. Rep., 1995.